JCTC Journal of Chemical Theory and Computation

pubs.acs.org/JCTC Article

Describing Polytopal Rearrangements of Fluxional Molecules with Curvilinear Coordinates Derived from Normal Vibrational Modes: A Conceptual Extension of Cremer−Pople Puckering Coordinates

Wenli Zou,[¶] Yunwen Tao,[¶] and Elfi Kraka*

Cite This: *J. Chem. Theory Comput.* 2020, 16, 3162−3193 Read Online

ACCESS | Metrics & More | Article Recommendations | Supporting Information

ABSTRACT: In this work a new curvilinear coordinate system is presented for the comprehensive description of polytopal rearrangements of *N*-coordinate compounds (*N* = 4−7) and systems containing an *N*-coordinate subunit. It is based on normal vibrational modes and a natural extension of the Cremer−Pople puckering coordinates (*J. Am. Chem. Soc.* **1975**, *97*, 1354) together with the Zou−Izotov−Cremer deformation coordinates (*J. Phys. Chem. A* **2011**, *115*, 8731) for ring structures to *N*-coordinate systems. We demonstrate that the new curvilinear coordinates are ideal reaction coordinates describing fluxional rearrangement pathways by revisiting the Berry pseudorotation and the lever mechanism in sulfur tetrafluoride, the Berry pseudorotation and two Muetterties' mechanisms in pentavalent compounds, the chimeric pseudorotation in iodine pentafluoride, Bailar and Ray-Dutt twists in hexacoordinate tris-chelates as well as the Bartell mechanism in iodine heptafluoride. The results of our study reveal that this dedicated curvilinear coordinate system can be applied to most coordination compounds opening new ways for the systematic modeling of fluxional processes.

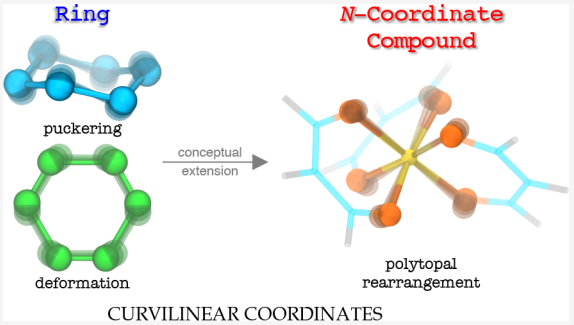

1. INTRODUCTION

Fluxional processes, in particular polytopal processes, have recently attracted attention caused by their potential to probe solvent−solute interactions[1−3] and to support self-healing processes.[4]

The term *polytopal rearrangement* describes a dynamic process that alters the positions of the vertices defined by the ligands in a coordination polyhedron; i.e., it "interconverts different or equivalent spatial arrangements of ligands about a central atom" as stated in the IUPAC Gold Book.[5−8] A well-known example for polytopal rearrangement found in most inorganic chemistry textbooks is the Berry pseudorotation of the PF_5 molecule.[9,10] Polytopal rearrangements being specific to coordination compounds are a subset of the broader class of *fluxionality*.[11−13] Many studies use "fluxionality",[14−16] "topomerization",[17] "stereomutation/enatiomerization",[13,17,18] "pseudorotation",[19−21] "permutational isomerization",[18,22] "polyhedral rearrangement/interconversion",[23,24] or "non-dissociative ligand exchange"[25] as a synonym for polytopal rearrangements.

Although a polytopal rearrrangement does not involve any ligand elimination and/or addition (i.e., no bond breaking and/or bond forming), it is of significant importance for chemists to understand the dynamics of such a process due to two reasons. (i) Fluxional flexibility can lead to more than one thermally accessible structure or to molecules with a dynamic structure, recently coined as molecules with a *quasistructure*.[26] (ii) Polytopal rearrangements affect the stereoselectivity and the reaction mechanism; therefore, they are critical for the reactivity and catalytic activity for many metal complexes.[27−34]

The tool extensively used by experimental chemists to determine molecular fluxionality is dynamic NMR spectroscopy.[13,35−38] On the basis of whether a polytopal rearrangement is either fast or slow compared to the NMR time scale,[39] its rate constant can be obtained by the Eyring equation.[12,40]

However, NMR spectroscopy is not able to provide us with information about the actual path that the atomic nuclei are tracing during a polytopal rearrangement. Therefore, we have to resort to quantum chemical calculations to model this path and verify the proposed mechanism(s) by calculating the activation energy.[41,42] On the one hand, often theory is guiding the experiment;[17,25] on the other hand, numerous mechanisms derived from experimental results await theoretical validation.[34]

One major obstacle in modeling polytopal rearrangements in coordination compounds is the lack of a generally applicable set of reaction coordinates tailored exclusively to distinctive *N*-coordinate geometries. Although some tricks (e.g., combining several bond angles[18] or dihedral angles[43]) could be employed

Received: December 20, 2019
Published: March 25, 2020

https://dx.doi.org/10.1021/acs.jctc.9b01274
J. Chem. Theory Comput. 2020, 16, 3162−3193

when driving the reaction complex into a desired reaction channel, these workarounds cannot achieve a systematic exploration of the configuration space of the N-coordinate motifs. However, it is of great necessity to determine all possible fluxional mechanisms for a specific geometry.

Noteworthy is the work related to polytopal rearrangement by Avnir, Alvarez, and co-workers who developed continuous symmetry measure (CSM) and continuous shape measure (CShM).[23,24,44−46] Their approach quantifies to what extent the geometry of a coordination compound matches the geometry of a reference compound with high symmetry or that of a regular polyhedron. By defining the "minimal distortion paths" for several polytopal rearrangement mechanisms, one can position a given coordination geometry onto the predefined minimal distortion paths.[23] After enumerating all relevant X-ray crystal structures with this approach, they observed a concentrated distribution of the geometries along the minimal distortion path, which they visualized as a "shape map". These results convincingly proved the existence of a polytopal rearrangement mechanism with numerous discrete structures. CSM and CShM measures offer a simplified way to describe and categorize the geometries of coordination compounds. However, one caveat is appropriate; the structural descriptors based on CSM/CShM will generally not span the complete configuration space of the N-coordinate motif and as such cannot serve as reaction coordinates used for practical calculations modeling polytopal rearrangement pathways.

Therefore, in this work, we adopted the conceptual approach of Cremer−Pople ring puckering coordinates[47] aiming at the development of a curvilinear coordinate system that provides appropriate reaction coordinates to (i) facilitate modeling polytopal rearrangements in N-coordinate molecules and (ii) present a simplified but comprehensive description of the conformational changes taking place during these rearrangements.

The paper is structured in the following way: First, the ring puckering and deformation coordinates are briefly reviewed in terms of their underlying rationale as the basis to define the N-coordinate reference system AB_n, its symmetry, configurational space, and molecular vibrations. Then, the curvilinear coordinate parameters for any N-coordinate geometry (N = 4−7) are derived from normal vibrational modes of the corresponding reference system. After the Computational Details section, nine different polytopal rearrangement mechanisms ranging from tetracoordinated to heptacoordinated compounds are revisited using the curvilinear coordinates derived in this work to demonstrate the general applicability of our new approach. The conclusions, along with perspectives on future work, are given in the last section.

2. METHODOLOGY

2.1. Retrospective on Cremer−Pople Ring Puckering and Deformation Coordinates. The Cremer−Pople ring puckering coordinates proposed in 1975 have become a well-accepted standard tool to describe the out-of-plane conformational flexibility of ring structures in cyclic molecules.[47−53] It is based on the concept of partitioning the $(3N-6)$-dimensional configuration space of an N-membered ring structure ("N-ring") into two subspaces where ring puckering and deformation motions take place, respectively.

Any N-ring has an $(N-3)$-dimensional puckering space spanned by $N-3$ basis conformations whose linear combinations are specified by ring puckering coordinates. The z-component of the Cartesian coordinates for each ring atom z_j (j = 1, 2, ..., N) depicting the puckering conformation relative to an ideal planar form (mean ring plane) is connected to the puckering amplitude q_m and pseudorotation phase angle ϕ_m via the following formulas depending on the parity of N:[47,48]

$$z_j = \sqrt{\frac{2}{N}} \sum_{m=2}^{(N-1)/2} q_m \cos\left[\phi_m + \frac{2\pi m(j-1)}{N}\right] \qquad (N \text{ odd}) \tag{1}$$

$$z_j = \sqrt{\frac{2}{N}} \sum_{m=2}^{(N-2)/2} q_m \cos\left[\phi_m + \frac{2\pi m(j-1)}{N}\right] + \sqrt{\frac{1}{N}} q_{N/2}(-1)^{j-1} \qquad (N \text{ even}) \tag{2}$$

where a pseudorotation cycle only starts from the five-membered ring ($N-3=2$) and the puckering coordinate pair (q_2, ϕ_2) is used to describe the motion in the puckering subspace. Puckering starts from the four-membered ring ($N-3=1$) with the puckering amplitude q_2.

The in-plane deformations of the N-ring take place in a $(2N-3)$-dimensional subspace complementing the $(N-3)$ out-of-plane motions to $(3N-6)$ coordinates. In recent work, we derived the ring deformation coordinates (RDC) as the complement to Cremer−Pople puckering coordinates rendering a whole picture of the ring configuration with curvilinear coordinates.[54−56] The definition of RDCs relies on further partitioning of the $(2N-3)$-dimensional deformation space into (1) a one-dimensional ring breathing mode subspace, determined by the breathing radius R and (2) $N-2$ two-dimensional pseudorotational subspaces spanned by pairs of amplitudes t_n and phase angles τ_n (n = 1, 2, ..., $N-2$). After the N-ring is positioned into *standard orientation*, the Cartesian coordinates of the ring atoms are linked to the deformation coordinate parameters R and (t_n, τ_n) with the following formulas:[54]

$$x_j = -R\cos\left[\frac{2\pi(j-1)}{N}\right] + \sum_{n=1}^{N-2} t_n \cos\left[\tau_n - \frac{2\pi(n+1)(j-1)}{N}\right] \tag{3}$$

$$y_j = R\sin\left[\frac{2\pi(j-1)}{N}\right] + \sum_{n=1}^{N-2} t_n \sin\left[\tau_n - \frac{2\pi(n+1)(j-1)}{N}\right] \tag{4}$$

where all z_j components as the out-of-plane deviations are related to puckering coordinates in eqs 1 and 2.

With the Cremer−Pople ring puckering coordinates and the recently developed ring deformation coordinates, one obtains a comprehensive, quantitative, and intuitive description of ring conformations of any N-membered ring.[47,54] Furthermore, the potential-energy surface (PES) or free-energy surface (FES) in $3N-6$ dimensions of the N-ring system can be reduced to two- or three-dimensional contour plots with deeper physical insight and higher interpretability.[53−67]

The success of these two curvilinear coordinate systems in describing ring conformations can be attributed to their generally applicable mathematical form for all N-rings; more

https://dx.doi.org/10.1021/acs.jctc.9b01274
J. Chem. Theory Comput. 2020, 16, 3162−3193

importantly, they turn out to be the natural choice in characterizing ring conformations and their changes because both the Cremer−Pople puckering coordinates and the ring deformation coordinates were inspired and derived from the normal vibrational modes.[51,54] Either the out-of-plane puckering or in-plane deformation/rearrangement of the N-ring is initialized by a molecular vibration or the mixing of several degenerate vibrations[68−70] acting as the leading parameter.[71−73] By adopting this conceptual approach, we aimed in this work at developing new curvilinear coordinates for more distinctive geometries besides ring structures. The novel curvilinear coordinates derived from molecular vibrations are expected to be especially useful in describing conformational changes and structural rearrangements involving multiple atoms simultaneously.

One may question the extension of the underlying rationale in ring coordinates (i.e., a specific vibration in a ring initiates puckering or deformation motion) to other molecular geometries in general. However, it has been widely recognized that molecular vibrations can drive chemical reactions by exciting a specific vibrational mode of the reactant along the reaction coordinate and in this way overcoming the energy barrier toward the product.[74,75] Crim, Zare, and others have demonstrated the possibilities of experimentally controlling the course of chemical reactions in gas phase and on metal surfaces by selectively exciting certain vibrational modes with a laser.[76−91] Therefore, the conceptual extension of ring coordinates to other geometries based on molecular vibrations has its physical foundation.

2.2. Vibration-Based Curvilinear Coordinates for *N*-Coordinate Geometry. Unlike for ring puckering/deformation coordinates, there is no direct analytic mathematical solution to connect each atom's Cartesian coordinates to the curvilinear coordinates describing N-coordinate systems due to the following reasons.

- The z-space can be separated from the x,y-space when defining the puckering[47] and deformation[54] coordinates for rings, respectively. However, the conformational changes in N-coordinate geometries involve atomic movement in the three-dimensional (3D) space which is more complex.
- The mathematical expression of either Cremer−Pople puckering or ring deformation coordinates has already encompassed the normal vibrational modes of the corresponding reference model systems (i.e., planar ring and regular polygon) implicitly. However, in the case of an N-coordinate geometry, we need to explicitly define the normal vibrational modes as the basis vectors spanning the configurational space of an N-coordinate geometry beforehand.

In the following, we elaborate how the curvilinear coordinates derived from normal vibrational modes for N-coordinate geometries are defined. Depending on the value of N, the geometry can be tricoordinate, tetracoordinate, pentacoordinate, hexacoordinate, heptacoordinate (e.g., IF_7), or octacoordinate (e.g., XeF_8^{2-}).[92] Within the same type of N-coordinate geometry, the relative spatial arrangement of the ligating atoms bonded to the central atom may vary. This complication can be resolved by utilizing point group information for the differentiation. For example, both $Fe(CO)_5$ and ClF_5 have a pentacoordinate geometry; however, the former is trigonal bipyramidal and the latter is square pyramidal, or expressed in the point group language, the former has D_{3h} and the latter has C_{4v} symmetry.

As shown in Figure 1, we define in this work the curvilinear coordinates with respect to a tetracoordinate geometry with T_d symmetry, pentacoordinate geometries with D_{3h} and C_{4v} symmetry, hexacoordinate geometries with O_h and C_{5v} symmetry along with heptacoordinate geometries with D_{5h} and C_{6v} symmetry to cover the vast majority of coordination compounds with fluxionality.

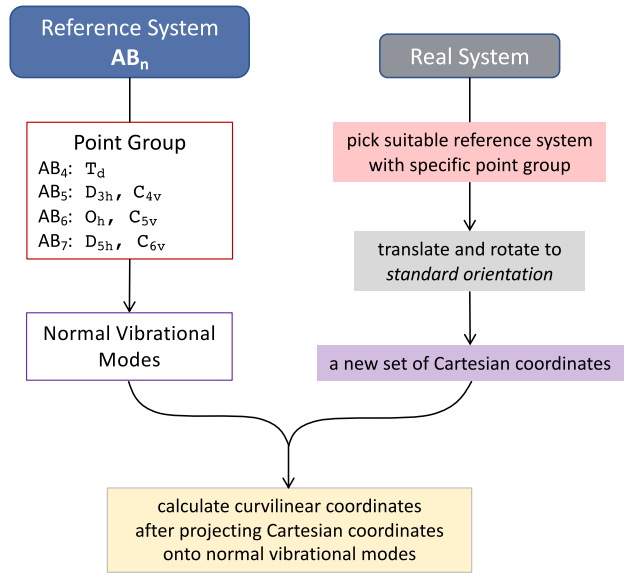

Figure 1. Schematic diagram illustrating the definition of curvilinear coordinates derived from normal vibrational modes for N-coordinate geometries.

The pentacoordinate geometry in C_{4v} symmetry is taken as an example in the following to stepwise illustrate how the curvilinear coordinate system derived from normal modes for an N-coordinate geometry is defined. The same procedure equally applies to other geometries with various point groups mentioned above.

2.2.1. Reference System for a Given Symmetry. As in the case of defining ring puckering coordinates with regard to the mean plane,[68−70] we first need to stipulate a reference system AB_n for the given symmetry, e.g., C_{4v}, where A is the central atom and n atoms of B are bonded to A as the first coordination sphere.

The definition of the reference system in Cartesian coordinates has to fulfill the following requirements:

- The central atom A denoted as the first atom is placed at the origin of the 3D Cartesian coordinate system.
- All A−B distances are set to be the same and assigned a value of r_1. This is equivalent to the situation that all atoms B are positioned on the surface of a sphere with radius r_1 and the center of sphere is placed at atom A.
- The relative positions of atoms B are adjusted under a symmetry constraint to guarantee that the geometrical center of AB_n is located at the position of atom A.

In addition, the following two conditions are optional.

- The z-axis is chosen to be the highest n-fold rotation axis of AB_n.
- Atoms B are grouped according to their z-values from top to bottom. If the first group of B has more than one atom,

https://dx.doi.org/10.1021/acs.jctc.9b01274
J. Chem. Theory Comput. 2020, 16, 3162−3193

the first atom within this group is placed right above the $+x$-axis ($y = 0$) and the remaining atoms are numbered counterclockwise when looking into the direction from atom 2 to atom 1. If the first group of B has only one atom, then this atom is positioned on the z-axis. Meanwhile, the first atom of the second group is positioned in the $+x$ direction ($y = 0$).

For example, the reference system AB_5 with the C_{4v} point group (shown in Figure 2) has 18 Cartesian coordinates

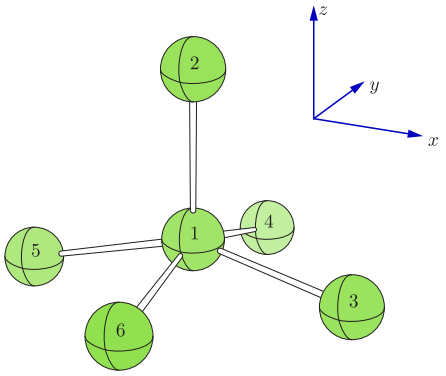

Figure 2. Ball-and-stick representation for the reference system AB_5 with C_{4v} symmetry in Cartesian coordinates. The schematic Cartesian axes are shown for illustrating directions while the true origin is at the first atom A.

collected in matrix $\mathbf{R}_0$ with dimension 6×3 shown in eq 5. The three columns correspond to x, y, and z components and the six rows correspond to the six atoms of the reference system ordered according to the above description. The first row specifies the position of A at the origin point.

$$\mathbf{R}_0 = \begin{bmatrix} 0 & 0 & 0 \\ 0 & 0 & r_1 \\ \mathcal{G}r_1 & 0 & -Cr_1 \\ 0 & \mathcal{G}r_1 & -Cr_1 \\ -\mathcal{G}r_1 & 0 & -Cr_1 \\ 0 & -\mathcal{G}r_1 & -Cr_1 \end{bmatrix} \quad (5)$$

where $\mathcal{G} = \sqrt{15}/4, C = 1/4$, and r_1 is the radius depending on the real system, which will be clarified below.

A reference system for a given symmetry operates like a template with fixed shape, which can be scaled by r_1. Furthermore, it serves as the basis for deriving the normal vibrational modes, which are independent of r_1.

2.2.2. Normal Vibrational Modes of Reference System. In order to span the complete configuration space of the reference system AB_n with a given symmetry, we need to derive one set of normal vibrational mode vectors acting as the basis. We employ for this purpose the following two-step procedure.

First, a model Hamiltonian accounting only for the pairwise nuclear charge repulsion is used to describe the interatomic forces within the reference system geometry (with r_1 temporarily taking an arbitrary value between 1 and 2 Å) leading to a model Hessian matrix which is calculated analytically. With the assumption that all atoms in AB_n have identical unit atomic masses (1 amu), the normal-mode analysis is carried out leading to an initial set of $3M - 6$ normal vibrational modes where $M = n + 1$. Besides, three rotational normal modes calculated with massless Eckart conditions[93,94] are obtained as column vectors $\mathbf{r}_1$, $\mathbf{r}_2$, and $\mathbf{r}_3$. (Please note that $\mathbf{r}_1$, $\mathbf{r}_2$, and $\mathbf{r}_3$ must not be confused with r_1, r_2, and r_3 representing amplitudes.)

Second, this initial set of $3M - 6$ normal modes is fine-tuned within the internal vibrational space by pairwise rotation according to the following rules:

(1) Two nondegenerate normal vibrations with the same irreducible representation can be mixed via a 2×2 rotation matrix leading to another two normal vibrations with the same symmetry.
(2) The first vibrational mode should always be the totally symmetric breathing mode of the present point group. The amplitude for all n atoms B in this vibrational mode vector must be identical, while the central atom A has no contribution.
(3) The atom A can be distorted only in the last three normal modes, which correspond to the relative translation between atom A and the remaining n atoms B in x, y, and z directions.
(4) Doubly degenerate modes (denoted as E and $E^{\dagger}$) or triply degenerate modes (T, $T^{\dagger}$, and $T^{\ddagger}$), can be pairwise rotated among themselves to fulfill the following requirements that
   (a) for the E or T mode, the distortions in the z direction and/or y direction are zero if possible,
   (b) for the $T^{\dagger}$ mode, the distortions in the y direction and/or x direction are zero if possible, and
   (c) the $E^{\dagger}$ or $T^{\ddagger}$ mode can be obtained by orthonormal condition.

Pairwise rotation as described between any two normal vibrational modes is a unitary transformation that keeps the orthonormality of $3M - 6$ normal modes and greatly simplifies the basis vibration vectors for later use.

Figure 3 shows all 12 normal vibrational modes of the AB_5 reference system in the C_{4v} point group. The normal mode vectors $\{\mathbf{l}_i\}$ ($i = 1, 2, ..., 3M - 6$) shown as $(M \times 3)$-dimensional matrices are orthonormal to each other. The collection of normal vibrational modes we derived for the other reference systems can be found in Appendices A.2–A.5.

2.2.3. Real System in Standard Orientation. For a real molecular compound with N-coordinate geometry as its core, the central N-coordinate part ("real system") deviates more or less from the reference geometry with a given symmetry during conformational changes or reaction processes. It would be ideal to express such distortions in terms of the normal vibrational modes that we derived for selected reference systems. In order to do so, we have to order the atomic labels of the real system according to those of the reference system for consistency and then place the real system into a particular position, where its internal coordinate space matches exactly the internal vibrational space of the reference system without any contamination from the translational or rotational space of the reference system.[95,96] This requires the following *standard orientation* to be imposed on the real system geometry:

- The initial Cartesian coordinates of the real system with N-coordinate geometry are recorded as $\mathbf{X}$, which is an $M \times 3$ matrix.
- The real system needs to be translated so that its geometrical center is positioned at the origin of Cartesian coordinate system, current Cartesian coordinates of the real system are collected in $\mathbf{X}_c$.

https://dx.doi.org/10.1021/acs.jctc.9b01274
J. Chem. Theory Comput. 2020, 16, 3162–3193

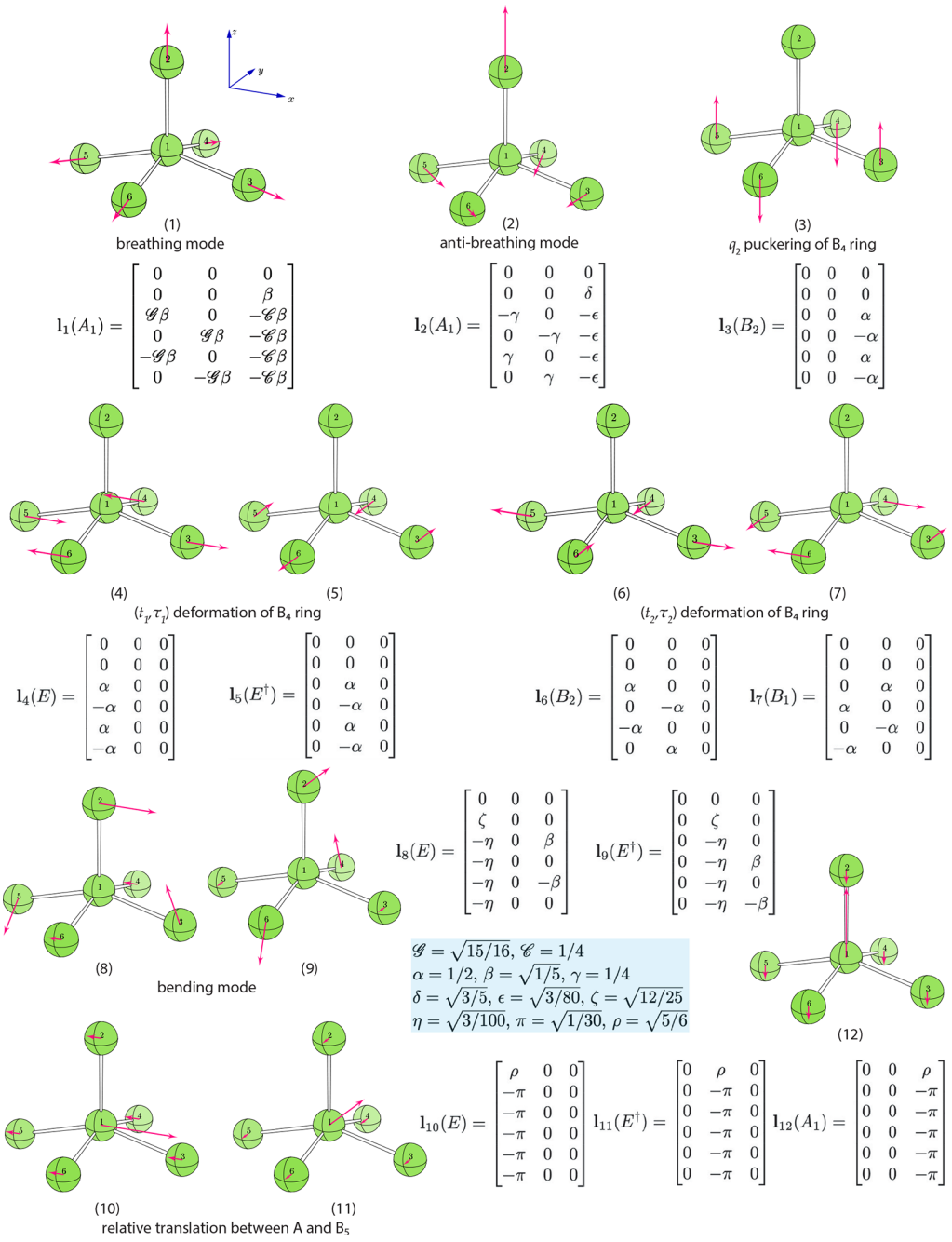

Figure 3. Twelve normal vibrational modes for the AB_5 reference system with C_{4v} symmetry. Below the ball-and-stick representations are the labels and brief descriptions of the normal modes. The irreducible representation and the mode vector for each vibration are also shown.

- The real system is then rotated in the 3D space so that its Cartesian coordinates denoted $\mathbf{X}_r$ are orthogonal to the rotational modes $\{\mathbf{r}_1, \mathbf{r}_2, \mathbf{r}_3\}$ of the reference system. This final set of Cartesian coordinates $\mathbf{X}_r$ is named *standard orientation* for the real system.

The rotation of the real system by a rotation matrix $\mathbf{u}$ can be expressed by the product of three 3 × 3 elemental rotation matrices

$$\mathbf{u} = \mathbf{u}_z\mathbf{u}_y\mathbf{u}_x \tag{6}$$

where $\mathbf{u}_x$, $\mathbf{u}_y$, and $\mathbf{u}_z$ define the rotation around x-, y-, and z-axes, respectively.

$$\mathbf{u}_x = \begin{bmatrix} 1 & 0 & 0 \\ 0 & \cos\theta_x & -\sin\theta_x \\ 0 & \sin\theta_x & \cos\theta_x \end{bmatrix} \quad \mathbf{u}_y = \begin{bmatrix} \cos\theta_y & 0 & \sin\theta_y \\ 0 & 1 & 0 \\ -\sin\theta_y & 0 & \cos\theta_y \end{bmatrix}$$
$$\mathbf{u}_z = \begin{bmatrix} \cos\theta_z & -\sin\theta_z & 0 \\ \sin\theta_z & \cos\theta_z & 0 \\ 0 & 0 & 1 \end{bmatrix} \tag{7}$$

This leads to

$$\mathbf{X}_r = \mathbf{X}_c\mathbf{u} \tag{8}$$

https://dx.doi.org/10.1021/acs.jctc.9b01274
J. Chem. Theory Comput. 2020, 16, 3162−3193

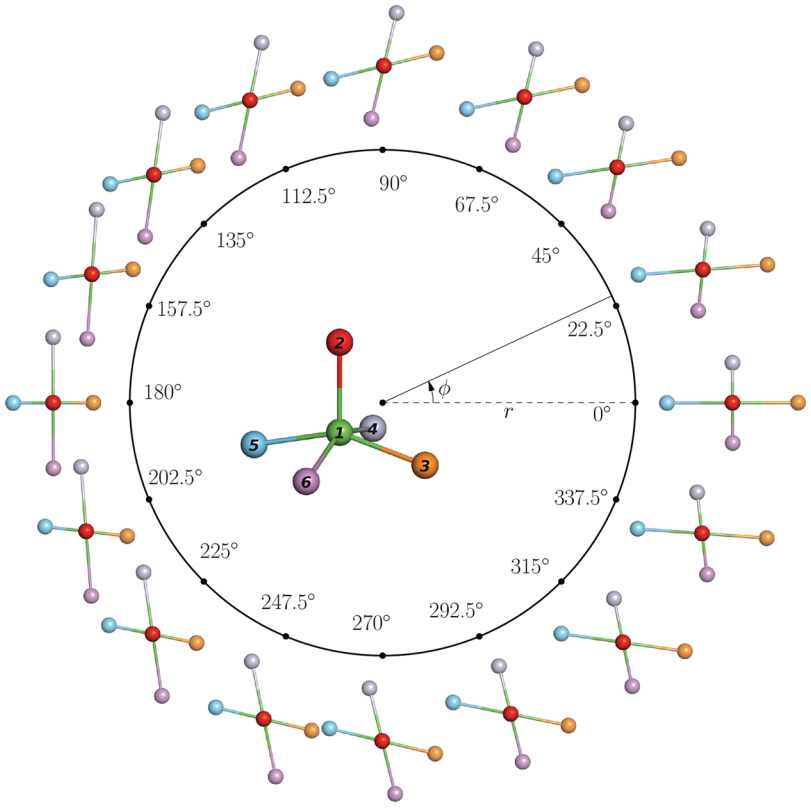

Figure 4. $\{r_S, \phi_S\}$ pseudorotational cycle specifying the (t_2, τ_2) deformation of the B_4 ring within the reference system AB_5 in C_{4v} symmetry (see Table 1). In the center of the cycle is the reference geometry for AB_5 with $r_1 = 1.5$ Å, and surrounding the cycle are the representative geometries for $r_S = 0.35$ Å and different ϕ_S values starting from 0° with the interval of 22.5° while all other r_m values (except r_1) are 0. The representative geometries are shown in the perspective of looking downward from atom 2 (red) to atom 1 (green), highlighting the in-plane deformation of the B_4 ring consisting of atoms 3−6.

We rearrange the Cartesian coordinates $\mathbf{X}_c$ and $\mathbf{X}_r$ from matrix form into the $(1 \times 3M)$-dimensional row vector form as $\vec{\mathbf{X}}_c$ and $\vec{\mathbf{X}}_r$; then a $(3M \times 3M)$-dimensional block diagonal matrix $\mathbf{U}$ is constructed with rotation matrix $\mathbf{u}$ as diagonal blocks and $\mathbf{0}_{3\times3}$ for nondiagonal blocks.

By definition, the standard orientation requires that

$$\begin{cases} \vec{\mathbf{X}}_r\mathbf{r}_1 = \vec{\mathbf{X}}_c\mathbf{U}\mathbf{r}_1 = 0 \\ \vec{\mathbf{X}}_r\mathbf{r}_2 = \vec{\mathbf{X}}_c\mathbf{U}\mathbf{r}_2 = 0 \\ \vec{\mathbf{X}}_r\mathbf{r}_3 = \vec{\mathbf{X}}_c\mathbf{U}\mathbf{r}_3 = 0 \end{cases} \tag{9}$$

where $\vec{\mathbf{X}}_c$, $\mathbf{r}_1$, $\mathbf{r}_2$, and $\mathbf{r}_3$ are already known so that only three rotation angles θ_x, θ_y, and θ_z remain as the unknowns contained in $\mathbf{U}$, which can be determined by iteratively solving this system of nonlinear equations.

However, practically solving the above system of equations with numerical methods could lead to an undesired solution as multiple sets of solutions could exist. This issue arises when the starting geometry in Cartesian coordinates $\mathbf{X}_c$ is close to another undesired standard orientation. As a remedy, the arbitrariness of rotation matrix $\mathbf{u}$ may be eliminated by minimizing the root mean-square deviation (RMSD) between the Cartesian coordinates $\mathbf{X}_c$ and the reference system, which has been proven by Kudin and Dymarsky[97] to be closely related to the well-known Eckart axis conditions. In this work, we adopt the quaternion-based algorithm of Kearsley[98] to first rotate the real system. Noteworthy is that before calculating the best-fit alignment between real system and reference system, the A−B distance r_1 in the reference system is temporarily set to be the averaged A−B distance of the real system. With the real system rotated, its Cartesian coordinates change from $\mathbf{X}_c$ to $\mathbf{X}_f$ and the standard orientation can be unambiguously obtained by solving the system of equations in eq 10

$$\begin{cases} \vec{\mathbf{X}}_r\mathbf{r}_1 = \vec{\mathbf{X}}_f\mathbf{U}\mathbf{r}_1 = 0 \\ \vec{\mathbf{X}}_r\mathbf{r}_2 = \vec{\mathbf{X}}_f\mathbf{U}\mathbf{r}_2 = 0 \\ \vec{\mathbf{X}}_r\mathbf{r}_3 = \vec{\mathbf{X}}_f\mathbf{U}\mathbf{r}_3 = 0 \end{cases} \tag{10}$$

where $\vec{\mathbf{X}}_r$ is guaranteed to be the desired standard orientation calculated by numerical equation solver because $\mathbf{X}_f$ is close to $\mathbf{X}_r$ and $\theta_x = \theta_y = \theta_z = 0$ can be used as the initial guess. Usually, the calculation of eq 10 converges after one iteration.

2.2.4. Calculation of Curvilinear Coordinates. Once the real system is positioned in the appropriate standard orientation, its geometry $\mathbf{X}_r$ can be completely described by the set of $3M - 6$ normal vibrational modes of the corresponding reference system AB_n.

The determination of the real system geometry along the directions of normal vibrations is calculated by the projection of Cartesian coordinates $\mathbf{X}_r$ onto each normal mode vector $\mathbf{l}_i$ $(i = 1, 2, ..., 3M - 6)$ using the dot product d_i

$$d_i = \vec{\mathbf{X}}_r\vec{\mathbf{l}}_i^{\mathrm{T}} \tag{11}$$

https://dx.doi.org/10.1021/acs.jctc.9b01274
J. Chem. Theory Comput. 2020, 16, 3162−3193

where $\vec{\mathbf{X}}_r$ and $\vec{\mathbf{l}}_i$ take the row vector form of matrices $\mathbf{X}_r$ and $\mathbf{l}_i$, respectively, and superscript T indicates the transpose.

Up to this point, we are able to describe the geometry of the real system merely by the set of $3M - 6$ projection values $\{d_i\}$ as long as corresponding normal vibrational modes for the reference system have been determined beforehand. Besides, for those doubly or triply degenerate vibrations we derived for the reference systems, it would be more useful if these degenerate vibrations are combined using pseudorotational cycles in polar coordinates or using the conformational globe in cylindrical/spherical coordinates as for ring puckering coordinates. Even for nondegenerate vibrational modes, they can also be grouped together for convenience.

Along these lines, we define three types of curvilinear coordinate sets for an N-coordinate geometry:

(i) nondegenerate curvilinear coordinate $\{r_m\}$

$$r_m = \mathcal{F} d_m \tag{12}$$

where $\mathcal{F}$ is the largest atomic amplitude within the normal mode vector $\mathbf{l}_m$ associated with the projection value d_m. For example, within the first breathing mode of the reference system AB_5 in C_{4v} symmetry, all four atoms B have the largest amplitude as $\sqrt{\alpha^2 + \beta^2} = 1/2$. Therefore, $\mathcal{F}$ takes the value of 1/2 for this particular vibrational mode.

With $\mathcal{F}$ as a scaling factor, r_m has the same fundamental unit of distance as d_m, generally expressed in Angstrom units. r_m can be either positive or negative.

(ii) doubly degenerate curvilinear coordinates $\{r_m, \phi_m\}$

$$\begin{cases} r_m \cos \phi_m = \mathcal{F} d_m \\ r_m \sin \phi_m = \mathcal{F} d'_m \end{cases} \tag{13}$$

where d_m and d'_m are the projections from real system geometry $\mathbf{X}_r$ onto a pair of doubly degenerate (E and $E^\dagger$) vibrational modes and the curvilinear coordinates $\{r_m, \phi_m\}$ are calculated by solving above system of equations.

This curvilinear coordinate parameter set specifies a polar coordinate system where we expect that

$$r_m \geqslant 0,\ 0^\circ \leqslant \phi_m < 360^\circ \tag{14}$$

During a relaxed PES scan or reaction pathway, r_m is allowed to take a negative value with the following equivalence relation.

$$\{r_m, \phi_m\} \equiv \{-r_m, \phi_m \pm 180^\circ\} \tag{15}$$

For a fixed amplitude r_m, a pseudorotational cycle arises when the phase angle ϕ_m gradually changes, as shown in Figure 4. When ϕ_m equals 0°/180°, the second degenerate vibration has no contribution, and when ϕ_m equals 90°/270°, the contribution from the first degenerate vibration vanishes. Otherwise, both vibrations contribute to determine the geometry of the real system.

iii. triply degenerate curvilinear coordinates $\{r_m, \theta_m, \phi_m\}$

$$\begin{cases} r_m \cos \theta_m = \mathcal{F} d_m \\ r_m \sin \theta_m \sin \phi_m = \mathcal{F} d'_m \\ r_m \sin \theta_m \cos \phi_m = \mathcal{F} d''_m \end{cases} \tag{16}$$

where d_m, d'_m, and d''_m are the projections from $\mathbf{X}_r$ onto a triad of triply degenerate (T, $T^\dagger$, and $T^\ddagger$) vibrational modes and $\{r_m, \theta_m, \phi_m\}$ determines a spherical coordinate system where we expect that

$$r_m \geqslant 0,\ 0^\circ \leqslant \theta_m \leqslant 180^\circ,\ 0^\circ \leqslant \phi_m < 360^\circ \tag{17}$$

Also, r_m can take a negative value with the following equivalence relation.

$$\begin{aligned} \{r_m, \theta_m, \phi_m\} &\equiv \{-r_m, 180^\circ - \theta_m, \phi_m \pm 180^\circ\} \\ &\equiv \{r_m, -\theta_m, \phi_m \pm 180^\circ\} \end{aligned} \tag{18}$$

This set of curvilinear coordinate parameters controls the contribution from three vibrations to the real system geometry in a similar fashion as the doubly degenerate set. For a given value of r_m, we adopt the idea of conformational globe from ring puckering coordinates for describing the conformational variation in N-coordinate geometries as shown in Figure 6.

Consequently, the geometry of the real system in the standard orientation with regard to the selected reference system AB_n having M atoms can be accurately determined by $3M - 6$ curvilinear coordinate parameters of the above three types.

Table 1 summarizes seven sets of curvilinear coordinate parameters we constructed for the AB_5 system with C_{4v} symmetry. The geometry of the reference system is determined once r_1 has been calculated with eq 12.

Table 1. Summary of 12 Curvilinear Coordinate Parameters in 7 Sets Based on 12 Normal Vibrational Modes for the Reference System AB_5 in C_{4v} Symmetry

normal mode	curvilinear coordinates	symmetry	description
1	r_1	A_1	AB_5 breathing
2	r_2	A_1	antibreathing
3	r_3	B_2	q_2 puckering of B_4 ring
4, 5	r_4, ϕ_4	E	(t_1, τ_1) deformation of B_4 ring
6, 7	r_5, ϕ_5	$B_2 + B_1$	(t_2, τ_2) deformation of B_4 ring
8, 9	r_6, ϕ_6	E	bending
10, 11, 12	r_7, θ_7, ϕ_7	$E + A_1$	translation of A

Note that we have combined the sixth and seventh normal modes into a pair of doubly degenerate curvilinear coordinates $\{r_5, \phi_5\}$ although these two modes have different symmetries. This is because these two vibrational modes are the basis vectors for the (t_2, τ_2) deformation of the B_4 ring[54] and they are similar in their mathematical form with identical $\mathcal{F}$ values.

Figure 4 shows a $\{r_5, \phi_5\}$ pseudorotational cycle where a single curvilinear coordinate parameter ϕ_5 determines the geometrical variation in AB_5. Figure 5 illustrates a two-dimensional (2D) PES by relaxed scanning r_5 and ϕ_5 simultaneously for the PF_5 molecule as a showcase example to demonstrate one possibility of applying the curvilinear coordinates developed in this work to model polytopal rearrangements. Besides, we have combined the pair of degenerate vibrations (10th and 11th) with the 12th vibrational mode into a triply degenerate set of curvilinear coordinates $\{r_7, \theta_7, \phi_7\}$ because these three vibrational modes are similar in their mathematical form and all of them describe the relative translations of the central atom.

2.2.5. Conversion from Curvilinear Coordinates into Cartesian Coordinates. During a quantum chemical modeling of an N-coordinate compound with its geometry described with the curvilinear coordinates, the back-conversion from curvilinear coordinates to Cartesian coordinates is needed.

https://dx.doi.org/10.1021/acs.jctc.9b01274
J. Chem. Theory Comput. 2020, 16, 3162−3193

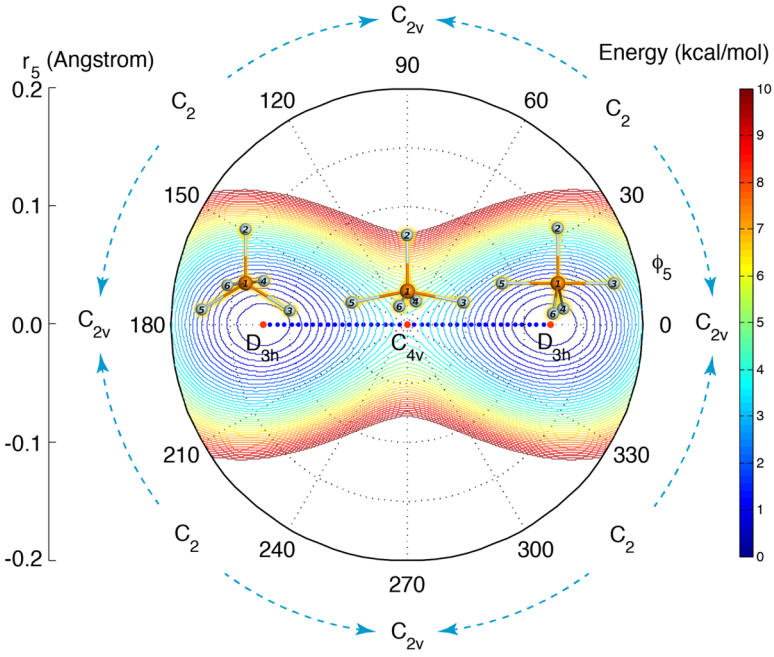

Figure 5. 2D PES of PF_5 obtained by relaxed scan of $\{r_5, \phi_5\}$ based on the AB_5 reference system in C_{4v} symmetry. An energy scale is given on the right side and data points with energy values over 10 kcal/mol have been removed from the contour plot. A minimum-energy path characterizing the Berry pseudorotation[9,10] is indicated by the blue dots, where two lowest energy structures in D_{3h} symmetry and the first-order saddle point structure in C_{4v} symmetry are marked with red dots. Geometries with $\phi_5 = 0°/90°/180°/270°$ have C_{2v} or higher symmetries, while the rest of the geometries have C_2 symmetry. Calculations were carried out at the B3LYP/cc-pVTZ level. A 3D representation of this PES is included in the Supporting Information.

For this purpose, we first calculate the projection values d_i from curvilinear coordinates according to eqs 12, 13, and 16. Then, the Cartesian coordinates $\mathbf{X}_r$ in standard orientation are calculated via

$$\mathbf{X}_r = \sum_{i=1}^{3M-6} d_i \mathbf{l}_i \tag{19}$$

which utilizes the orthonormality of the normal modes.

2.2.6. Wilson B-Matrix and Geometry Optimization. Using the curvilinear coordinates defined above, to optimize equilibrium geometries and transition states with quasi-Newton algorithms[99,100] in quantum chemical packages requires the Wilson **B**-matrix and its derivative d**B**-matrix defined in eqs 20 and 21, respectively.

$$B_{n,i} = \frac{\partial q_n}{\partial x_i} \tag{20}$$

$$\mathrm{d}B_{n,i,j} = \frac{\partial^2 q_n}{\partial x_i \partial x_j} \tag{21}$$

where q_n is an internal coordinate or curvilinear coordinate parameter while x_i and x_j are Cartesian coordinate components of $\mathbf{X}_r$ in standard orientation.

We did not derive yet an analytic Wilson **B**-matrix and its derivatives. Therefore, for the time being these matrices are calculated numerically according to the formula listed in Appendix A.1.

2.2.7. Extension to Larger Molecules with N-Coordinate Core. For those coordination compounds having more than one coordination sphere (e.g., $Fe(CO)_5$), the curvilinear coordinates developed in this work only determine the geometry of the *N*-coordinate core fragment. We employed the **Z**-matrix formulation by combining the curvilinear coordinates describing the core fragment and the internal coordinates (e.g., bond length, bond angle, and dihedral angle) describing the outer spheres, so that our curvilinear coordinate system is seamlessly incorporated into the internal coordinate system implemented in most quantum chemical packages. In this way, conventional geometry optimization machinery can be employed with the newly developed curvilinear coordinates for larger coordination compounds.

3. COMPUTATIONAL DETAILS

In this work, we have developed a utility program CURVI that converts Cartesian coordinates into curvilinear coordinates and vice versa. Programs written to carry out geometry optimization in terms of curvilinear coordinates have been incorporated into the *ab initio* program COLOGNE19.[101]

All quantum chemical calculations including single-point energy, geometry optimization, relaxed PES scan, harmonic vibrational frequencies and intrinsic reaction coordinate (IRC) path were performed with the *ab initio* program packages COLOGNE19[101] and Gaussian 16.[102] Density functional theory (DFT) with an UltraFine integration grid was employed to model all systems in this work. The PF_5 molecule in Figure 5 was calculated at the B3LYP/cc-pVTZ level,[103−107] the $Fe(CO)_5$ and $Ga^{III}(mda)_3$ compounds were calculated using the Minnesota hybrid functional M06L[108] with Ahlrichs' Def2SVP basis set,[109,110] and all molecules without metal atoms were calculated at M06-2X/Def2SVP level.[111]

Relaxed PES scans were conducted by combining the curvilinear coordinates describing the core fragment with internal coordinates describing the outer-layer atoms within the Z-matrix formulation. Each scan step was considered as optimized when the maximum force is below 0.0025 au and the maximum geometrical deviation is below 0.01 au. The geometry

https://dx.doi.org/10.1021/acs.jctc.9b01274
J. Chem. Theory Comput. 2020, 16, 3162−3193

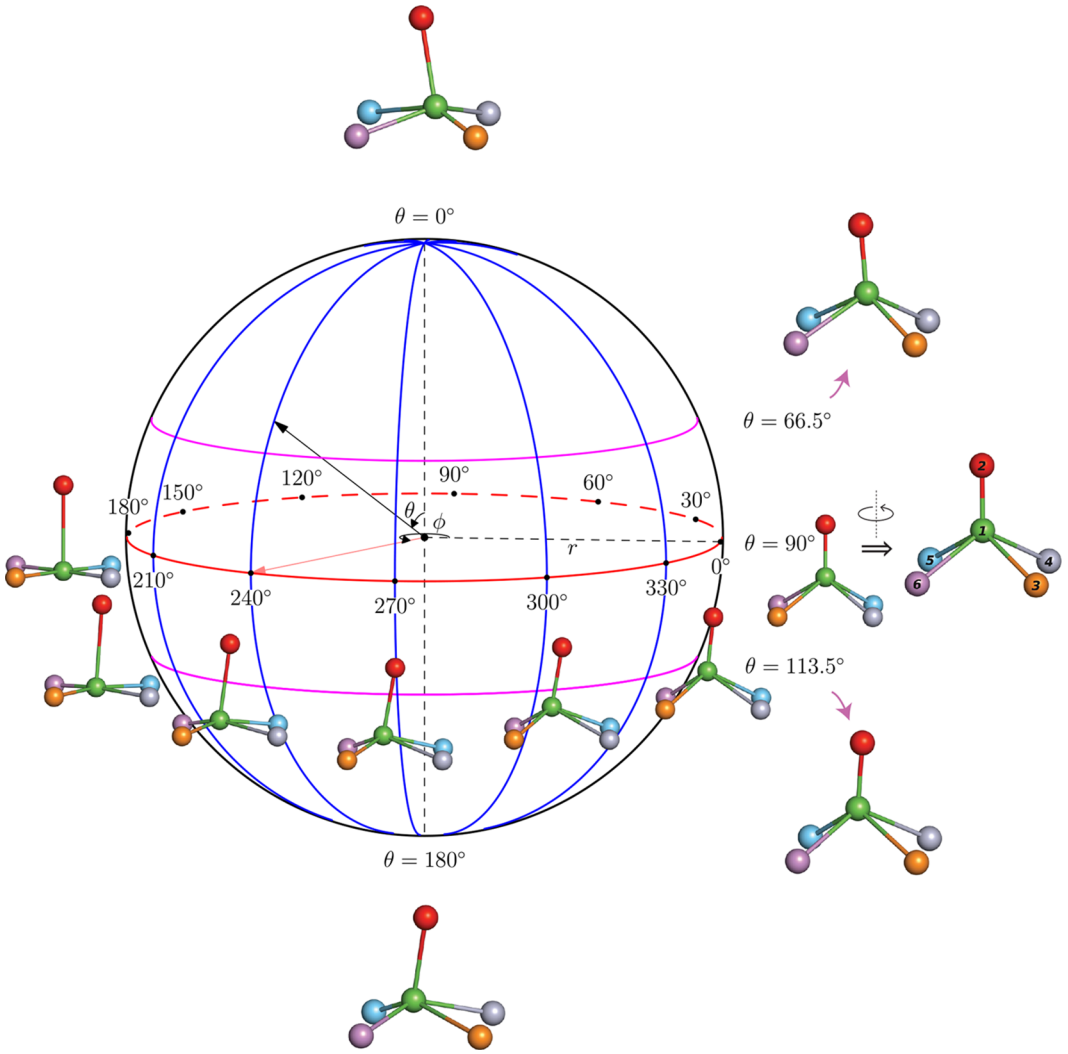

Figure 6. Conformational globe spanned by the parameter set $\{r_7, \theta_7, \phi_7\}$ specifying the translation of central atom A within the AB_5 reference system (r_1 = 1.5 Å) in C_{4v} symmetry (see Table 1). Any point on the globe surface has r_7 = 0.3 Å while all other r_m values (except r_1) are 0. Some distinct longitudes and latitudes are shown, including the equator (θ = 90°) in red and the Tropic of Cancer (θ = 66.5°) and the Tropic of Capricorn (θ = 113.5°) in magenta. Among five representative structures (ϕ_7 = 0°, θ_7 = 0°/66.5°/90°/113.5°/180°), bond 1−2 first shortens and then elongates (controlled by sin θ_7), bond 1−3 elongates and bond 1−5 shortens (controlled by cos θ_7) continuously from north pole to south pole. Among seven representative structures on the equator (θ_7 = 90°, ϕ_7 = 180°/210°/240°/270°/300°/330°/360°), bond 1−2 shortens (controlled by cos ϕ_7) from left to right, bond 1−6 first shortens and then elongates, and bond 1−4 changes in the opposite way (controlled by sin ϕ_7).

optimization for stationary points was carried out with a tight convergence criterion.

IRC calculations were performed in Cartesian coordinates without mass-weighting in order to map out the minimum-energy path (MEP). Most MEPs in this work were obtained using Hessian-based predictor-corrector (HPC) integrator[112−114] with a stepsize of 0.05 bohr and analytic Hessian every five steps. For larger compounds discussed in sections 4.2 and 4.3, either the GS2[115,116] or local quadratic approximation (LQA)[117,118] algorithm was employed as the path integrator, with the stepsize of 0.20−0.50 bohr.

4. RESULTS AND DISCUSSION

The Berry pseudorotation of PF_5 molecule[9,10] has been shown in Figure 5 as an example where the multidimensional PES is reduced to a 2D PES spanned by the curvilinear coordinate pair $\{r_5, \phi_5\}$ and the reaction path connecting the stationary points is then straightforwardly determined. We need to note that the choice of the reference system AB_5 in C_{4v} symmetry for this example is based on its known mechanism; i.e., the transition state takes a square pyramidal (C_{4v}) geometry. However, when investigating fluxional molecules with uncertain mechanisms, we have to start from the local minimum structures (reactants/products) on the PES. Besides, the scanned PES with two degrees of freedom can be further simplified into a 1D PES if the reaction coordinate is properly chosen.

Table 2. Curvilinear Coordinate Parameters of SF_4 at Its Equilibrium Geometry Based on the AB_4 Reference System in T_d Symmetry[a]

m	r_m	θ_m	ϕ_m
1	1.4186		
2	0.4673		270.0
3	0.2157	0.0	0.0
4	0.4493	90.0	0.0[b]

[a]Units for amplitude r_m and phase angles θ_m/ϕ_m are angstrom (Å) and degree (deg), respectively. [b]ϕ_4 = 0° is equivalent to ϕ_4 = 360°.

https://dx.doi.org/10.1021/acs.jctc.9b01274
J. Chem. Theory Comput. 2020, 16, 3162−3193

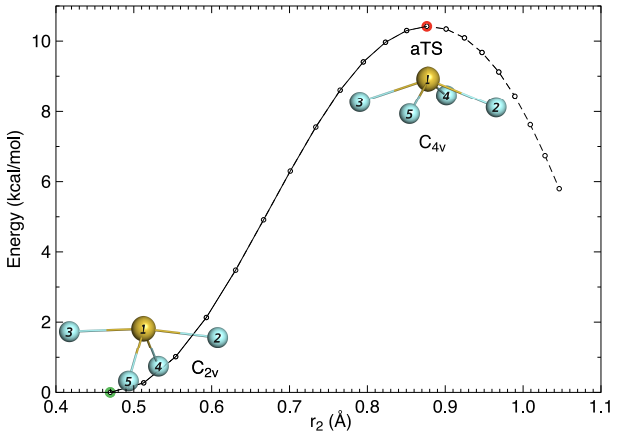

Figure 7. Potential energy curve from relaxed scan of curvilinear coordinate parameter r_2 for SF_4 molecule revealing the Berry pseudorotation. The entrance channel starts from the reactant structure highlighted in green circle toward the approximate transition state (aTS) highlighted in red color.

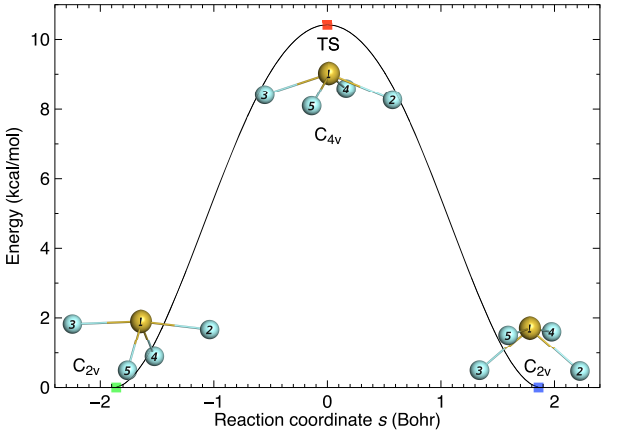

Figure 8. Energy profile along the MEP of the Berry pseudorotation of SF_4 molecule. Reactant and product are represented by green and blue squares while the TS position is denoted by the red square.

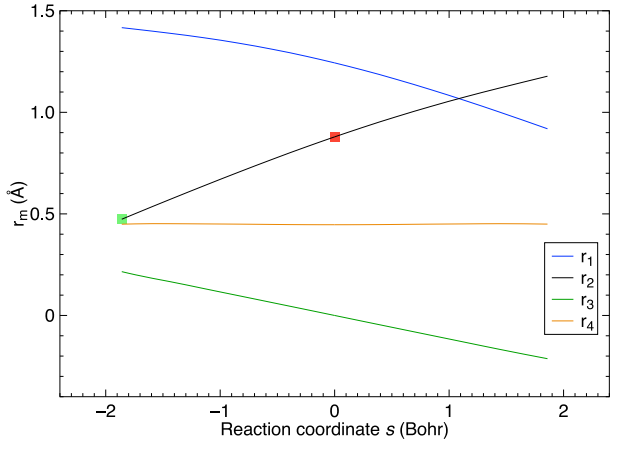

Figure 9. Variation in amplitude r_m along the MEP of the Berry pseudorotation of SF_4. The green and red squares indicate the reactant and TS. The r_2 curve including the squares is the one used to drive the reaction coordinate during relaxed PES scan.

In the following, the results of our study will be discussed in detail. We investigated a series of fluxional molecular

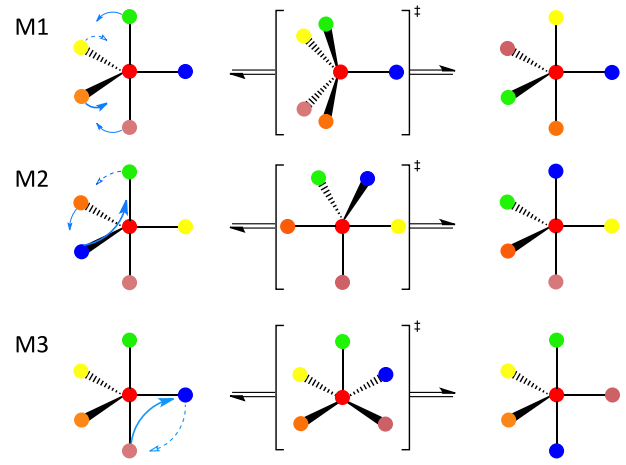

Figure 10. Three feasible permutation mechanisms for pentavalent bipyramidal structures proposed by Muetterties. Mechanism **M1** is Berry pseudorotation. **M2** involves a 3-fold (120°) cyclic permutation and resembles the motion of a three-arm turnstile gate. **M3** resembles a two-arm turnstile and involves a half-twist axial−equatorial interchange. Both **M1** and **M3** have a TS with square pyramid geometry, while **M2** has a trigonal bipyramidal TS.

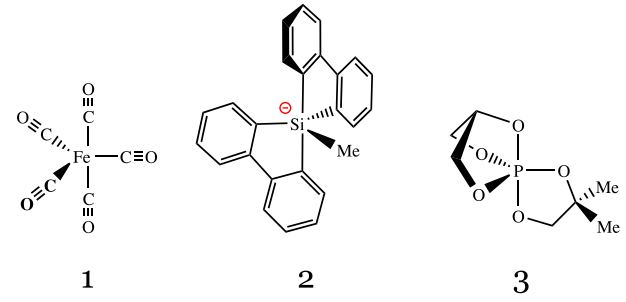

1 **2** **3**

Figure 11. Three pentacoordinate compounds used to illustrate three different stereomutation mechanisms **M1** through **M3**, respectively, in Figure 10. **1**, iron pentacarbonyl;[135] **2**, a spirocyclic pentaorganylsilicate;[136] **3**, a caged phosphorane.[137]

Table 3. Curvilinear Coordinates of the Core Fragment of 1 at Its Equilibrium Geometry Based on the AB_5 Reference System in D_{3h} Symmetry[a]

m	r_m	θ_m	ϕ_m
1	1.8116		
2	0.0029		
3	0.0003		180.0
4	0.0002		0.0
5	0.0005	180.0	0.0
6	0.0000	180.0	0.0

[a]Units for amplitude r_m and phase angles θ_m/ϕ_m are angstrom (Å) and degree (deg), respectively.

compounds with N-coordinate geometry, N = 4−7, to demonstrate how the new curvilinear coordinates derived from normal vibrational modes can facilitate the description of polytopal rearrangements, focusing (i) on the chemical kinetics of these processes and (ii) on determining all transition states (TS) and mapping the corresponding reaction pathways on the PES.

4.1. Berry Pseudorotation of Sulfur Tetrafluoride (SF_4).

Sulfur tetrafluoride (SF_4), first reported in 1911,[119] has a seesaw (C_{2v}) geometry. On the basis of ^{19}F NMR data recorded at

https://dx.doi.org/10.1021/acs.jctc.9b01274
J. Chem. Theory Comput. 2020, 16, 3162−3193

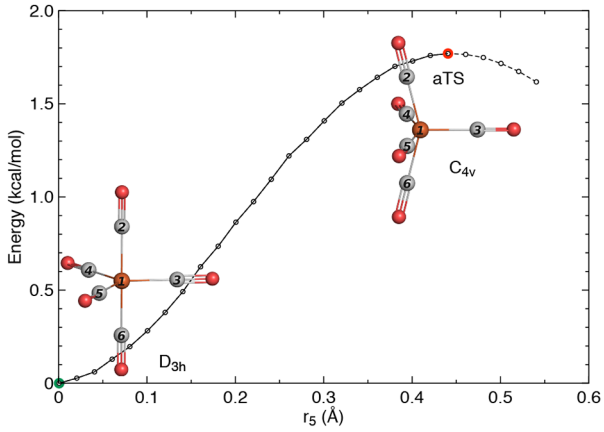

Figure 12. Potential energy curve from relaxed scan of curvilinear coordinate parameter r_5 for **1** along the Berry pseudorotation path. The entrance channel starts with reactant (green circle) toward the aTS (red circle).

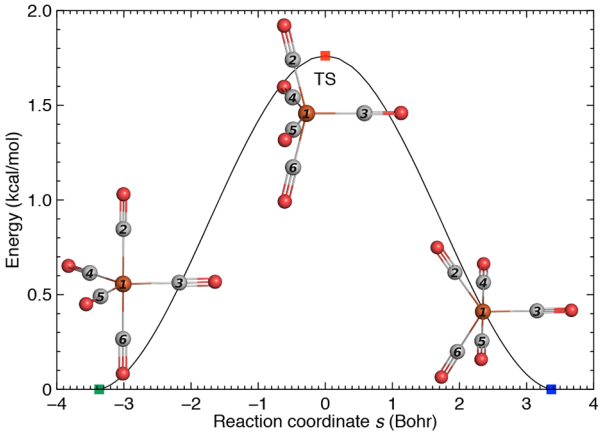

Figure 13. Energy profile along the MEP of the Berry pseudorotation for **1**. Reactant, TS, and product are marked with green, red, and blue squares, respectively.

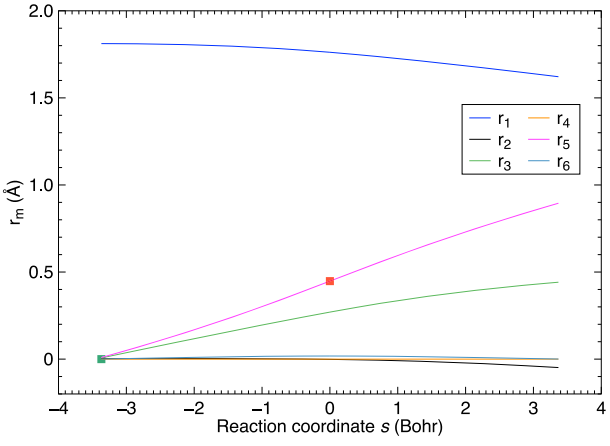

Figure 14. Change of amplitude r_m along the MEP of the Berry pseudorotation of **1**. The green and red squares indicate the reaction coordinates for reactant and TS, and the amplitude r_5 with these squares is the chosen variable in relaxed PES scan.

different temperatures, SF_4 is considered fluxional as it undergoes fast exchange of ligand positions at room temperature.[120−122] Klemperer and co-workers concluded in 1975[123]

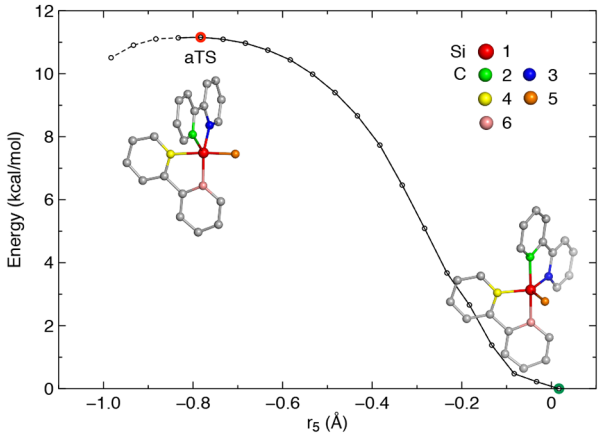

Figure 15. Potential energy curve from the relaxed scan of curvilinear coordinate r_5 for **2**. Green and red circles on the curve indicate the reactant and aTS respectively. Hydrogen atoms are not shown in the ball-and-stick representations.

Table 4. Curvilinear Coordinates of the Core Fragment within 2 at Its Equilibrium Geometry Based on the AB_5 Reference System in D_{3h} Symmetry[a]

m	r_m	θ_m	ϕ_m
1	1.9811		
2	0.0533		
3	0.0159		42.6
4	0.1041		339.9
5	0.0176	41.4	8.9
6	0.0213	101.9	308.3

[a]Units for amplitude r_m and phase angles θ_m/ϕ_m are angstrom (Å) and degree (deg), respectively.

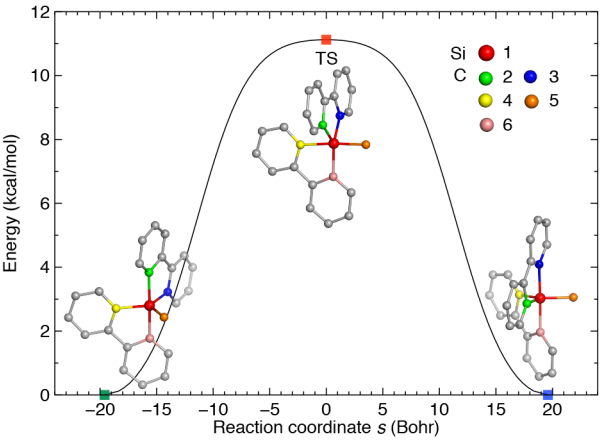

Figure 16. Energy profile along the MEP of Muetterties mechanism **M2** for **2**. Reactant, TS, and product are marked with green, red, and blue squares respectively.

that the nonrigidity of SF_4 arises from Berry pseudorotation,[9,10] where the axial F−S−F angle closes accompanied by the opening of the equatorial F−S−F angle, passing through a TS with C_{4v} symmetry.

We used the curvilinear coordinates derived from the AB_4 reference system in T_d symmetry (see Appendix A.2) to describe the Berry mechanism of SF_4 pseudorotation. Ideally, a tetracoordinate reference system in C_{2v} symmetry would best fit the symmetry of SF_4. However, by definition, the reference

https://dx.doi.org/10.1021/acs.jctc.9b01274
J. Chem. Theory Comput. 2020, 16, 3162−3193

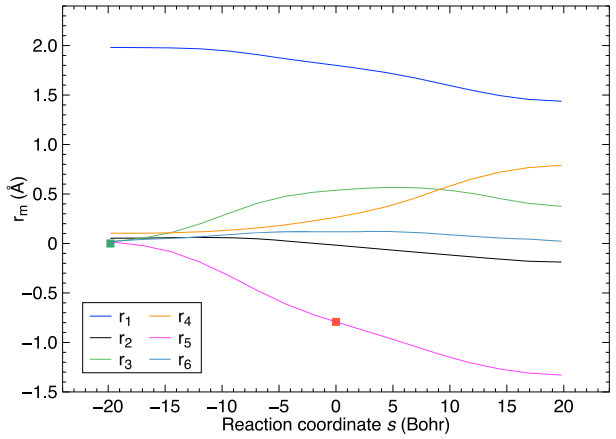

Figure 17. Changes in the amplitude r_m along the MEP of Muetterties mechanism **M2** of **2**. The green and red squares represent the reactant and TS, and the amplitude r_5 with these squares is the chosen variable in relaxed PES scan.

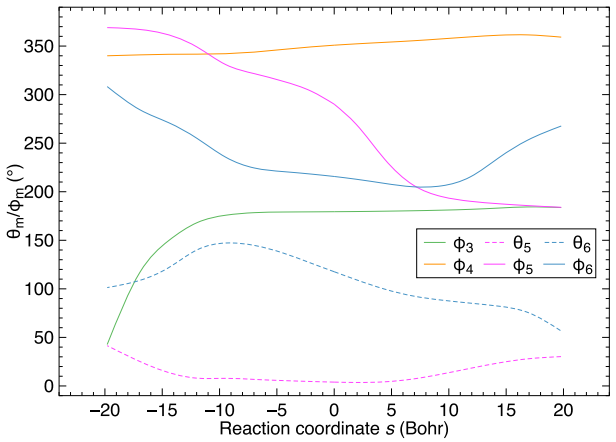

Figure 18. Variation of the phase angles θ_m/ϕ_m along the MEP of Muetterties mechanism **M2** of **2**.

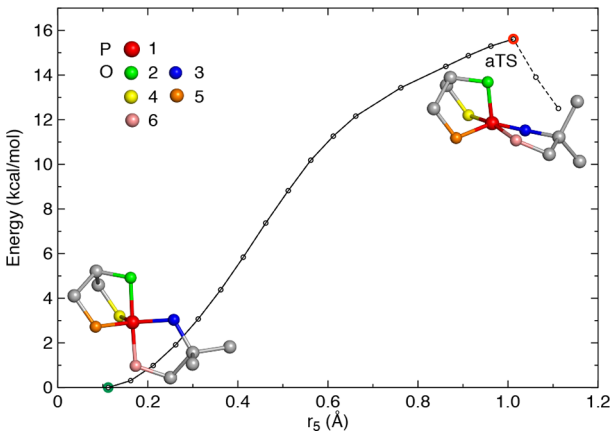

Figure 19. Potential energy curve from relaxed scan of curvilinear coordinate r_5 for **3**. Reactant and aTS points are indicated by the green and red circles, respectively.

system is required to position the central atom A at the geometrical center. Under this constraint, for SF_4 the AB_4 reference system with T_d symmetry is the only solution.

The two axial fluorine atoms were labeled as the first two ligands (atoms 2 and 3), and the optimized geometry of SF_4 was

Table 5. Curvilinear Coordinates of the Core Fragment of 3 at Its Equilibrium Geometry Based on the AB_5 Reference System in D_{3h} Symmetry[a]

m	r_m	θ_m	ϕ_m
1	1.6476		
2	0.0325		
3	0.1318		19.2
4	0.0143		68.0
5	0.1169	30.0	255.2
6	0.0593	34.3	198.9

[a]Units for amplitude r_m and phase angles θ_m/ϕ_m are angstrom (Å) and degree (deg), respectively.

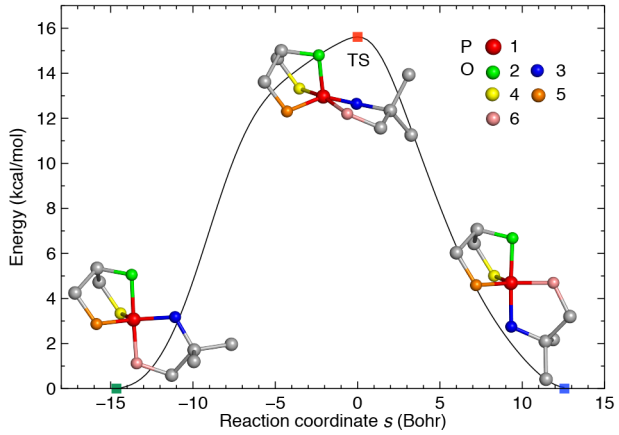

Figure 20. Energy profile along the MEP of Muetterties mechanism **M3** for **3**. The green, red, and blue squares represent the reactant, TS, and product respectively.

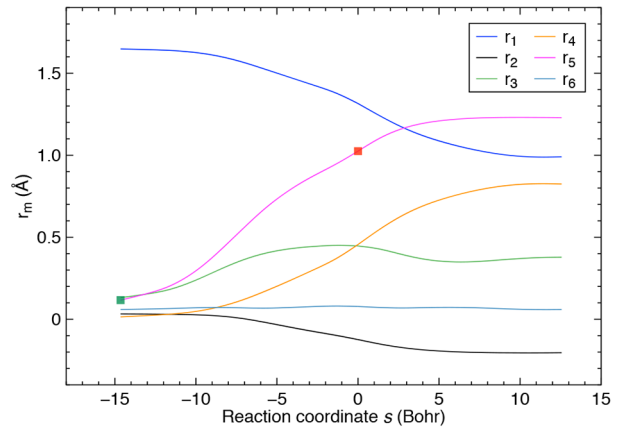

Figure 21. Variation of the amplitude r_m along the MEP of Muetterties mechanism **M3** of **3**. The green and red squares represent reactant and TS; the amplitude r_5 is the chosen variable for relaxed PES scan.

then expressed in curvilinear coordinates collected in Table 2. The amplitude r_1 defines the overall size of SF_4 structure while the remaining r_m values specify to what extent the geometry deviates from the reference system with T_d symmetry. The parameter set $\{r_2, \phi_2\}$ has a positive amplitude and a phase angle $\phi_2 = 270°$. This implies that SF_4 geometry has a dominating contribution from the third normal vibrational mode in reverse direction ($\sin \phi_2 = -1$) and no contribution from the second normal mode ($\cos \phi_2 = 0$) relative to the reference geometry in T_d symmetry (see Table 10 in Appendix A.2). Similarly, the

https://dx.doi.org/10.1021/acs.jctc.9b01274
J. Chem. Theory Comput. 2020, 16, 3162−3193

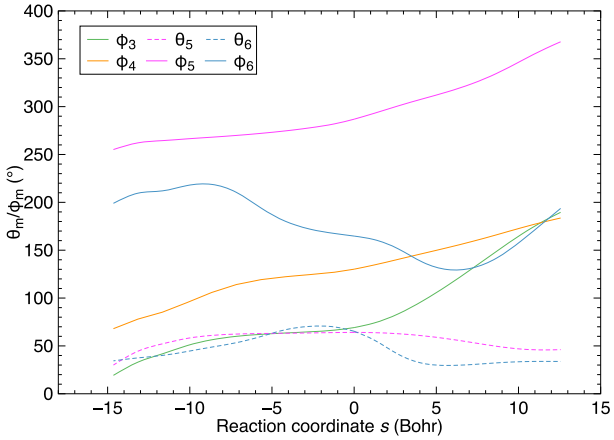

Figure 22. Variation of the phase angles θ_m/ϕ_m along the MEP of Muetterties mechanism **M3** for **3**.

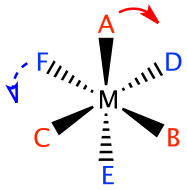

Figure 23. Schematic representation of twist about a C_3 axis in an octahedral structure. The rotational axis is perpendicular to the paper plane passing through the central atom M. The arrows define the twist direction as clockwise.

Table 6. Four Representative Solutions to Eq 22 and Corresponding Twist Motions

	phase angles (deg)		twist motion[a]	
no.	θ_4	ϕ_4	(ABC)-(DEF)	clockwise
1	54.7	45.0	(2,5,4)-(6,7,3)	−
2	54.7	135.0	(2,3,6)-(4,7,5)	+
3	125.3	45.0	(2,4,3)-(5,7,6)	+
4	125.3	135.0	(2,6,5)-(3,7,4)	−

[a]The twist motion of the octahedral reference system is defined according to the scheme in Figure 23. A, B, and C are three atoms sticking out of the plane of the paper while D, E, and F are the other three atoms into the plane of the paper. The clockwise (+) twist direction is defined in the same figure given a positive r_4 value and the anticlockwise (−) is the other way around.

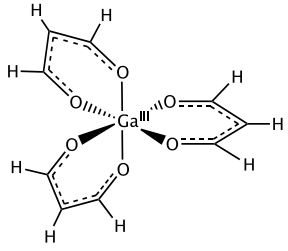

Figure 24. Structure of trismalondialdehydegallium(III) in Λ chirality, abbreviated as Λ-$Ga^{III}(mda)_3$.

phase angles within the parameter set $\{r_3, \theta_3, \phi_3\}$ show that the fourth normal vibration fully contributes to the SF_4 geometry ($\cos\theta_3 = 1$), in contrast to zero contributions ($\sin\theta_3 = 0$) from the fifth and sixth normal modes. The parameter set $\{r_4, \theta_4, \phi_4\}$ indicates that the ninth vibrational mode is contributing to the

Table 7. Curvilinear Coordinates of the Core Fragment of Λ-$Ga^{III}(mda)_3$ at Its Equilibrium Geometry Based on the AB_6 Reference System in O_h Symmetry[a]

m	r_m	θ_m	ϕ_m
1	1.9848		
2	0.0000		0.0
3	0.0159	125.3	135.0
4	0.0233	54.7	135.0
5	0.0000	0.0	0.0
6	0.0000	0.0	0.0

[a]Units for amplitude r_m and phase angles θ_m/ϕ_m are Angstrom (Å) and degree (deg), respectively.

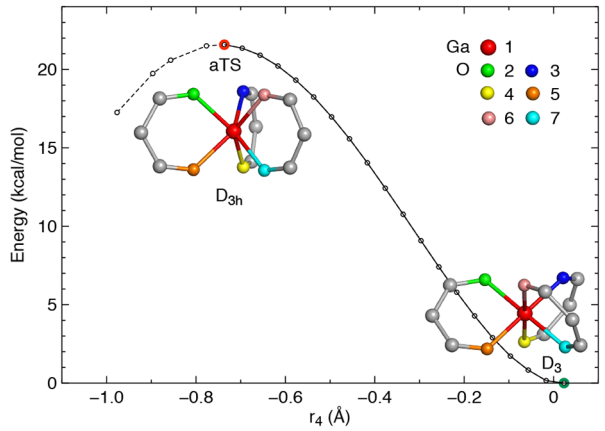

Figure 25. Potential energy curve from the relaxed PES scan of curvilinear coordinate r_4 for Λ-$Ga^{III}(mda)_3$. Reactant and aTS points are indicated by the green and red circles, respectively.

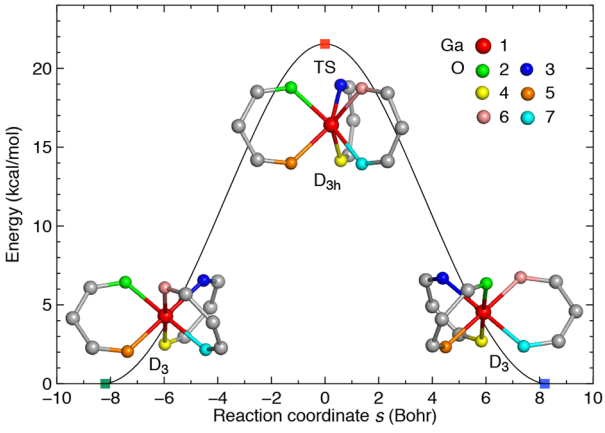

Figure 26. Energy profile along the MEP of Bailar twist from Λ-$Ga^{III}(mda)_3$ to Δ-$Ga^{III}(mda)_3$ (left to right). The green, red, and blue squares represent reactant, TS, and product, respectively.

SF_4 geometry ($\sin\theta_4 \cos\phi_4 = 1$) while the seventh ($\cos\theta_4 = 0$) and eighth ($\sin\theta_4 \sin\phi_4 = 0$) do not.

In order to model the Berry pseudorotation process, we employed the coordinate driving approach[124−129] by carrying out a relaxed PES scan of selected curvilinear coordinate(s) locating the TS in the first place. By inspection of all nine normal vibrations for the AB_4 reference system shown in Figure 44 (Appendix A.2), we found the third normal mode is closely related to the Berry process if the F atoms in SF_4 move along this mode in the opposite direction to lower the axial fluorine atoms

https://dx.doi.org/10.1021/acs.jctc.9b01274
J. Chem. Theory Comput. 2020, 16, 3162−3193

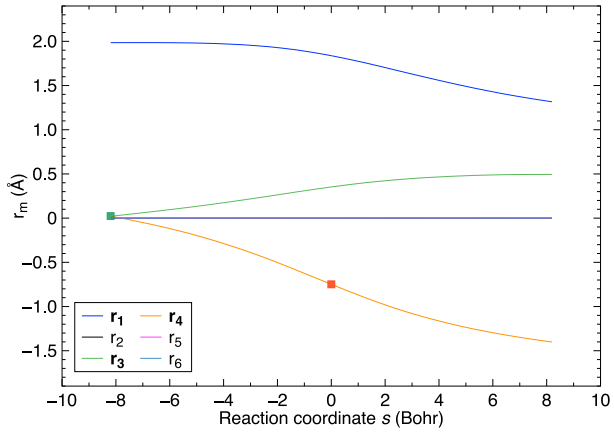

Figure 27. Variation of the amplitude r_m along the MEP of Bailar twist starting from Λ-$Ga^{III}(mda)_3$. The green and red squares represent the reactant and TS. Amplitude r_4 is the chosen variable for relaxed PES scan.

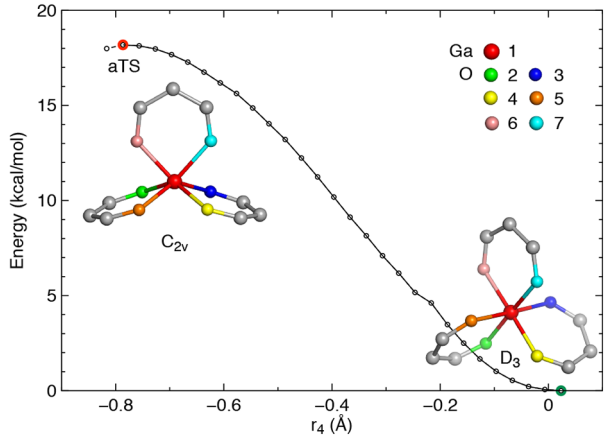

Figure 28. Potential energy curve from the relaxed PES scan of curvilinear coordinate r_4 for Λ-$Ga^{III}(mda)_3$. The aTS point is marked by a red circle, and the reactant is represented by a green circle. All points to the left of the green circle correspond to the geometries with the additional constraint $\theta_4 = 125.3°$.

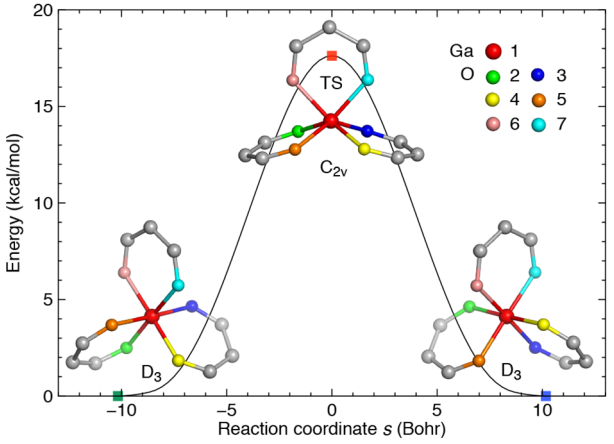

Figure 29. Energy profile along the MEP of the Ray-Dutt twist from Λ-$Ga^{III}(mda)_3$ to Δ-$Ga^{III}(mda)_3$ (left to right). The green, red, and blue squares represent the reactant, TS, and product, respectively.

and to lift up the equatorial fluorines. As the parameter set $\{r_2, \phi_2\}$ already specifies the third normal mode in the reverse

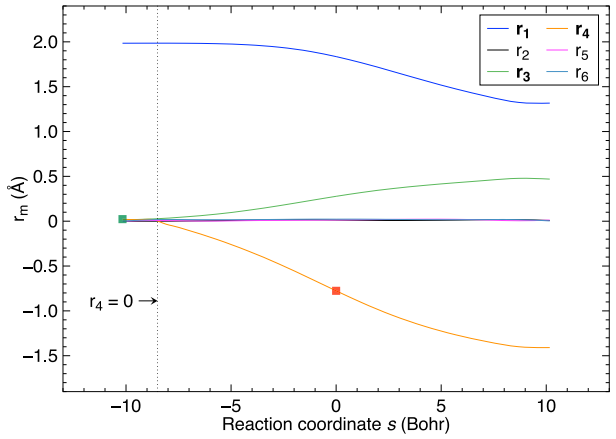

Figure 30. Variation of the amplitude r_m along the MEP of the Ray-Dutt twist starting from Λ-$Ga^{III}(mda)_3$. The green and red square represent reactant and TS. The amplitude r_4 is the chosen variable for relaxed PES scan.

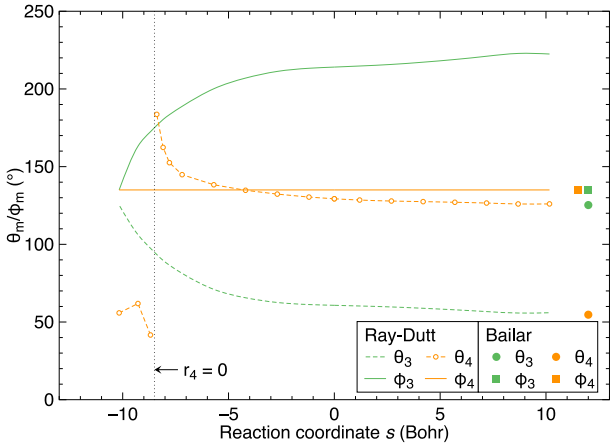

Figure 31. Variation of the phase angles θ_m/ϕ_m along the MEP of the Ray-Dutt twist from Λ-$Ga^{III}(mda)_3$ to Δ-$Ga^{III}(mda)_3$. Phase angles along the Bailar twist pathway are constant. They are marked with solid dots and squares.

Table 8. Curvilinear Coordinates of IF_7 at Its Equilibrium Geometry Based on the AB_7 Reference System in D_{5h} Symmetry[a]

m	r_m	θ_m	ϕ_m
1	1.8845		
2	−0.0376		
3	0.0001		144.0
4	0.0004		72.0
5	0.0000		180.0
6	0.0000		180.0
7	0.0000		180.0
8	0.0002	288.0	90.0
9	0.0001	288.0	90.0

[a]Units for amplitude r_m and phase angles θ_m/ϕ_m are Angstrom (Å) and degree (deg), respectively.

direction, we performed a relaxed PES scan by stepwise increasing the amplitude r_2.

As shown in Figure 7, the energy increases smoothly with an increasing r_2 value until it encounters a maximum point around $r_2 = 0.88$ Å, followed by a few points with lower energies. We did

https://dx.doi.org/10.1021/acs.jctc.9b01274
J. Chem. Theory Comput. 2020, 16, 3162−3193

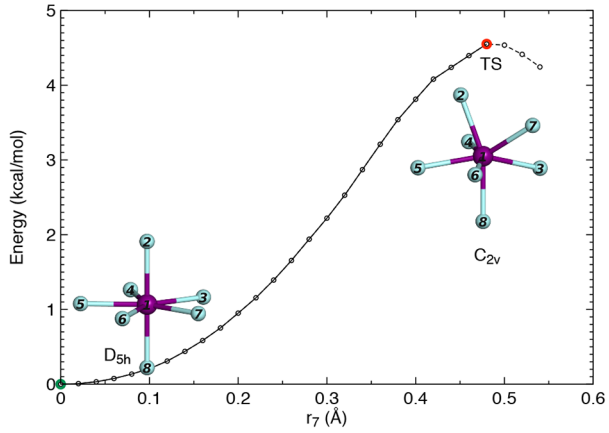

Figure 32. Potential energy curve from relaxed PES scan of curvilinear coordinate parameter r_7 for IF_7. The reactant and aTS points are indicated by the green and red circles, respectively.

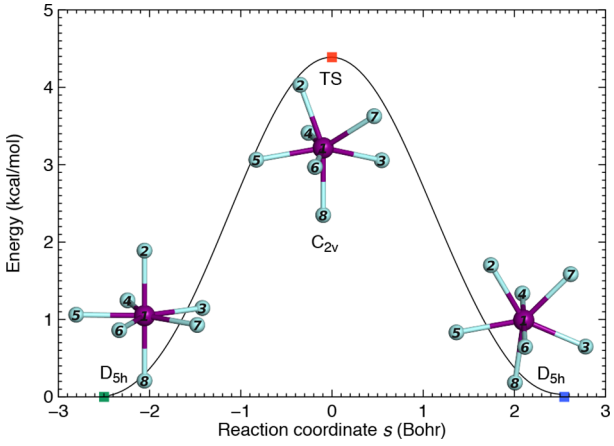

Figure 33. Energy profile along the MEP of the Bartell mechanism for IF_7. The green, red, and blue squares represent reactant, TS, and product, respectively.

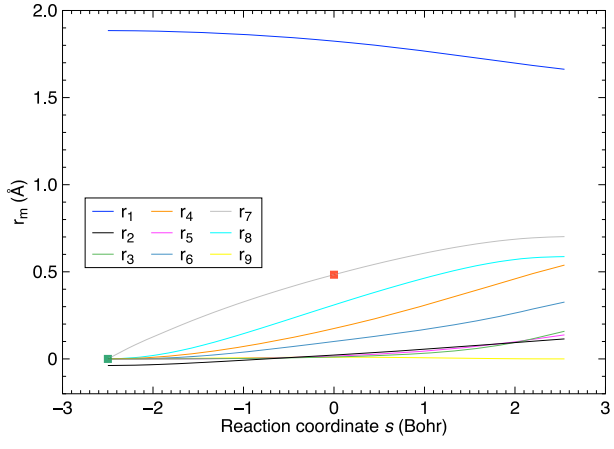

Figure 34. Variation of the amplitude r_m along the MEP of the Bartell mechanism of IF_7. The green and red squares represent the reactant and TS. The amplitude r_7 is the chosen variable for relaxed PES scan.

not continue the relaxed PES scan all the way down to reach another minimum point close to the product structure, instead the scan was terminated immediately, when an obvious maximum point was found. This strategy was based on two reasons:

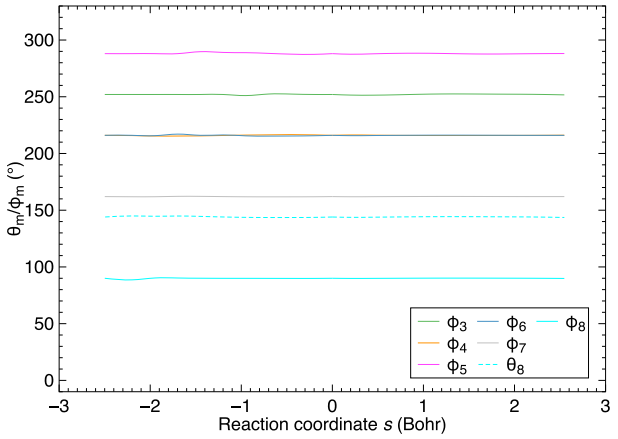

Figure 35. Variation of the phase angles θ_m/ϕ_m along the MEP of the Bartell mechanism of IF_7.

Table 9. Curvilinear Coordinates of IF_5 at Its Equilibrium Geometry Based on the AB_5 Reference System in C_{4v} Symmetry[a]

m	r_m	θ_m	ϕ_m
1	1.7844		
2	−0.4961		
3	0.0000		
4	0.0000		0.0
5	0.0000		0.0
6	0.0000		0.0
7	0.4800	90.0	180.0

[a]Units for amplitude r_m and phase angles θ_m/ϕ_m are angstrom (Å) and degree (deg), respectively.

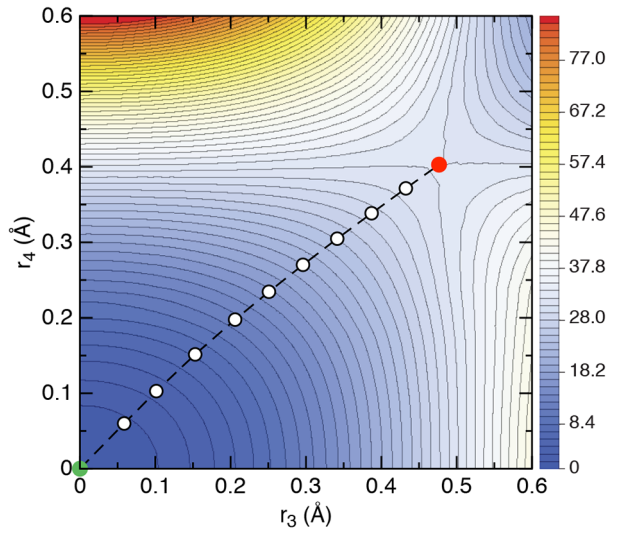

Figure 36. 2D PES of IF_5 obtained by relaxed scan of r_3 and r_4 based on the AB_5 reference system in C_{4v} symmetry. The MEP characterizing the chimeric pseudorotation is indicated by the white dots connected with a dashed line. The green dot represents the reactant while the red dot represents the aTS point. The color bar on the right side shows the energy scale in kcal/mol.

- The curvilinear coordinate selected to drive the reaction coordinate in the entrance channel might be no longer appropriate to serve in the same way for the exit channel after the TS.[125]

https://dx.doi.org/10.1021/acs.jctc.9b01274
J. Chem. Theory Comput. 2020, 16, 3162−3193

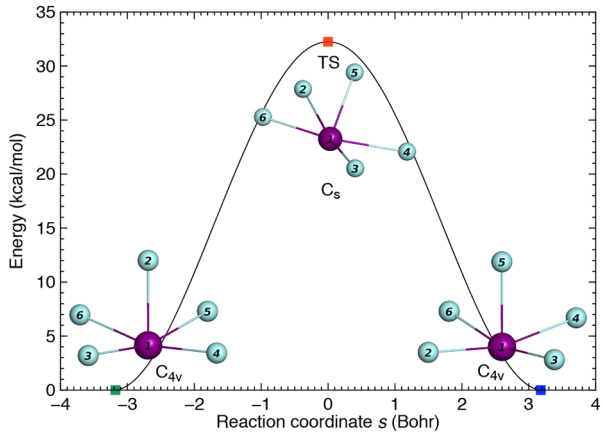

Figure 37. Energy profile along the MEP of chimeric pseudorotation for IF_5. The green, red, and blue squares represent reactant, TS, and product respectively. The mirror plane of the C_s symmetric TS equally divides both F2−I1−F5 and F3−I1−F4 angles, while containing the F6 atom.

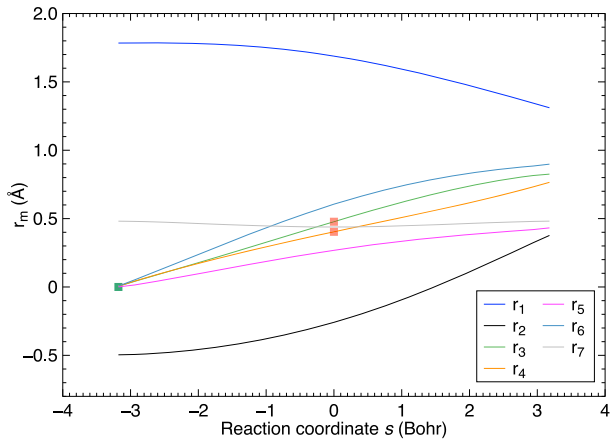

Figure 38. Variation of the amplitude r_m along the MEP of the chimeric pseudorotation of IF_5. The green and red squares represent reactant and TS, respectively. The amplitudes r_3 and r_4 are the chosen variables for relaxed PES scan.

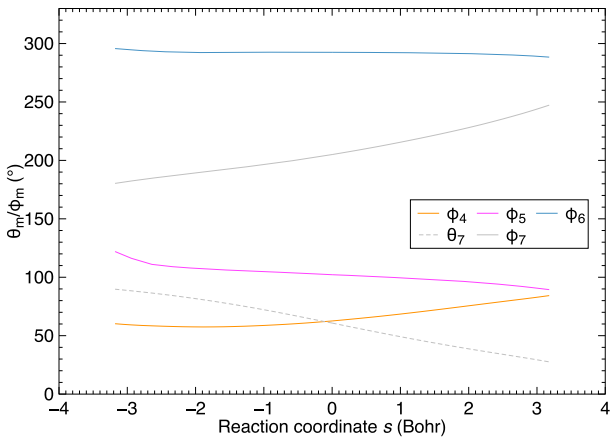

Figure 39. Variation of the phase angles θ_m/ϕ_m along the MEP of the chimeric pseudorotation of IF_5.

- The maximum point obtained from the relaxed scan is an approximate transition state (aTS) that is already close to the true transition state (TS). The TS point connects the entrance and exit channels, and the whole reaction path can be easily mapped out starting from this point by following the vibrational eigenvector with negative PES curvature. Therefore, it is unnecessary to continue the relaxed scan past the aTS point until a minimum point is found.

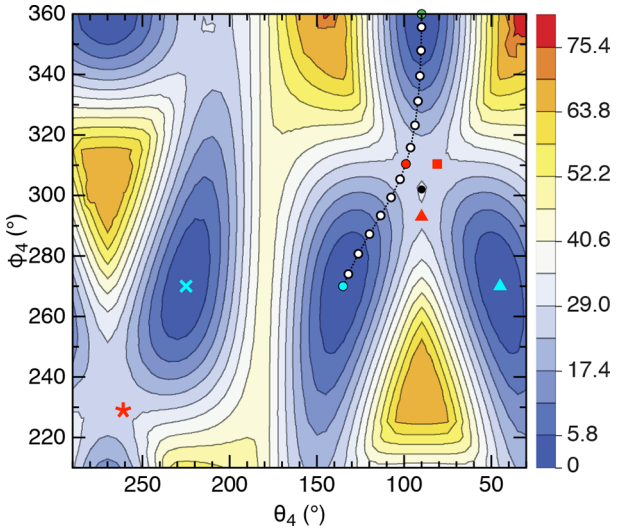

Figure 40. 2D PES of SF_4 obtained by a relaxed scan of θ_4 and ϕ_4 based on the AB_4 reference system in T_d symmetry. The MEP characterizing the lever pseudorotation mechanism is traced by the white dots connected with a dashed line. The green, red, and cyan round dots represent reactant, aTS, and product, respectively. All other cyan dots represent SF_4 in equilibrium geometry, red dots represent first-order saddle points of the lever mechanism, and the black dot represents a second-order saddle point. The color bar on the right side shows the energy scale in kcal/mol. A 3D representation of this PES is included in the Supporting Information.

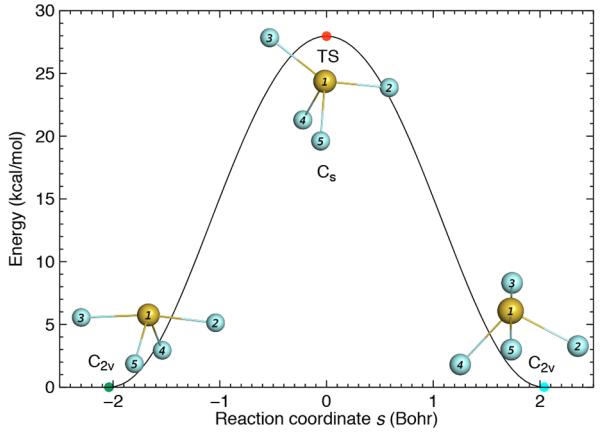

Figure 41. Energy profile along the MEP of a lever mechanism for SF_4. The green, red, and cyan round dots represent reactant, TS, and product respectively. The mirror plane of the C_s symmetric TS contains F3 and F4 atoms and halves the F2−S1−F5 angle.

We reoptimized the geometry of the SF_4 molecule at the aTS point in order to locate the first-order saddle point (TS) on the PES. Then, the minimum-energy path (MEP) was traced going downhill from the TS in two directions, toward reactant and product, respectively.

Figure 8 shows the energy profile as a function of the reaction coordinate s, which is symmetric with regard to $s = 0$. The

https://dx.doi.org/10.1021/acs.jctc.9b01274
J. Chem. Theory Comput. 2020, 16, 3162−3193

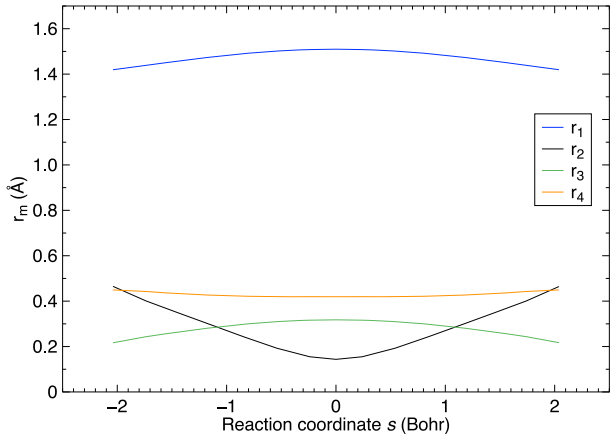

Figure 42. Variation of the amplitude r_m along the MEP of the lever mechanism of SF_4.

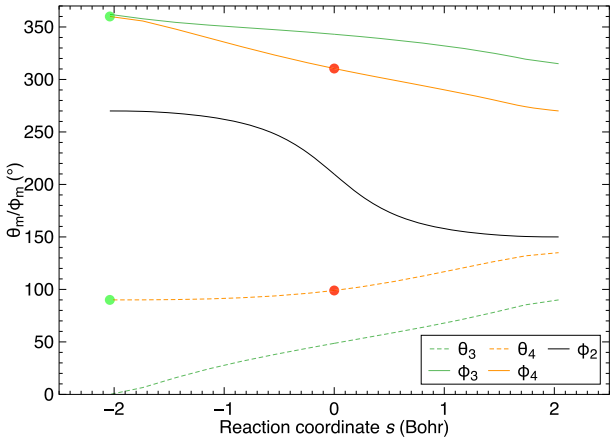

Figure 43. Variation of the phase angles θ_m/ϕ_m along the MEP of the lever mechanism of SF_4. The green and red dots represent reactant and TS, respectively. θ_4 and ϕ_4 are the chosen variables for relaxed PES scan.

calculated barrier height (without thermal correction) is 10.4 kcal/mol, being qualitatively consistent with experimentally measured activation free energy of 12.2 kcal/mol.[130]

We also monitored the variation of the curvilinear coordinates along the MEP of the Berry pseudorotation. Interestingly, we found that all phase angles θ_m/ϕ_m do not change along the whole reaction process, as indicated in Table 2 for the reactant geometry. Figure 9 shows how each amplitude value r_m changes with the reaction progress.

The amplitude r_2 chosen as the driving coordinate in the relaxed PES scan shows the most significant change along the path, it increases by 0.7 Å, while r_1 and r_3 both decrease by 0.5 Å. The amplitude r_4, associated with relative translation between the central S atom and four ligating F atoms does not change. In addition, this result indicates that the amplitude r_3 could be another parameter to be scanned when locating the aTS point (by decreasing it) as the parameter set $\{r_3, \theta_3, \phi_3\}$ at the reactant geometry specifies the fourth normal vibration, which corresponds to the lengthening of axial F··· F distance and shortening of equatorial F··· F distance (see Figure 44 in Appendix A.2).

An alternative fluxional process to the Berry pseudorotation of SF_4 molecule is the *lever mechanism*, which will be discussed below in section 4.5.2.

4.2. Berry Pseudorotation and Muetterties' Mechanisms of Pentacoordinate Trigonal-Bipyramidal Compounds. The stereomutation of pentacoordinate compounds has fascinated chemists since the 1950s, when the fluxionality of PF_5 in solution was first discovered.[131] In 1960, Berry proposed a pseudorotation mechanism for the PF_5 molecule with trigonal bipyramidal (D_{3h}) geometry, where two axial F atoms and two equatorial F atoms are interconverted via a square pyramidal (C_{4v}) transition state (see Figure 5).[9,10] After an increasing number of trigonal bipyramidal compounds exhibiting fluxionality had been synthesized, Muetterties derived five permutation mechanisms interchanging the position of the ligands in the trigonal bipyramidal geometry.[6,132] However, two out of these five mechanisms are unlikely to happen due to high energy barriers. The remaining three mechanisms **M1**−**M3** are shown in Figure 10. Complementary to the Berry pseudorotation, Ugi and co-workers proposed a turnstile rotation mechanism to account for the stereomutation in a caged oxyphosphorane compound, where three out of five groups are rotated by 60° with regard to the other two.[133]

In 2010, Couzijn and co-workers revisited the polytopal rearrangements in a series of trigonal bipyramidal compounds with quantum chemical calculations and came to several assertions, which refreshed our view on the mechanistic detail in terms of atomic motions in pentavalent compounds.[18,134] The authors proved that Ugi's turnstile rotation in the caged oxyphosphorane structure is simply a Berry pseudorotation with lower symmetry by examining its topology parameter (i.e., difference between axial biting angle and equatorial biting angle) along the reaction path. They re-evaluated the three possible mechanisms **M1**−**M3** suggested by Muetterties (see Figure 10) with topology parameter and found that mechanisms **M2** and **M3** can be decomposed into two and three consecutive Berry pseudorotations respectively, although only one transition state exists.

In this work, we revisited Muetterties' three mechanisms **M1**−**M3** each exemplified by a pentacoordinate compound (see Figure 11) with our new curvilinear coordinates.

4.2.1. Berry Pseudorotation M1. **1** has a D_{3h} geometry; therefore, the Fe and C atoms are labeled in accordance with the AB_5 reference system with D_{3h} symmetry, leading to the curvilinear coordinates of **1** in Table 3. The optimized geometry of core fragment (central Fe atom and its first coordination sphere, i.e., C atoms) of **1** is very close to that of the reference system, as the amplitudes r_2 through r_6 are literally zero. We found that the seventh normal vibrational mode of the reference system (see Appendix A.3) is directly related to a Berry pseudorotation process, if this mode moves in the opposite direction. Coincidently, the parameter set $\{r_5, \theta_5, \phi_5\}$ in **1** corresponds exactly to the seventh normal mode ($\cos\theta_5 = -1$) and a relaxed PES scan for increasing r_5 ensures driving the whole compound toward Berry pseudorotation process, as shown in Figure 12.

After locating the TS, we mapped out the MEP of the Berry pseudorotation for this system as shown in Figure 13. Examination of the curvilinear coordinates along the MEP revealed that all phase angles (θ_m/ϕ_m) do not change compared to the reactant geometry, which is in the same situation as found for the Berry pseudorotation of SF_4 discussed above. From the variation of the amplitude values shown in Figure 14, we found that amplitude r_5 has the largest increase followed by r_3. This result demonstrates that the seventh normal mode intrinsically corresponds to a Berry pseudorotation process, qualifying this

https://dx.doi.org/10.1021/acs.jctc.9b01274
J. Chem. Theory Comput. 2020, 16, 3162−3193

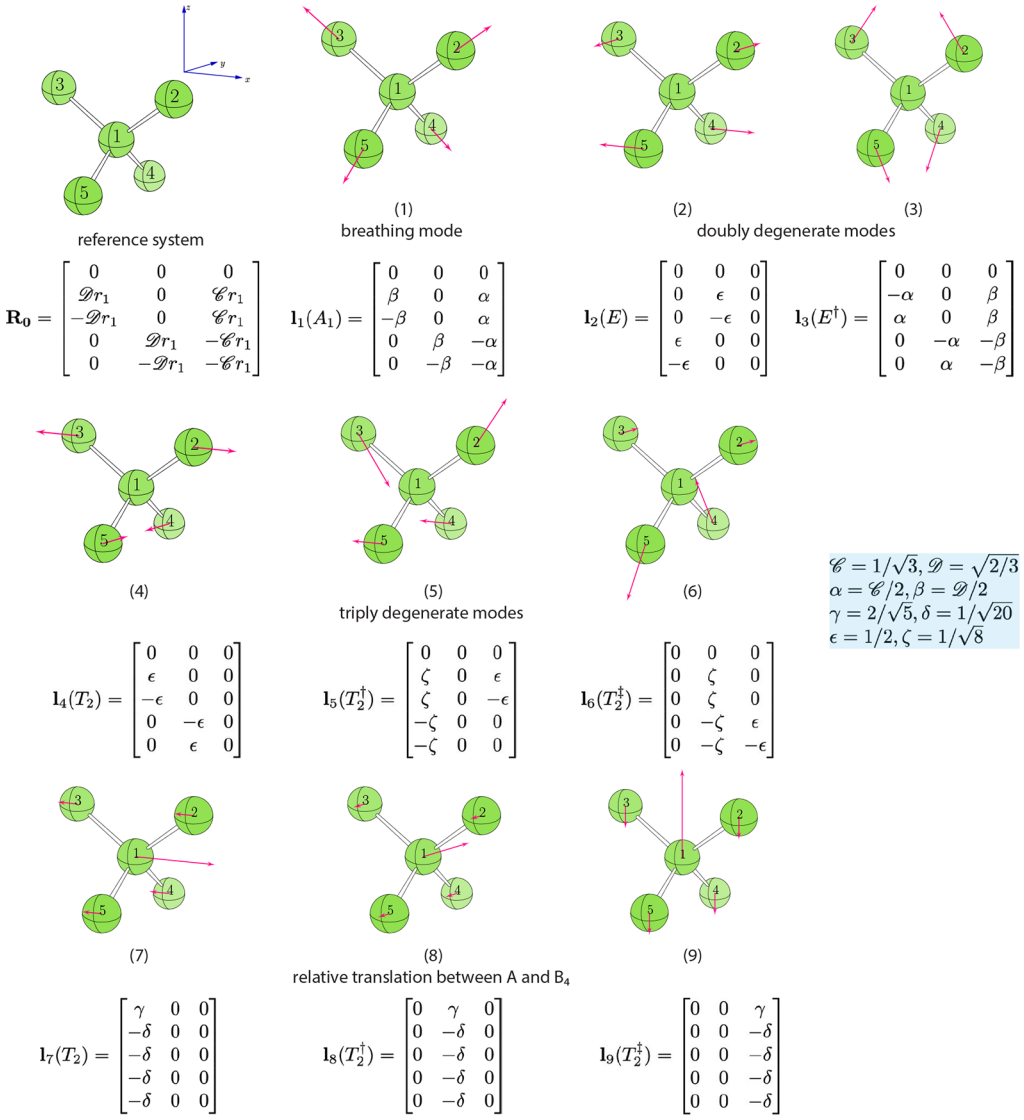

Figure 44. List of 9 normal vibrational modes for AB_4 reference system with T_d symmetry. Below the ball-and-stick representations are the labels and brief descriptions of the normal modes. The irreducible representation and the mode vector for each vibration are also shown.

mode as suitable parameter for a relaxed PES scan. The reason why r_3 has a significant change is because the third normal mode in the opposite direction ($\cos \phi_3 = -1$) corresponds to the opening of the equatorial C−Fe−C bite angle (see Figure 45 in Appendix A.3), which is also observed in the Berry pseudorotation. The changes in the amplitude values of r_2, r_4, and r_6 are only marginal.

4.2.2. Muetterties Mechanism M2. According to the work of Couzijn, Lammertsma, and co-workers,[18] the seemingly complicated 3-fold cyclic permutation mechanism **M2** consists of two consecutive Berry pseudorotation steps. Following this idea, we first identified in **2** the pivot atom, which does not participate the Berry pseudorotation involving the other four ligating atoms. As shown in Figure 15, we chose one equatorial carbon atom of a biphenyl-2,2′-diyl group as the pivot atom (no. 3) and the other atoms were labeled according to the reference system. Then the geometry of the core fragment in **2** is expressed in curvilinear coordinates shown in Table 4.

As revealed from the previous example, the seventh normal mode of the AB_5 reference system with D_{3h} symmetry is closely related to a Berry pseudorotation. The curvilinear coordinates can ideally describe the Berry mechanism if the phase angle θ_5 is expected to be close to 180° while r_5 is positive. We found that in the reactant geometry of **2** (see Table 4) the amplitude r_5 is positive. $\cos \theta_5 = 0.75$ reveals the dominance of the seventh normal vibration over the eighth ($\sin \theta_5 \sin \phi_5 = 0.10$) and ninth ($\sin \theta_5 \cos \phi_5 = 0.65$) vibrations because 0.75 is closer to 1. However, the phase angle θ_5 specifies a reverse direction toward the desired Berry pseudorotation path. A simple solution to mitigate this issue is to push the amplitude r_5 into the negative direction. Therefore, we carried out a relaxed PES scan for **2** by decreasing the amplitude r_5 as shown in Figure 15 and the aTS point pertaining to mechanism **M2** was successfully located.

After the refinement of the TS point, the complete reaction path shown in Figure 16 was mapped out. Figures 17 and 18 show how the curvilinear coordinates (i.e., amplitudes and phase angles) change along the MEP.

Amplitude r_5 shows the largest variation with a steady decline along the whole path, r_3 starts to increase in the middle of the entrance channel while the increase of r_4 becomes obvious in the exit channel. We were particularly interested in the parameter set $\{r_5, \theta_5, \phi_5\}$ monitoring its contribution from the seventh normal

https://dx.doi.org/10.1021/acs.jctc.9b01274
J. Chem. Theory Comput. 2020, 16, 3162−3193

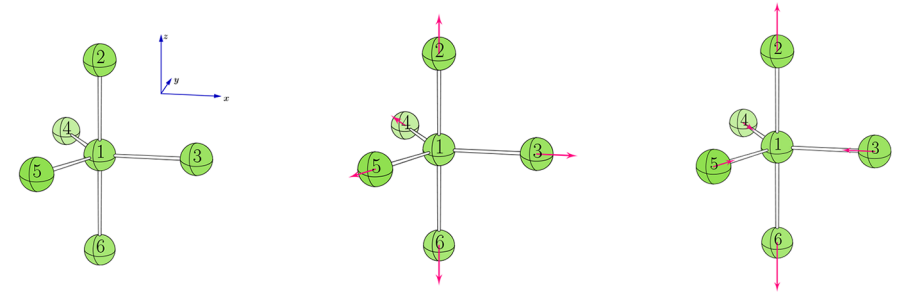

reference system (1) breathing mode (2) anti-breathing mode

$$\mathbf{R_0} = \begin{bmatrix} 0 & 0 & 0 \\ 0 & 0 & r_1 \\ r_1 & 0 & 0 \\ \mathscr{C}_1 r_1 & \mathscr{G}_1 r_1 & 0 \\ \mathscr{C}_2 r_1 & \mathscr{G}_2 r_1 & 0 \\ 0 & 0 & -r_1 \end{bmatrix} \quad \mathbf{l}_1(A_1') = \begin{bmatrix} 0 & 0 & 0 \\ 0 & 0 & \alpha \\ \alpha & 0 & 0 \\ -\beta & \gamma & 0 \\ -\beta & -\gamma & 0 \\ 0 & 0 & -\alpha \end{bmatrix} \quad \mathbf{l}_2(A_1') = \begin{bmatrix} 0 & 0 & 0 \\ 0 & 0 & \delta \\ -\epsilon & 0 & 0 \\ \pi & -\iota & 0 \\ \pi & \iota & 0 \\ 0 & 0 & -\delta \end{bmatrix}$$

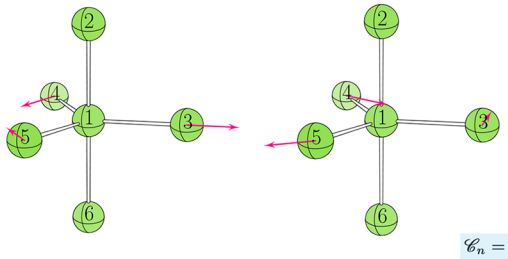

(3) (4) (t_1, τ_1) deformation of B_3 ring

$$\mathbf{l}_3(E') = \begin{bmatrix} 0 & 0 & 0 \\ 0 & 0 & 0 \\ \zeta & 0 & 0 \\ -\theta & -\eta & 0 \\ -\theta & \eta & 0 \\ 0 & 0 & 0 \end{bmatrix} \quad \mathbf{l}_4(E'^{\dagger}) = \begin{bmatrix} 0 & 0 & 0 \\ 0 & 0 & 0 \\ 0 & \zeta & 0 \\ \eta & -\theta & 0 \\ -\eta & -\theta & 0 \\ 0 & 0 & 0 \end{bmatrix}$$

$\mathscr{C}_n = cos(\frac{2n\pi}{3}), \mathscr{G}_n = sin(\frac{2n\pi}{3})$
$\alpha = \sqrt{1/5}, \beta = \sqrt{1/20}, \gamma = \sqrt{3/20}, \delta = \sqrt{3/10}, \epsilon = \sqrt{2/15}$
$\eta = 1/2, \theta = \sqrt{1/12}, \iota = \sqrt{1/10}, \zeta = \sqrt{1/3}, \pi = \sqrt{1/30}$
$\rho = \sqrt{5/6}, \kappa = \sqrt{3/14}, \lambda = \sqrt{2/7}, \mu = \sqrt{8/21}, \nu = \sqrt{2/21}$

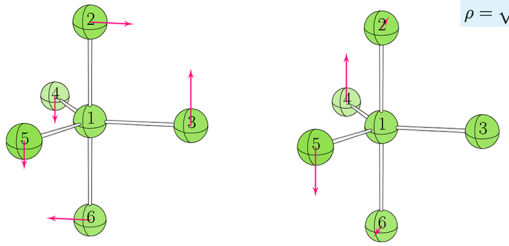

(5) (6) relative rotation

$$\mathbf{l}_5(E'') = \begin{bmatrix} 0 & 0 & 0 \\ \kappa & 0 & 0 \\ 0 & 0 & \mu \\ 0 & 0 & -\nu \\ 0 & 0 & -\nu \\ -\kappa & 0 & 0 \end{bmatrix} \quad \mathbf{l}_6(E''^{\dagger}) = \begin{bmatrix} 0 & 0 & 0 \\ 0 & \kappa & 0 \\ 0 & 0 & 0 \\ 0 & 0 & \lambda \\ 0 & 0 & -\lambda \\ 0 & -\kappa & 0 \end{bmatrix}$$

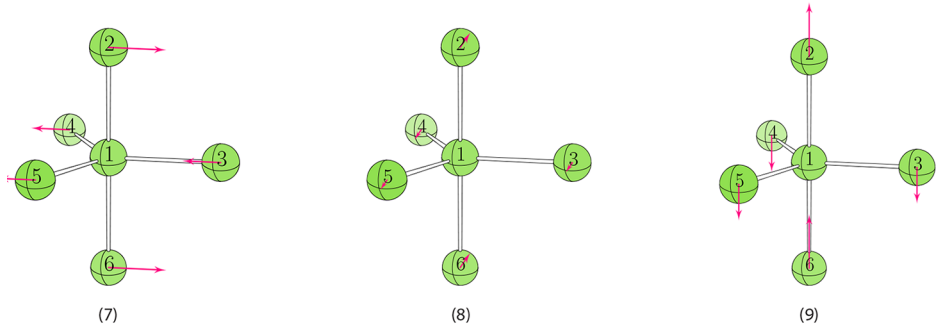

(7) (8) (9) pseudo-triply-degenerate translation between (B2, B6) and (B3, B4, B5)

$$\mathbf{l}_7(E') = \begin{bmatrix} 0 & 0 & 0 \\ \delta & 0 & 0 \\ -\epsilon & 0 & 0 \\ -\epsilon & 0 & 0 \\ -\epsilon & 0 & 0 \\ \delta & 0 & 0 \end{bmatrix} \quad \mathbf{l}_8(E'^{\dagger}) = \begin{bmatrix} 0 & 0 & 0 \\ 0 & \delta & 0 \\ 0 & -\epsilon & 0 \\ 0 & -\epsilon & 0 \\ 0 & -\epsilon & 0 \\ 0 & \delta & 0 \end{bmatrix} \quad \mathbf{l}_9(A_2'') = \begin{bmatrix} 0 & 0 & 0 \\ 0 & 0 & \delta \\ 0 & 0 & -\epsilon \\ 0 & 0 & -\epsilon \\ 0 & 0 & -\epsilon \\ 0 & 0 & \delta \end{bmatrix}$$

Figure 45. continued

https://dx.doi.org/10.1021/acs.jctc.9b01274
J. Chem. Theory Comput. 2020, 16, 3162−3193

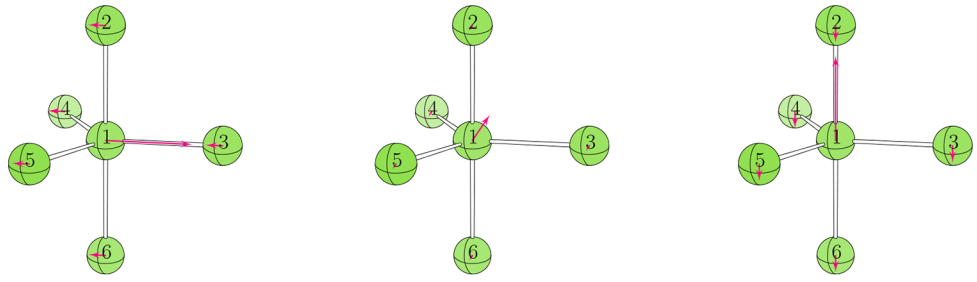

$$\mathbf{l}_{10}(E') = \begin{bmatrix} \rho & 0 & 0 \\ -\pi & 0 & 0 \\ -\pi & 0 & 0 \\ -\pi & 0 & 0 \\ -\pi & 0 & 0 \\ -\pi & 0 & 0 \end{bmatrix} \quad \mathbf{l}_{11}(E'^{\dagger}) = \begin{bmatrix} 0 & \rho & 0 \\ 0 & -\pi & 0 \\ 0 & -\pi & 0 \\ 0 & -\pi & 0 \\ 0 & -\pi & 0 \\ 0 & -\pi & 0 \end{bmatrix} \quad \mathbf{l}_{12}(A_2'') = \begin{bmatrix} 0 & 0 & \rho \\ 0 & 0 & -\pi \\ 0 & 0 & -\pi \\ 0 & 0 & -\pi \\ 0 & 0 & -\pi \\ 0 & 0 & -\pi \end{bmatrix}$$

Figure 45. List of 12 normal vibrational modes for AB_5 reference system with D_{3h} symmetry. Below the ball-and-stick representations are the labels and brief descriptions of the normal modes. The irreducible representation and the mode vector for each vibration are also shown.

vibration compared with that from the eighth and ninth normal modes. Figure 18 shows that the phase angle θ_5 drops immediately toward 5° as the reaction starts. This ensures the dominance of the seventh normal mode as its cosine value of 0.996 is very close to 1. Although the phase angle θ_5 starts to increase in the middle of exit channel, its maximum value at the end is around 30° which still claims the dominant role of the seventh normal mode. Given the significant change in r_5 throughout the whole path, we conclude that the reaction path of the Muetterties mechanism **M2** of **2** is dictated by the continuous displacement of the seventh normal vibration of the corresponding reference system.

It seems that our findings are inconsistent with Couzijn's claim[18] that this mechanism consists of two consecutive Berry processes. However, one needs to be aware that their analysis was based on a so-called *topology parameter* that relies on the definition of an equatorial pivot atom in order to describe the Berry process. The well-suited topology parameter describing the entrance (exit) channel of **M2** mechanism is no longer suitable to describe the geometrical changes in the exit (entrance) channel. Couzijn and co-workers thus defined for this reaction two separate topology parameters whose values meet at the TS point.

Despite the simplicity introduced into the Muetterties mechanism **M2**, topology parameters are by nature discontinuous along the complete reaction path. In contrast, our curvilinear coordinate system provides a comprehensive and continuous description of the geometry along reaction path in terms of distortions from a reference geometry.

4.2.3. Muetterties Mechanism M3. Although Couzijn's work[18] suggests the location of an aTS point of the Muetterties mechanism **M3** for **3** via a relaxed PES scan following the Berry process led by the seventh normal vibrational mode as in the last example, the vibration library data (see Appendix A.3) suggest that the eighth normal mode is the most important motion describing this mechanism. One also has to consider that the seventh and eighth vibrations form a doubly degenerate pair. Therefore, we first reordered the atoms in the core fragment of **3** as shown in Figure 19 to ensure that the bending of O2−P1−O6 angle in the $-y$ direction could optimally correspond to the target mechanism. The geometry of the core fragment expressed in curvilinear coordinates is collected in Table 5.

Compared with the AB_5 reference geometry in D_{3h} symmetry, the relative contributions of the seventh, eighth, and ninth normal modes to the geometry of **3** are determined by the phase angles θ_5 and ϕ_5, as this set of pseudotriply degenerate normal modes is controlled by the parameter set $\{r_5, \theta_5, \phi_5\}$. Noteworthy is that the contribution from the seventh vibration ($\cos\theta_5 = 0.87$) to the reactant geometry is still dominating and the eighth vibration ($\sin\theta_5 \sin\phi_5 = -0.48$) is the second dominant vibration. Current phase angles for the eighth vibration correctly specify the desired motion responsible for the reaction mechanism **M3**. The relaxed PES scan was carried out by gradually increasing the amplitude r_5.

As shown in Figure 19, we located a maximum point at r_5 = 1.02 Å followed by a sudden decrease in energy leading to a cusp. However, the subsequent refinement showed that the geometry of this maximum point is already very close to the real TS point for mechanism **M3**, which means the approximate TS point was successfully identified through relaxed PES scan of r_5. On the basis of the refined TS point, a smooth MEP was mapped out as shown in Figure 20. The corresponding variation of the curvilinear coordinates along the MEP is shown in Figures 21 and 22.

The amplitude r_5 shows the most significant change before the TS by increasing from 0.1 to 1.2 Å. In the exit channel, changes of all amplitude values are only marginal, especially after s = 5.0 bohr. As amplitude r_5 is the major driving coordinate in Muetterties mechanism **M3** in the entrance channel, monitoring of the phase angles θ_5 and ϕ_5 is of great importance for the understanding of this mechanism. θ_5 gradually increases from 30° to 60° at the TS and ϕ_5 increases from 255° to 290°; i.e., the eighth normal mode ($\sin\theta_5 \sin\phi_5 = -0.48 \rightarrow -0.81$) takes over the role as the dominant vibration after $s = -12.5$ bohr compared to the seventh normal mode ($\cos\theta_5 = 0.87 \rightarrow 0.50$). The contribution from the ninth vibration remains low ($\sin\theta_5 \cos\phi_5 = -0.13 \rightarrow -0.30$).

Amplitude r_4 shows also a significant change in the entrance channel by increasing from 0.0 to 0.5 Å. The associated phase angle ϕ_4 increases from 68° to 130° at the TS point, indicating the prevailing contribution from the sixth normal mode over the

https://dx.doi.org/10.1021/acs.jctc.9b01274
J. Chem. Theory Comput. 2020, 16, 3162−3193

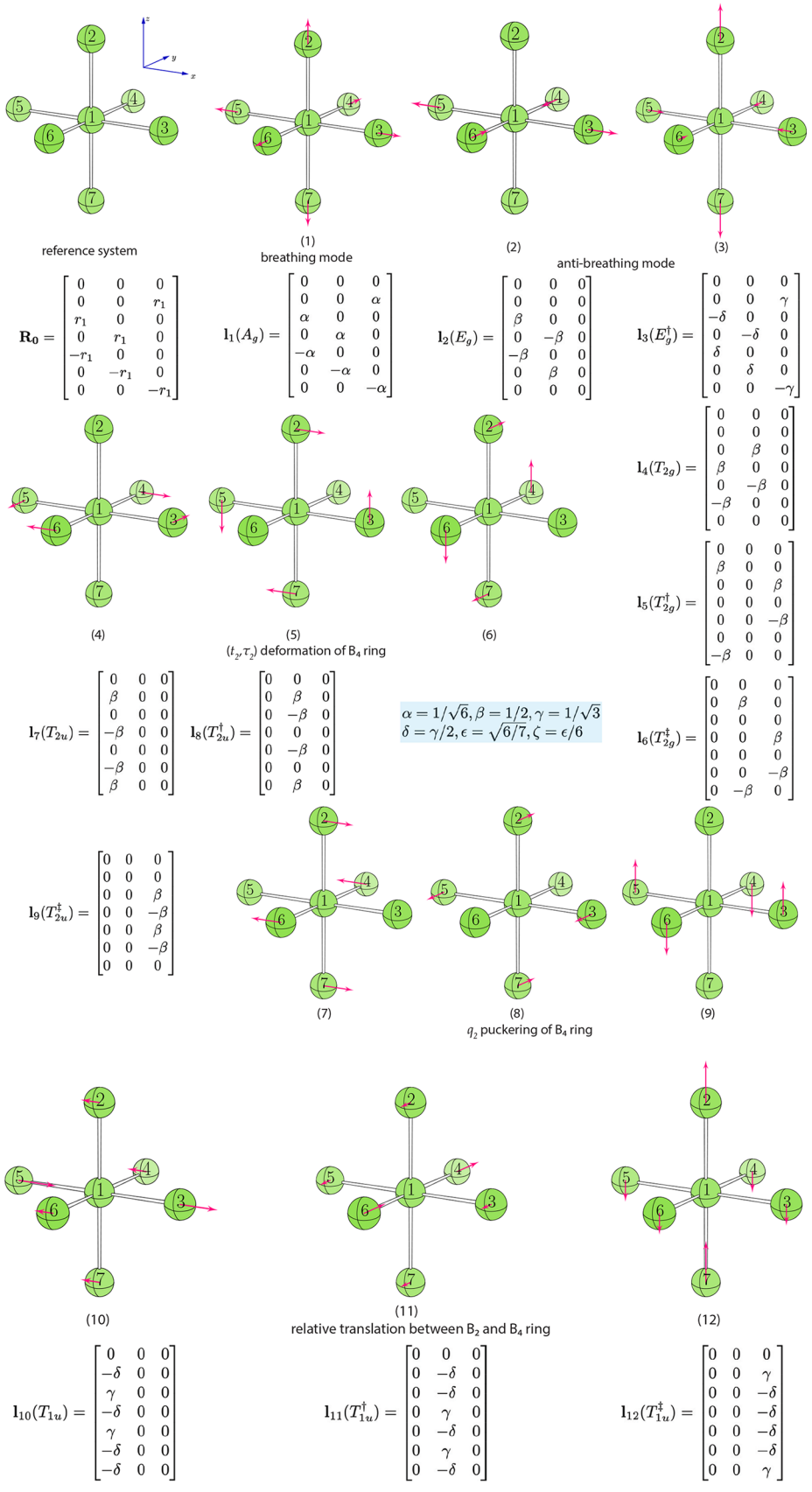

Figure 46. continued

https://dx.doi.org/10.1021/acs.jctc.9b01274
J. Chem. Theory Comput. 2020, 16, 3162−3193

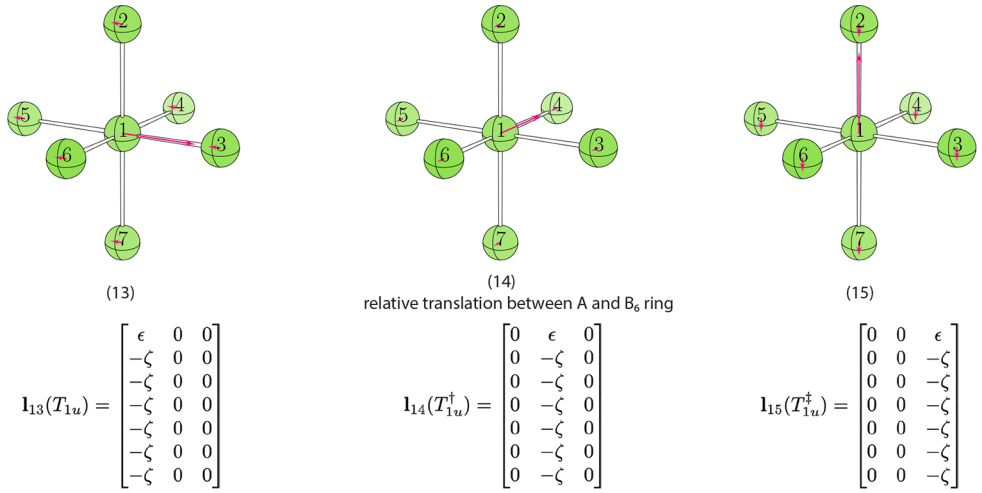

Figure 46. List of 15 normal vibrational modes for AB_6 reference system with O_h symmetry. Below the ball-and-stick representations are the labels and brief descriptions of the normal modes. The irreducible representation and the mode vector for each vibration are also shown.

fifth. While the eighth normal mode brings the O2−P1−O6 angle into the $-y$ direction, the sixth normal mode pulls the O6 atom into the $-y$ direction but the O2 atom is pushed to $+y$ direction. The combined effects of these two modes result in the O6 atom being lifted up in the $-y$ direction while the motions for O2 atom are canceled out, leading to the square pyramidal TS.

The above analysis on mechanism **M3** is based on the present atomic ordering for the core fragment shown in Figure 19. We also could have chosen another more straightforward set of atomic ordering (i.e., pick the yellow C atom as the pivot) in order to utilize Couzijn's conclusion[18] that mechanism **M3** consists of three consecutive Berry processes expecting a dominating contribution from the seventh normal mode throughout the whole path. Important to note is that according to our findings, the initial assignment of reference to real system (i.e., ordering of atoms within the core fragment) is not strictly limited to only one possibility. This allows a certain flexibility, which makes our curvilinear coordinate system robust.

4.3. Bailar and Ray−Dutt Twists of Tris-chelate Metal Complexes. Tris-chelate metal complexes containing three chelating ligands typically adopt an octahedral (hexacoordinate) geometry in the center and they can undergo nondissociative ligand permutation processes (Figure 23), altering their helical chirality (i.e., from Δ to Λ form and vice versa).[29,138] Two well-known mechanisms for racemization of chiral tris-chelates are (1) the Bailar twist,[139] a trigonal twist around the real C_3 axis of a metal tris-chelate and (2) the Ray-Dutt twist,[140] a rhombic twist around a pseudo-C_3 axis. The different pathways describing these two conformational changes originate in the different rotation axes leading to D_{3h} and C_{2v} TSs for the Bailar and the Ray−Dutt twists, respectively. Twists converting an octahedral structure to a trigonal prismatic one at the TS are often associated with spin-state changes of the central metal atom enabled by spin−orbit coupling between different spin states.[141,142] However, in this work, we focus on the aspect of geometrical changes during the twisting motion.

In order to derive the appropriate curvilinear coordinates describing the two twist mechanisms, we first analyzed 15 normal modes for the AB_6 reference system with O_h symmetry (see Figure 47 in Appendix A.4) to search for one vibration that can best describe the twist motion about the C_3 axis in an octahedral geometry. However, we could not identify a single vibration serving for this purpose. The only solution to obtain such a twist vibration turned out to equally mix the seventh, eighth, and ninth vibrations, which are triply degenerate normal modes describing q_2 puckering of four ligating atoms in a plane within the AB_6 reference system. The phase angles of parameter set $\{r_4, \theta_4, \phi_4\}$ describing the twisting motions have the following relationship:

$$|\cos\theta_m| = |\sin\theta_m \sin\phi_m| = |\sin\theta_m \cos\phi_m| \tag{22}$$

There are in total eight sets of solutions to eq 22 in the spherical coordinate system. Four of them are listed in Table 6. The other four solutions are equivalent if the amplitude r_4 is multiplied by −1.

To illustrate how our curvilinear coordinates can be applied to study Bailar and Ray-Dutt twists, we selected a gallium(III) complex coordinated with three malondialdehyde ligands (see Figure 24) as an example, which was taken from a DFT study by Rzepa and Cass.[143] We pick this tris-chelate complex with Ga^{III} as the central atom instead of other transition metals (e.g., Sc^{III} and Ti^{III}) to avoid the complication from possible crossing of the PESs for two different spin states during the twist process.[43] These spin-crossings may be the reason why Rzepa and Cass[143] were unable the locate the TS for Bailar and Ray-Dutt twists of $Co^{III}(mda)_3$ on the singlet PES described with DFT.

The starting geometry of the core fragment of Λ-$Ga^{III}(mda)_3$ expressed in curvilinear coordinates is shown in Table 7.

4.3.1. Bailar Twist. For Λ-$Ga^{III}(mda)_3$, the Bailar twist corresponds to the second solution (i.e., $\theta_4 = 54.7°$, $\phi_4 = 135.0°$) of eq 22; see Table 6. However, the twist direction has to be anticlockwise to initiate this conformational change. From the data in Table 7, we learn that the curvilinear coordinates θ_4 and ϕ_4 of the reactant geometry are identical with those of the second solution; i.e., we can search for the aTS point of the Bailar twist simply via a relaxed PES scan for decreasing amplitude r_4, as shown in Figure 25.

The MEP starting from the refined TS structure shown in Figure 26 shows the conformational changes from Λ-$Ga^{III}(mda)_3$ to Δ-$Ga^{III}(mda)_3$ via a Bailar twist.

Concerning the geometrical changes in terms of curvilinear coordinates for the above Bailar twist process, one interesting observation is that the values of all phase angles (θ_m/ϕ_m) stay constant during the whole reaction path as in the reactant

https://dx.doi.org/10.1021/acs.jctc.9b01274
J. Chem. Theory Comput. 2020, 16, 3162−3193

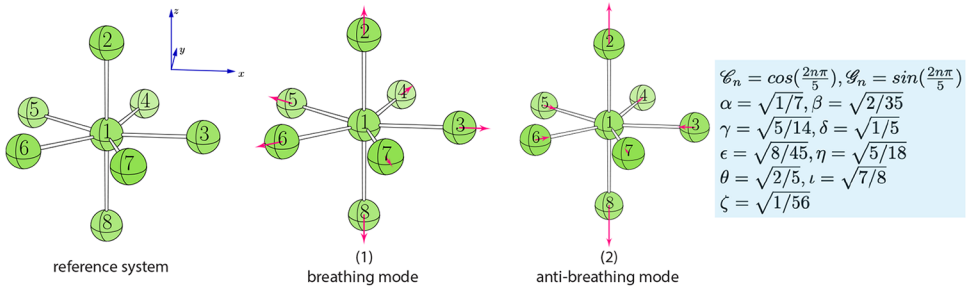

$\mathscr{C}_n = cos(\frac{2n\pi}{5}), \mathscr{G}_n = sin(\frac{2n\pi}{5})$
$\alpha = \sqrt{1/7}, \beta = \sqrt{2/35}$
$\gamma = \sqrt{5/14}, \delta = \sqrt{1/5}$
$\epsilon = \sqrt{8/45}, \eta = \sqrt{5/18}$
$\theta = \sqrt{2/5}, \iota = \sqrt{7/8}$
$\zeta = \sqrt{1/56}$

$$\mathbf{R_0} = \begin{bmatrix} 0 & 0 & 0 \\ 0 & 0 & r_1 \\ r_1 & 0 & 0 \\ \mathscr{C}_1 r_1 & \mathscr{G}_1 r_1 & 0 \\ \mathscr{C}_2 r_1 & \mathscr{G}_2 r_1 & 0 \\ \mathscr{C}_3 r_1 & \mathscr{G}_3 r_1 & 0 \\ \mathscr{C}_4 r_1 & \mathscr{G}_4 r_1 & 0 \\ 0 & 0 & -r_1 \end{bmatrix} \quad \mathbf{l}_1(A_1') = \begin{bmatrix} 0 & 0 & 0 \\ 0 & 0 & \alpha \\ \alpha & 0 & 0 \\ \mathscr{C}_1\alpha & \mathscr{G}_1\alpha & 0 \\ \mathscr{C}_2\alpha & \mathscr{G}_2\alpha & 0 \\ \mathscr{C}_3\alpha & \mathscr{G}_3\alpha & 0 \\ \mathscr{C}_4\alpha & \mathscr{G}_4\alpha & 0 \\ 0 & 0 & -\alpha \end{bmatrix} \quad \mathbf{l}_2(A_1') = \begin{bmatrix} 0 & 0 & 0 \\ 0 & 0 & \gamma \\ -\beta & 0 & 0 \\ -\mathscr{C}_1\beta & -\mathscr{G}_1\beta & 0 \\ -\mathscr{C}_2\beta & -\mathscr{G}_2\beta & 0 \\ -\mathscr{C}_3\beta & -\mathscr{G}_3\beta & 0 \\ -\mathscr{C}_4\beta & -\mathscr{G}_4\beta & 0 \\ 0 & 0 & -\gamma \end{bmatrix}$$

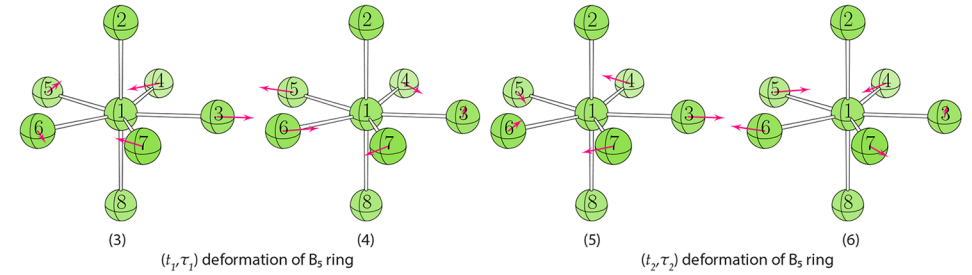

$$\mathbf{l}_3(E_1') = \begin{bmatrix} 0 & 0 & 0 \\ 0 & 0 & 0 \\ \delta & 0 & 0 \\ \mathscr{C}_3\delta & \mathscr{G}_3\delta & 0 \\ \mathscr{C}_1\delta & \mathscr{G}_1\delta & 0 \\ \mathscr{C}_4\delta & \mathscr{G}_4\delta & 0 \\ \mathscr{C}_2\delta & \mathscr{G}_2\delta & 0 \\ 0 & 0 & 0 \end{bmatrix} \quad \mathbf{l}_4(E_1'^{\dagger}) = \begin{bmatrix} 0 & 0 & 0 \\ 0 & 0 & 0 \\ 0 & \delta & 0 \\ \mathscr{G}_2\delta & \mathscr{C}_2\delta & 0 \\ \mathscr{G}_4\delta & \mathscr{C}_4\delta & 0 \\ \mathscr{G}_1\delta & \mathscr{C}_1\delta & 0 \\ \mathscr{G}_3\delta & \mathscr{C}_3\delta & 0 \\ 0 & 0 & 0 \end{bmatrix} \quad \mathbf{l}_5(E_2') = \begin{bmatrix} 0 & 0 & 0 \\ 0 & 0 & 0 \\ \delta & 0 & 0 \\ \mathscr{C}_2\delta & \mathscr{G}_2\delta & 0 \\ \mathscr{C}_4\delta & \mathscr{G}_4\delta & 0 \\ \mathscr{C}_1\delta & \mathscr{G}_1\delta & 0 \\ \mathscr{C}_3\delta & \mathscr{G}_3\delta & 0 \\ 0 & 0 & 0 \end{bmatrix} \quad \mathbf{l}_6(E_2'^{\dagger}) = \begin{bmatrix} 0 & 0 & 0 \\ 0 & 0 & 0 \\ 0 & \delta & 0 \\ \mathscr{G}_3\delta & \mathscr{C}_3\delta & 0 \\ \mathscr{G}_1\delta & \mathscr{C}_1\delta & 0 \\ \mathscr{G}_4\delta & \mathscr{C}_4\delta & 0 \\ \mathscr{G}_2\delta & \mathscr{C}_2\delta & 0 \\ 0 & 0 & 0 \end{bmatrix}$$

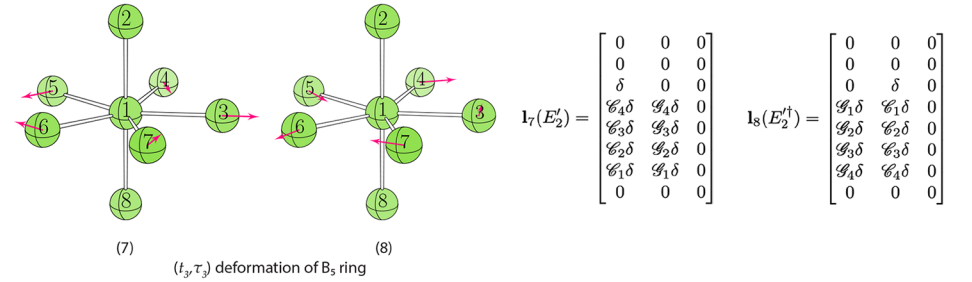

$$\mathbf{l}_7(E_2') = \begin{bmatrix} 0 & 0 & 0 \\ 0 & 0 & 0 \\ \delta & 0 & 0 \\ \mathscr{C}_4\delta & \mathscr{G}_4\delta & 0 \\ \mathscr{C}_3\delta & \mathscr{G}_3\delta & 0 \\ \mathscr{C}_2\delta & \mathscr{G}_2\delta & 0 \\ \mathscr{C}_1\delta & \mathscr{G}_1\delta & 0 \\ 0 & 0 & 0 \end{bmatrix} \quad \mathbf{l}_8(E_2'^{\dagger}) = \begin{bmatrix} 0 & 0 & 0 \\ 0 & 0 & 0 \\ 0 & \delta & 0 \\ \mathscr{G}_1\delta & \mathscr{C}_1\delta & 0 \\ \mathscr{G}_2\delta & \mathscr{C}_2\delta & 0 \\ \mathscr{G}_3\delta & \mathscr{C}_3\delta & 0 \\ \mathscr{G}_4\delta & \mathscr{C}_4\delta & 0 \\ 0 & 0 & 0 \end{bmatrix}$$

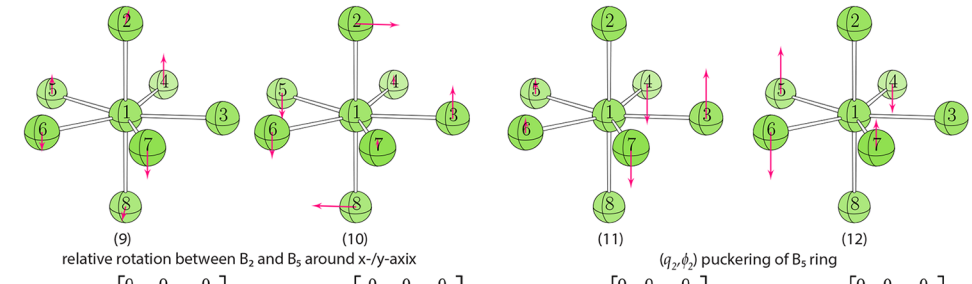

$$\mathbf{l}_9(E_1'') = \begin{bmatrix} 0 & 0 & 0 \\ 0 & \eta & 0 \\ 0 & 0 & 0 \\ 0 & 0 & \mathscr{G}_1\epsilon \\ 0 & 0 & \mathscr{G}_2\epsilon \\ 0 & 0 & \mathscr{G}_3\epsilon \\ 0 & 0 & \mathscr{G}_4\epsilon \\ 0 & -\eta & 0 \end{bmatrix} \quad \mathbf{l}_{10}(E_1''^{\dagger}) = \begin{bmatrix} 0 & 0 & 0 \\ \eta & 0 & 0 \\ 0 & 0 & \epsilon \\ 0 & 0 & \mathscr{C}_1\epsilon \\ 0 & 0 & \mathscr{C}_2\epsilon \\ 0 & 0 & \mathscr{C}_3\epsilon \\ 0 & 0 & \mathscr{C}_4\epsilon \\ -\eta & 0 & 0 \end{bmatrix} \quad \mathbf{l}_{11}(E_2'') = \begin{bmatrix} 0 & 0 & 0 \\ 0 & 0 & 0 \\ 0 & 0 & \theta \\ 0 & 0 & \mathscr{C}_3\theta \\ 0 & 0 & \mathscr{C}_1\theta \\ 0 & 0 & \mathscr{C}_4\theta \\ 0 & 0 & \mathscr{C}_2\theta \\ 0 & 0 & 0 \end{bmatrix} \quad \mathbf{l}_{12}(E_2''^{\dagger}) = \begin{bmatrix} 0 & 0 & 0 \\ 0 & 0 & 0 \\ 0 & 0 & 0 \\ 0 & 0 & \mathscr{G}_3\theta \\ 0 & 0 & \mathscr{G}_1\theta \\ 0 & 0 & \mathscr{G}_4\theta \\ 0 & 0 & \mathscr{G}_2\theta \\ 0 & 0 & 0 \end{bmatrix}$$

Figure 47. continued

https://dx.doi.org/10.1021/acs.jctc.9b01274
J. Chem. Theory Comput. 2020, 16, 3162−3193

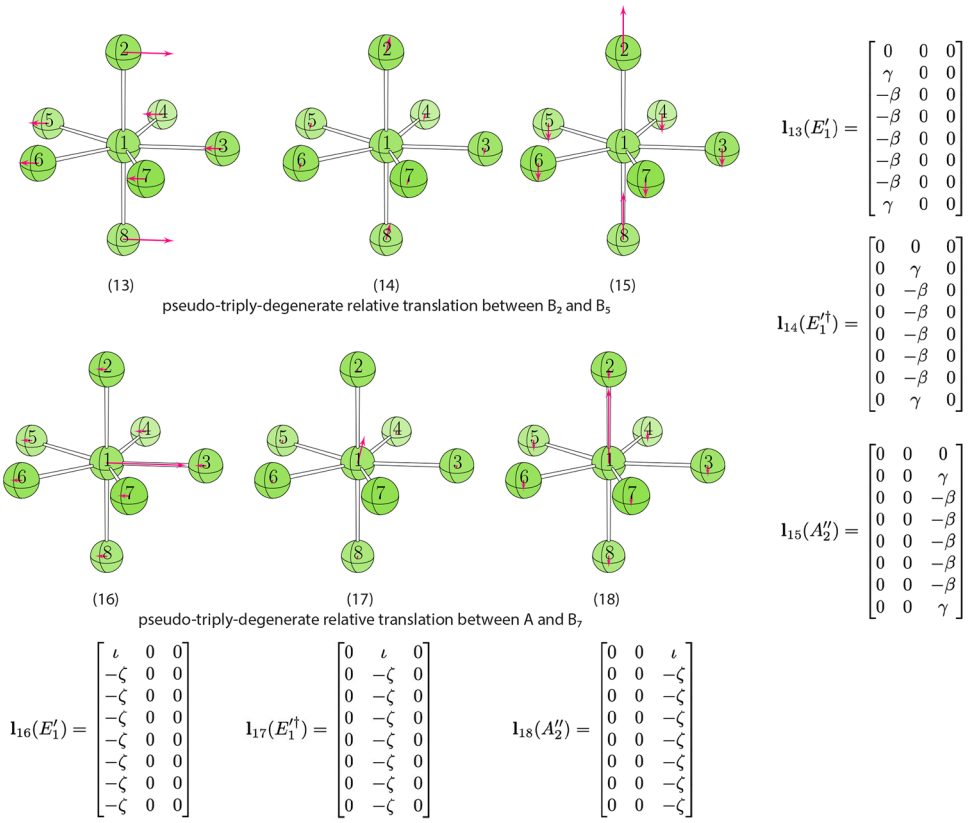

$$\mathbf{l}_{13}(E_1') = \begin{bmatrix} 0 & 0 & 0 \\ \gamma & 0 & 0 \\ -\beta & 0 & 0 \\ -\beta & 0 & 0 \\ -\beta & 0 & 0 \\ -\beta & 0 & 0 \\ -\beta & 0 & 0 \\ \gamma & 0 & 0 \end{bmatrix}$$

$$\mathbf{l}_{14}(E_1'^{\dagger}) = \begin{bmatrix} 0 & 0 & 0 \\ 0 & \gamma & 0 \\ 0 & -\beta & 0 \\ 0 & -\beta & 0 \\ 0 & -\beta & 0 \\ 0 & -\beta & 0 \\ 0 & -\beta & 0 \\ 0 & \gamma & 0 \end{bmatrix}$$

$$\mathbf{l}_{15}(A_2'') = \begin{bmatrix} 0 & 0 & 0 \\ 0 & 0 & \gamma \\ 0 & 0 & -\beta \\ 0 & 0 & -\beta \\ 0 & 0 & -\beta \\ 0 & 0 & -\beta \\ 0 & 0 & -\beta \\ 0 & 0 & \gamma \end{bmatrix}$$

$$\mathbf{l}_{16}(E_1') = \begin{bmatrix} \iota & 0 & 0 \\ -\zeta & 0 & 0 \\ -\zeta & 0 & 0 \\ -\zeta & 0 & 0 \\ -\zeta & 0 & 0 \\ -\zeta & 0 & 0 \\ -\zeta & 0 & 0 \\ -\zeta & 0 & 0 \end{bmatrix}$$

$$\mathbf{l}_{17}(E_1'^{\dagger}) = \begin{bmatrix} 0 & \iota & 0 \\ 0 & -\zeta & 0 \\ 0 & -\zeta & 0 \\ 0 & -\zeta & 0 \\ 0 & -\zeta & 0 \\ 0 & -\zeta & 0 \\ 0 & -\zeta & 0 \\ 0 & -\zeta & 0 \end{bmatrix}$$

$$\mathbf{l}_{18}(A_2'') = \begin{bmatrix} 0 & 0 & \iota \\ 0 & 0 & -\zeta \\ 0 & 0 & -\zeta \\ 0 & 0 & -\zeta \\ 0 & 0 & -\zeta \\ 0 & 0 & -\zeta \\ 0 & 0 & -\zeta \\ 0 & 0 & -\zeta \end{bmatrix}$$

Figure 47. List of 18 normal vibrational modes for AB_7 reference system with D_{5h} symmetry. Below the ball-and-stick representations are the labels and brief descriptions of the normal modes. The irreducible representation and the mode vector for each vibration are also shown.

geometry. Figure 27 shows that among six amplitude r_m values, three of them stay as zero and the amplitude r_4 has the most significant change from 0.0 to −1.4 Å. We find that the values of the parameter set $\{r_3, \theta_3, \phi_3\}$ shown in Table 7 specify also an equal mixing of three degenerate normal vibrations (i.e., the fourth, fifth and sixth) of the octahedral AB_6 reference system. The joint effect of such combination leads to the synchronized change in the bite angles of three chelating ligands as revealed by the change in amplitude r_3 from 0.0 to 0.5 Å.

4.3.2. Ray-Dutt Twist. The Ray−Dutt twist in Λ-$Ga^{III}(mda)_3$ has three possible pathways as it has three pseudo-C_3 axes, which correspond to the first, third, and fourth solutions of eq 22 listed in Table 6. We selected the Ray−Dutt twist motion associated with the fourth solution to illustrate the use of curvilinear coordinates because ϕ_4 in the geometry of Λ-$Ga^{III}(mda)_3$ is the same as in the fourth solution, which simplifies the analysis. However, due to the D_3 symmetry in $Ga^{III}(mda)_3$, the choice from these three equivalent twists is in reality trivial.

When searching for the TS structure of the Ray−Dutt twist through a relaxed PES scan, we took a different route. Unlike for the other examples where the relaxed PES scans were carried out without any further constraint besides the driving coordinate variable, in this case we imposed one additional constraint, namely, θ_4 = 125.3° to properly orient the coordinate driving into the direction of Ray-Dutt twist. The change of θ_4 from 54.7° to 125.3° results in a marginal geometrical change for Λ-$Ga^{III}(mda)_3$ accompanied by an energy increase of less than 0.1 kcal/mol. By decreasing the amplitude r_4 stepwise, we successfully located the aTS point of the desired Ray-Dutt twist motion (see Figure 28).

After the refinement of the aTS geometry resulting in the TS, we mapped out the MEP of the Ray-Dutt twist, as shown in Figure 29.

Figure 30 shows that the amplitudes r_m behave in a similar way during Ray-Dutt twist as for the Bailar twist shown in Figure 27. This demonstrates the mechanistic similarity between Bailar and Ray-Dutt twists with regard to the motion of the core fragment.

Unlike the Bailar twist where four phase angles remain constant along the reaction path, only ϕ_4 is unchanged during Ray-Dutt twist. As shown in Figure 31, θ_3 drops to 54.7° and ϕ_3 increases to 225°. A discontinuity is found for θ_4 at s = −8.5 bohr as the amplitude r_4 equals zero at that point leading to no definition for θ_4 and ϕ_4 according to eq 16. However, this does not necessarily mean that the curvilinear coordinate system fails to describe a continuous conformational change along the reaction path, because the changes in amplitudes are still continuous.

4.4. Bartell Mechanism of Iodine Heptafluoride (IF_7).

The IF_7 molecule is one of the most investigated prototypes of a heptacoordinated molecule,[144] and its fluxionality was first reported by Bartell and co-workers in the 1970s.[20,145,146] With its pentagonal bipyramidal molecular geometry in D_{5h} symmetry, the equatorial fluorine atoms can undergo a dynamic puckering motion inducing an axial bending leading to a pseudorotation path via a C_{2v} transition state. This polytopal rearrangement process was coined the *Bartell mechanism* for the first time by Minyaev and co-workers in 1994.[147] The transition path for the Bartell mechanism was modeled with quantum chemical calculations by Rzepa and co-workers in 2006.[15] Noteworthy is that Christe and co-workers proposed another much slower axial−equatorial ligand exchange mechanism for

https://dx.doi.org/10.1021/acs.jctc.9b01274
J. Chem. Theory Comput. 2020, 16, 3162−3193

IF_7 based on NMR evidence in 1993.[14] However, this process seemed to be too complicated and was never confirmed afterward.

In this work, we focused on the Bartell mechanism being described with our curvilinear coordinates. The optimized geometry of IF_7 molecule is described in Table 8, where three phase anlges ϕ_m associated with $r_m = 0$ was intentionally set to 180°.

As described in Bartell's original work, this pseudorotation path is dominated by E_2'' puckering.[20] Analyzing the vibration library data of the reference system (see Appendix A.5) we found that the parameter set $\{r_7, \phi_7\}$ corresponds to doubly degenerate (q_2, ϕ_2) ring puckering vibrations. By carrying out a relaxed PES scan with the increasing amplitude r_7, we successfully located the aTS point for the Bartell mechanism, as shown in Figure 32.

After refinement of the TS point, the complete MEP was mapped out, as shown in Figure 33 revealing the Bartell mechanism. The changes in amplitudes r_m and phase angles θ_m/ϕ_m of IF_7 along the MEP are shown in Figures 34 and 35.

Along the MEP, amplitudes r_2 through r_8 are increased to different extent. The amplitude r_9 adopts the zero value throughout the whole path and its associated phase angles are thus not shown. Similar to several other dynamic fluxional processes discussed above, the phase angles also adopt constant values along the whole reaction path. Amplitude r_7 has the largest increase from 0.0 to 0.7 Å, followed by the amplitude r_8 from 0.0 to 0.6 Å. Phase angle ϕ_7 takes the value of 162°, indicating a dominant contribution from the 11th normal mode ($\cos \phi_7 = -0.95$) compared with the 12th normal mode ($\sin \phi_7 = 0.31$). For the parameter set $\{r_8, \theta_8, \phi_8\}$, θ_8 is 145° and ϕ_8 equals 90°, which specifies the mixing of the 13th and 14th vibrational modes without any contribution from the 15th normal mode, leading to an axial bending motion. In summary, the conformational changes described in terms of curvilinear coordinates are consistent with Bartell's original description of distortion from D_{5h} symmetry for IF_7.[20]

4.5. Two Technically Complicated Fluxional Mechanisms. In the above examples illustrating the usefulness of our newly developed curvilinear coordinate system for the description of dynamic fluxional processes, we have demonstrated that the search of the aTS point for the polytopal rearrangement processes can be done in a systematic way via a relaxed PES scan starting from equilibrium geometry using a single amplitude r_m from the complete set of curvilinear coordinates as a variable.

In the following, we discuss two examples for which the single-parameter PES scan protocol fails to locate the aTS point and we present a solution for successfully finding the aTS point in these cases. Rather than undermining the value of the curvilinear coordinates developed in this work, these two examples reflect robustness and flexibility of our approach.

4.5.1. Chimeric Pseudorotation of Iodine Pentafluoride (IF_5). Similar to IF_7, the iodine pentafluoride (IF_5) is also a hypervalent halogen compound. Its square pyramidal (C_{4v}) geometry was first reported by Lord and co-workers in 1950.[148] Several years later in 1957, Muetterties and Phillips carried out ^{19}F NMR studies on IF_5, and they observed IF_5 being stable at room temperature. However, the absence of F−F coupling pattern in NMR spectra at elevated temperatures indicated apical-basal fluorine exchange.[121] Therefore, they concluded that such apical-basal exchange has a relatively high energy barrier over 25 kcal/mol and they hypothesized that this process would proceed via a dimer structure. During the following years, little progress was made with regard to a more detailed understanding of the fluxional mechanism of IF_5 until in 2006 when Rzepa and Cass suggested a nondissociative (i.e., intramolecular) mechanism based on quantum chemical calculations.[25] Their reaction path analysis led to the conclusion that the fluxional mechanism of IF_5 is composed of three distinct fluxional processes mixed together, which they coined *chimeric pseudorotation*. Noteworthy is that the BrF_5 can undergo the same chimeric pseudorotation as IF_5 via a C_s TS according to Rzepa's calculations, while the ClF_5 adopts a different path via a C_{2v} TS resembling a Berry pseudorotation, which was exemplified by PF_5, SF_4, and $Fe(CO)_5$, as discussed above. In this work, we studied the chimeric pseudorotation of IF_5 with curvilinear coordinates to further explore Rzepa's findings. Equilibrium geometry data of IF_5 are collected in Table 9.

In order to locate the aTS point for the chimeric pseudorotation mechanism, we performed a relaxed PES scan of a single amplitude parameter using r_3 through r_7, one at a time combined with various phase angle possibilities, but failed to capture the desired aTS point. After closer inspection of the IF_5 equilibrium geometry compared with the TS geometry calculated by Rzepa,[25] we found that the geometrical change from reactant toward TS can be attributed to a q_2 puckering motion of four basal fluorines combined with a (t_1, τ_1) deformation of the same four-membered ring. According to the vibration library for the AB_5 reference system in C_{4v} symmetry (see Figure 3), the displacement of q_2 puckering and (t_1, τ_1) deformation for the B_4 ring is controlled by r_3 and $\{r_4, \phi_4\}$, respectively. Therefore, we performed next a 2D relaxed PES scan of r_3 and r_4, as shown in Figure 36, and the aTS point could be correctly identified.

After the refinement of the TS point, the complete MEP of the chimeric pseudorotation for IF_5 was mapped out as shown in Figure 37.

The change in the amplitude values along the MEP shown in Figure 38 is rather simple as r_3 through r_6 all increase from 0.0 Å in the very beginning. Noteworthy is that r_3 and r_4 stay close to each other and progress in a synchronized fashion. The phase angle change in Figure 39 shows ϕ_4 gradually increases from 60.0° to 85.0°, indicating more contribution from the fifth normal mode than the fourth.

For this showcase example, one might suggest combining the third normal mode from the vibrational library with the fourth and fifth modes forming a pseudotriply degenerate curvilinear coordinate parameter set, as these three vibrational modes are highly similar and in this way allowing to locate the aTS point via a single-parameter (i.e., amplitude) relaxed PES scan, which is simpler than 2D scan. It is feasible to implement the curvilinear coordinates in that way. However, the grouping of the vibrations with different symmetries into either pairs or triads is not arbitrary. We rather prefer to group vibrations depending on their types of motion. The third vibration is the puckering motion of the four-membered ring of the basal F atoms, while the fourth and fifth vibrations are related to ring deformation. Separating these two well-defined motions is physically more meaningful.

4.5.2. Lever Mechanism of Sulfur Tetrafluoride (SF_4). In addition to the Berry pseudorotation of SF_4 discussed in section 4.1, other mechanisms were proposed to enable complete scrambling of its four fluorine atoms.[149] The most credible alternative to Berry pseudorotation, termed *lever mechanism*, was first proposed by Minyaev and co-workers[147] and further

https://dx.doi.org/10.1021/acs.jctc.9b01274
J. Chem. Theory Comput. 2020, 16, 3162−3193

investigated by Mauksch and Schleyer with theoretical calculations.[17]

We failed to locate the aTS point pertaining to the lever mechanism in SF_4 with curvilinear coordinates via a relaxed PES scan of either one single amplitude or two amplitudes, as we did for IF_5. The correct aTS point was successfully disclosed by a relaxed PES scan of the two phase angles of the parameter set $\{r_4, \theta_4, \phi_4\}$, which corresponds to relative translations of the central atom.

As shown in the right half of the energy contour plot in Figure 40, there are three reaction valleys interconnected with each other by three first-order saddle points. The green round dot in the upper reaction valley corresponds to the reactant geometry for SF_4 described in Table 2. In the middle of three first-order saddle points, there is a second-order saddle point corresponding to a C_{3v} geometry[17] with slightly higher energy (~1.0 kcal/mol). The left region of this contour map seems to be centrally symmetric to the right part.

Our results are consistent with the qualitative energy landscape of Mauksch and Schleyer, which led them to the conclusion that three MEPs of lever mechanism encircle the second-order saddle point.[17] They named such an energy surface where three valleys meet on a hilltop having two imaginary frequencies[150,151] as "effective monkey saddle point", which has to be distinguished from an ideal "monkey saddle" where doubly degenerate zero curvatures are required.[152,153] In this sense, we have now consolidated the work of Mauksch and Schleyer[17] for the first time by presenting a detailed description of the unusual PES of the SF_4 lever mechanism with the help of our new curvilinear coordinates.

On the basis of a refined TS point, the MEP marked out in the above 2D PES contour plot was mapped out in Figure 41.

The conformational change of SF_4 expressed in curvilinear coordinates during the lever pseudorotation is shown in Figures 42 and 43.

The amplitude values along the MEP are symmetric with regard to $s = 0$ bohr. Amplitude r_4 has the least change although its associated phase angles θ_4 and ϕ_4 play a central role in driving the reaction coordinates.

Among all phase angles, θ_4 and ϕ_4 show a moderate change along the reaction path. Throughout the whole path these two phase angles change from 90° and 360° toward 135° and 270°, respectively, specifying the full contribution from the ninth normal vibration ($\sin\theta\cos\phi = 1$) for the reactant geometry and equal contributions from the seventh and eighth normal modes ($\cos\theta = \sin\theta\sin\phi = -\sqrt{2}/2$) for the product geometry. This means that the reactant geometry is basically a result of the upward translation of the central sulfur atom in the $+z$ direction. With the progress of lever mechanism the contribution of this upward translation decays (i.e., central sulfur moves downward) and the sulfur atom gradually moves into the $-x$ and $-y$ direction.

A similar variation is also found for θ_3 and ϕ_3. On the basis of this observation, we performed a relaxed PES scan of these two phase angles in order to locate the aTS point. However, it turned out that the only solution leading to the correct aTS point is via relaxed scanning of θ_4 and ϕ_4.

5. CONCLUSIONS

We developed in this work a novel curvilinear coordinate system describing polytopal rearrangements in N-coordinate compounds, where N can take any number from four through seven:

(1) The physical foundation of this curvilinear coordinate system is based on the fact that a chemical reaction can be initiated and even accelerated via the excitation of vibrational modes of the reaction complex.[68−70,74,75] The polytopal rearrangements in N-coordinate molecules, like conformational changes, can be considered as unimolecular reactions, which are amenable to the promotion by certain vibrations. In this sense, the new curvilinear coordinate system is a conceptual extension of the Cremer−Pople ring puckering coordinates[47] as well as the recently proposed ring deformation coordinates.[54]

(2) The curvilinear coordinates developed in this work are derived from the normal vibrational modes of N-coordinate reference systems AB_n, for which $3M - 6$ curvilinear coordinates (where $M = N + 1$) are sufficient to describe the geometry of any N-coordinate motif.

(3) A reference system AB_n defines a geometrical template (i.e., its size is scalable) with a highly symmetric N-coordinate structure that fulfill several preconditions. In this work, we have stipulated reference systems for different N-coordinate structures ranging from tetracoordinate to heptacoordinate in different point groups including AB_4 in T_d symmetry, AB_5 in D_{3h} and C_{4v} symmetries, AB_6 in O_h and C_{5v} symmetries along with AB_7 in D_{5h} and C_{6v} symmetries. These reference systems cover the vast majority of single-center coordination compounds (versus binuclear and polynuclear complexes).

(4) In a coordination compound, the geometry of its N-coordinate core fragment ("real system") can be unambiguously expressed by the nonredundant set of $3M - 6$ normal vibrations of corresponding reference system AB_n if the internal coordinate space of the real system matches exactly the internal vibration space of the reference system. This is realized by translating and rotating the real system into a standard orientation, from which the geometrical information is encoded by the projection of Cartesian coordinates onto the $3M - 6$ normal vibrations of the reference system. Depending on the degeneracy and type of motion of the $3M - 6$ normal vibrational modes, some of the $3M - 6$ projections are grouped into pairs or triads, leading to three kinds of curvilinear coordinate parameter sets: (i) nondegenerate $\{r_m\}$, (ii) doubly degenerate $\{r_m, \phi_m\}$, and (iii) triply degenerate $\{r_m, \theta_m, \phi_m\}$. The latter two parameter sets with phase angles (θ_m/ϕ_m) linearly combine two and three vibrations, respectively.

(5) Any complete set of internal or Cartesian coordinates of an N-coordinate structure can be transformed into $3M - 6$ curvilinear coordinates. In turn, the curvilinear coordinates can be used to derive the internal or Cartesian coordinates of the N-coordinate structure.

(6) The new curvilinear coordinates are well-suited reaction coordinates for describing polytopal rearrangements in two aspects. First, these curvilinear coordinates can directly be used for 1D/2D relaxed PES scan starting from an equilibrium geometry to locate the first-order saddle point (TS). In most cases, the equilibrium geometry of the reactant is close to that of the corresponding reference system with many amplitude parameters r_m being almost zero (except r_1). A relaxed PES scan in which one or two amplitudes r_m are steadily increased simulates the process of the vibration(s) (associated with the scanned amplitudes) being excited to obtain pronounced atomic displacements. Noteworthy is that, like using internal coordinates for relaxed PES scans, the choice of curvilinear coordinations as the constraint variables requires them to be closely related to the vibrations initiating a polytopal rearrangement process. Even in the rare case that the molecular geometry

https://dx.doi.org/10.1021/acs.jctc.9b01274
J. Chem. Theory Comput. 2020, 16, 3162−3193

is different from its best suited reference system in terms of symmetry (e.g., SF_4 with C_{2v} symmetry versus its reference system with T_d symmtry), a relaxed PES scan with our curvilinear coordinate system can reveal important mechanistic details. Second, the polytopal rearrangement pathways (especially in the entrance channel before TS) can be better understood in terms of one or two leading vibrational motions. Such a simplification has been widely used in understanding the conformational change of proteins.[154]

(7) Nine different polytopal rearrangement processes in tetracoordinate through heptacoordinate compounds were studied, including the Berry pseudorotation and the lever mechanism for SF_4, the chimeric pseudorotation for IF_5, the Berry pseudorotation and the Muetterties' mechanisms for trigonal bipyramidal structures, Bailar and Ray-Dutt twists for tris-chelates, and the Bartell mechanism for IF_7. These showcase examples endorse the general applicability of our curvilinear coordinates for the description of polytopal rearrangements for different coordination structures.

Noteworthy is that in the case of several polytopal rearrangement mechanisms studied in this work, the phase angles (θ_m/ϕ_m) are unchanged along the whole pathway, including the Berry pseudorotations for SF_4 and $Fe(CO)_5$, the Bailar twist for tris-chelates and the Bartell mechanism for IF_7. This finding is closely related to the observation of Avnir, Alvarez, and co-workers that the Berry pseudorotation in pentacoordinate compounds and the Bailar twist possess minimal distortion pathways according to their CShM analysis.[23]

On the basis of the curvilinear coordinate framework introduced in this work, work in progress covers the following directions:

- The curvilinear coordinates will be employed to explore all possible polytopal rearrangement mechanisms for newly discovered and intriguing coordination structures.
- Unconfirmed polytopal mechanisms reported in the literature will be revisited, like the chimeric pseudorotation for IF_5 rediscovered and studied by Rzepa and Cass.[25]
- More reference systems and associated curvilinear coordinates are to be designed for heptacoordinate and octacoordinate compounds, which are less explored compared with lower coordinated counterparts in the hope of discovering novel polytopal rearrangement mechanisms.
- The curvilinear coordinate system can be incorporated into automatic workflows for high-throughput screening for polypotal rearrangements as well as rational design of transition-metal complexes. Related work in this direction has been pioneered by the Kulik group.[155−158]
- Collective variables based on the curvilinear coordinates developed in this work will be implemented in order to sample free energy surfaces of polytopal rearrangements with molecular dynamics simulations.[159]

In conclusion, this work introduces a dedicated curvilinear coordinate system for the description of polytopal rearrangements in coordination compounds opening a new avenue for the systematic study and comparison of these fluxional processes.

APPENDIX A

A.1. Formula for Wilson B- and dB-Matrix

We have derived the formulas to calculate the Wilson **B**-matrix and its derivative for the curvilinear coordinate system developed in this work using finite difference method.

(i) Nondegenerate curvilinear coordinate $\{r_m\}$

$$\frac{\partial r_m}{\partial x_i} = \mathcal{F}\frac{\Delta d_m}{\Delta x_i} \tag{23}$$

$$\frac{\partial^2 r_m}{\partial x_i \partial x_j} = \mathcal{F}\frac{\Delta^2 d_m}{\Delta x_i \Delta x_j} \tag{24}$$

(ii) Doubly degenerate curvilinear coordinates $\{r_m, \phi_m\}$

$$\frac{\partial r_m}{\partial x_i} = \mathcal{F}\left(\cos\phi_m \frac{\Delta d_m}{\Delta x_i} + \sin\phi_m \frac{\Delta d'_m}{\Delta x_i}\right) \tag{25}$$

$$\frac{\partial \phi_m}{\partial x_i} = \frac{\mathcal{F}}{r_m}\left(-\sin\phi_m \frac{\Delta d_m}{\Delta x_i} + \cos\phi_m \frac{\Delta d'_m}{\Delta x_i}\right) \tag{26}$$

$$\frac{\partial^2 r_m}{\partial x_i \partial x_j} = \mathcal{F}\left(\cos\phi_m \frac{\Delta^2 d_m}{\Delta x_i \Delta x_j} + \sin\phi_m \frac{\Delta^2 d'_m}{\Delta x_i \Delta x_j}\right) + r_m \frac{\Delta\phi_m}{\Delta x_i}\frac{\Delta\phi_m}{\Delta x_j} \tag{27}$$

$$\frac{\partial^2 \phi_m}{\partial x_i \partial x_j} = \frac{\mathcal{F}}{r_m}\left(-\sin\phi_m \frac{\Delta^2 d_m}{\Delta x_i \Delta x_j} + \cos\phi_m \frac{\Delta^2 d'_m}{\Delta x_i \Delta x_j}\right) - \frac{1}{r_m}\left(\frac{\Delta r_m}{\Delta x_i}\frac{\Delta\phi_m}{\Delta x_j} + \frac{\Delta r_m}{\Delta x_j}\frac{\Delta\phi_m}{\Delta x_i}\right) \tag{28}$$

(iii) Triply degenerate curvilinear coordinates $\{r_m, \theta_m, \phi_m\}$

$$\frac{\partial r_m}{\partial x_i} = \mathcal{F}\left(\cos\theta_m \frac{\Delta d_m}{\Delta x_i} + \sin\theta_m \sin\phi_m \frac{\Delta d'_m}{\Delta x_i} + \sin\theta_m \cos\phi_m \frac{\Delta d''_m}{\Delta x_i}\right) \tag{29}$$

$$\frac{\partial \theta_m}{\partial x_i} = \frac{\mathcal{F}}{r_m}\left(-\sin\theta_m \frac{\Delta d_m}{\Delta x_i} + \cos\theta_m \sin\phi_m \frac{\Delta d'_m}{\Delta x_i} + \cos\theta_m \cos\phi_m \frac{\Delta d''_m}{\Delta x_i}\right) \tag{30}$$

$$\frac{\partial \phi_m}{\partial x_i} = \frac{\mathcal{F}}{r_m \sin\theta_m}\left(\cos\phi_m \frac{\Delta d'_m}{\Delta x_i} - \sin\phi_m \frac{\Delta d''_m}{\Delta x_i}\right) \tag{31}$$

$$\frac{\partial^2 r_m}{\partial x_i \partial x_j} = \mathcal{F}\left(\cos\theta_m \frac{\Delta^2 d_m}{\Delta x_i \Delta x_j} + \sin\theta_m \sin\phi_m \frac{\Delta^2 d'_m}{\Delta x_i \Delta x_j} + \sin\theta_m \cos\phi_m \frac{\Delta^2 d''_m}{\Delta x_i \Delta x_j}\right) + r_m \frac{\Delta\theta_m}{\Delta x_i}\frac{\Delta\theta_m}{\Delta x_j} + r_m \sin^2\theta_m \frac{\Delta\phi_m}{\Delta x_i}\frac{\Delta\phi_m}{\Delta x_j} \tag{32}$$

https://dx.doi.org/10.1021/acs.jctc.9b01274
J. Chem. Theory Comput. 2020, 16, 3162−3193

$$\frac{\partial^2\theta_m}{\partial x_i \partial x_j} = \frac{\mathcal{F}}{r_m}\left(-\sin\theta_m \frac{\Delta^2 d_m}{\Delta x_i \Delta x_j} + \cos\theta_m \sin\phi_m \frac{\Delta^2 d'_m}{\Delta x_i \Delta x_j} + \cos\theta_m \cos\phi_m \frac{\Delta^2 d''_m}{\Delta x_i \Delta x_j}\right) - \frac{1}{r_m}\left(\frac{\Delta r_m}{\Delta x_i}\frac{\Delta\theta_m}{\Delta x_j} + \frac{\Delta r_m}{\Delta x_j}\frac{\Delta\theta_m}{\Delta x_i}\right) + \sin\theta_m \cos\theta_m \frac{\Delta\phi_m}{\Delta x_i}\frac{\Delta\phi_m}{\Delta x_j} \quad (33)$$

$$\frac{\partial^2\phi_m}{\partial x_i \partial x_j} = \frac{\mathcal{F}}{r_m \sin\theta_m}\left(\cos\phi_m \frac{\Delta^2 d'_m}{\Delta x_i \Delta x_j} - \sin\phi_m \frac{\Delta^2 d''_m}{\Delta x_i \Delta x_j}\right) - \frac{1}{r_m}\left(\frac{\Delta r_m}{\Delta x_i}\frac{\Delta\phi_m}{\Delta x_j} + \frac{\Delta r_m}{\Delta x_j}\frac{\Delta\phi_m}{\Delta x_i}\right) - \frac{1}{\tan\theta_m}\left(\frac{\Delta\theta_m}{\Delta x_i}\frac{\Delta\phi_m}{\Delta x_j} + \frac{\Delta\theta_m}{\Delta x_j}\frac{\Delta\phi_m}{\Delta x_i}\right) \quad (34)$$

Table 10. Summary of 9 Curvilinear Coordinate Parameters in 4 Sets Based on 9 Normal Vibrational Modes for the Reference System AB_4 in T_d Symmetry

normal mode	curvilinear coordinates	symmetry	description
1	r_1	A_1	AB_4 breathing
2, 3	r_2, ϕ_2	E	doubly degenerate vibrations
4, 5, 6	r_3, θ_3, ϕ_3	T_2	triply degenerate vibrations
7, 8, 9	r_4, θ_4, ϕ_4	T_2	translation of A

Table 11. Summary of 12 Curvilinear Coordinate Parameters in 6 Sets Based on 12 Normal Vibrational Modes for the Reference System AB_5 in D_{3h} Symmetry

normal mode	curvilinear coordinates	symmetry	description
1	r_1	A_1'	AB_5 breathing
2	r_2	A_1'	antibreathing
3, 4	r_3, ϕ_3	E′	(t_1, τ_1) deformation of B_3 ring
5, 6	r_4, ϕ_4	E″	relative rotation within B_5
7, 8, 9	r_5, θ_5, ϕ_5	E′ + A_2''	relative translation within B_5
10, 11, 12	r_6, θ_6, ϕ_6	E′ + A_2''	translation of A

Table 12. Summary of 15 Curvilinear Coordinate Parameters in 6 Sets Based on 15 Normal Vibrational Modes for the Reference System AB_6 in O_h Symmetry

normal mode	curvilinear coordinates	symmetry	description
1	r_1	A_g	AB_6 breathing
2, 3	r_2, ϕ_2	E_g	antibreathing
4, 5, 6	r_3, θ_3, ϕ_3	T_{2g}	(t_2, τ_2) deformation of B_4 ring
7, 8, 9	r_4, θ_4, ϕ_4	T_{2u}	q_2 puckering of B_4 ring
10, 11, 12	r_5, θ_5, ϕ_5	T_{1u}	relative translation within B_6
13, 14, 15	r_6, θ_6, ϕ_6	T_{1u}	translation of A

Table 13. Summary of 18 Curvilinear Coordinate Parameters in 9 Sets Based on 18 Normal Vibrational Modes for the Reference System AB_7 in D_{5h} Symmetry

normal mode	curvilinear coordinates	symmetry	description
1	r_1	A_1'	AB_7 breathing
2	r_2	A_1'	antibreathing
3, 4	r_3, ϕ_3	E_1'	(t_1, τ_1) deformation of B_5 ring
5, 6	r_4, ϕ_4	E_2'	(t_2, τ_2) deformation of B_5 ring
7, 8	r_5, ϕ_5	E_2'	(t_3, τ_3) deformation of B_5 ring
9, 10	r_6, ϕ_6	E_1''	relative rotation within B_7
11, 12	r_7, ϕ_7	E_2''	(q_2, ϕ_2) puckering of B_5 ring
13, 14, 15	r_8, θ_8, ϕ_8	E_1' + A_2''	relative translation within B_7
16, 17, 18	r_9, θ_9, ϕ_9	E_1' + A_2''	translation of A

A.2. T_d Reference System and Its Vibrations

The geometry and the vibration library for AB_4 reference system in T_d symmetry are shown in Figure 44. The definition of curvilinear coordinate parameters associated with this reference system is collected in Table 10.

A.3. D_{3h} Reference System and Its Vibrations

The geometry and the vibration library for AB_5 reference system in D_{3h} symmetry are shown in Figure 45. The definition of curvilinear coordinate parameters associated with this reference system is collected in Table 11.

A.4. O_h Reference System and Its Vibrations

The geometry and the vibration library for AB_6 reference system in O_h symmetry are shown in Figure 46. The definition of curvilinear coordinate parameters associated with this reference system is collected in Table 12.

A.5. D_{5h} Reference System and Its Vibrations

The geometry and the vibration library for AB_7 reference system in D_{5h} symmetry are shown in Figure 47. The definition of curvilinear coordinate parameters associated with this reference system is collected in Table 13.

■ ASSOCIATED CONTENT

Supporting Information

The Supporting Information is available free of charge at https://pubs.acs.org/doi/10.1021/acs.jctc.9b01274.

3D PES of Berry pseudorotation for PF_5 molecule, 3D PES of lever mechanism for SF_4 molecule, and reference system and associated normal modes for AB_6 in C_{5v} symmetry and AB_7 in C_{6v} symmetry (PDF)

■ AUTHOR INFORMATION

Corresponding Author

Elfi Kraka − *Department of Chemistry, Southern Methodist University, Dallas, Texas 75275-0314, United States;* orcid.org/0000-0002-9658-5626; Email: ekraka@gmail.com

Authors

Wenli Zou − *Institute of Modern Physics, Northwest University, and Shaanxi Key Laboratory for Theoretical Physics Frontiers, Xi'an, Shaanxi 710127, P. R. China; Department of Chemistry, Southern Methodist University, Dallas, Texas 75275-0314, United States;* orcid.org/0000-0002-0747-2428

Yunwen Tao − *Department of Chemistry, Southern Methodist University, Dallas, Texas 75275-0314, United States*

Complete contact information is available at:

https://dx.doi.org/10.1021/acs.jctc.9b01274
J. Chem. Theory Comput. 2020, 16, 3162−3193

https://pubs.acs.org/10.1021/acs.jctc.9b01274

Author Contributions

[¶]Contributed equally to this work.

Notes

The authors declare no competing financial interest.

■ ACKNOWLEDGMENTS

This work was financially supported by the National Science Foundation (Grant CHE 1464906). We thank SMU for providing generous computational resources. W.Z. also acknowledges the financial support by National Natural Science Foundation of China (Grant No. 21673175) and the Double First-Class University Construction Project of Northwest University.

■ DEDICATION

Dedicated to Dieter Cremer (1944−2017).

■ REFERENCES

(1) Portius, P.; Bühl, M.; George, M. W.; Grevels, F.-W.; Turner, J. J. Structure and Dynamics of Iron Pentacarbonyl. *Organometallics* **2019**, *38*, 4288−4297.
(2) Schilter, D. Trading places. *Nat. Rev. Chem.* **2020**, *4*, 2.
(3) Cahoon, J. F.; Sawyer, K. R.; Schlegel, J. P.; Harris, C. B. Determining Transition-State Geometries in Liquids Using 2D-IR. *Science* **2008**, *319*, 1820−1823.
(4) Lai, J.-C.; Jia, X.-Y.; Wang, D.-P.; Deng, Y.-B.; Zheng, P.; Li, C.-H.; Zuo, J.-L.; Bao, Z. Thermodynamically Stable Whilst Kinetically Labile Coordination Bonds Lead to Strong and Tough Self-Healing Polymers. *Nat. Commun.* **2019**, *10*, 1164.
(5) Moss, G. P. Basic Terminology of Stereochemistry (IUPAC Recommendations 1996). *Pure Appl. Chem.* **1996**, *68*, 2193−2222.
(6) Muetterties, E. L. Topological Representation of Stereoisomerism. I. Polytopal Rearrangements. *J. Am. Chem. Soc.* **1969**, *91*, 1636−1643.
(7) Muetterties, E. L.; Storr, A. T. Topological Analysis of Polytopal Rearrangements. Sufficient Conditions for Closure. *J. Am. Chem. Soc.* **1969**, *91*, 3098−3099.
(8) Asatryan, R.; Ruckenstein, E.; Hachmann, J. Revisiting the Polytopal Rearrangements in Penta-Coordinate d^7-Metallocomplexes: Modified Berry Pseudorotation, Octahedral Switch, and Butterfly Isomerization. *Chem. Sci.* **2017**, *8*, 5512−5525.
(9) Berry, R. S. Correlation of Rates of Intramolecular Tunneling Processes, with Application to Some Group V Compounds. *J. Chem. Phys.* **1960**, *32*, 933−938.
(10) Berry, R. S. Time-Dependent Measurements and Molecular Structure: Ozone. *Rev. Mod. Phys.* **1960**, *32*, 447−454.
(11) Muller, P. Glossary of Terms used in Physical Organic Chemistry (IUPAC Recommendations 1994). *Pure Appl. Chem.* **1994**, *66*, 1077−1184.
(12) McKee, M. L. Fluctional Molecules. *WIREs: Comput. Mol. Sci.* **2011**, *1*, 943−951.
(13) Nikitin, K.; O'Gara, R. Mechanisms and Beyond: Elucidation of Fluxional Dynamics by Exchange NMR Spectroscopy. *Chem. - Eur. J.* **2019**, *25*, 4551−4589.
(14) Christe, K. O.; Curtis, E. C.; Dixon, D. A. On the Problem of Heptacoordination: Vibrational Spectra, Structure, and Fluxionality of Iodine Heptafluoride. *J. Am. Chem. Soc.* **1993**, *115*, 1520−1526.
(15) Cass, M. E.; Hii, K. K.; Rzepa, H. S. Mechanisms That Interchange Axial and Equatorial Atoms in Fluxional Processes: Illustration of the Berry Pseudorotation, the Turnstile, and the Lever Mechanisms via Animation of Transition State Normal Vibrational Modes. *J. Chem. Educ.* **2006**, *83*, 336.
(16) Lonnon, D. G.; Ball, G. E.; Taylor, I.; Craig, D. C.; Colbran, S. B. Fluxionality in a Paramagnetic Seven-Coordinate Iron(II) Complex: A Variable-Temperature, Two-Dimensional NMR and DFT Study. *Inorg. Chem.* **2009**, *48*, 4863−4872.
(17) Mauksch, M.; von Ragué Schleyer, P. Effective Monkey Saddle Points and Berry and Lever Mechanisms in the Topomerization of SF_4 and Related Tetracoordinated AX_4 Species. *Inorg. Chem.* **2001**, *40*, 1756−1769.
(18) Couzijn, E. P. A.; Slootweg, J. C.; Ehlers, A. W.; Lammertsma, K. Stereomutation of Pentavalent Compounds: Validating the Berry Pseudorotation, Redressing Ugi's Turnstile Rotation, and Revealing the Two- and Three-Arm Turnstiles. *J. Am. Chem. Soc.* **2010**, *132*, 18127−18140.
(19) Russegger, P.; Brickmann, J. Pseudorotation of Trigonal Bipyramidal Molecules: Berry Rotation Contra "Turnstile" Rotation in PF_5. *Chem. Phys. Lett.* **1975**, *30*, 276−278.
(20) Adams, W. J.; Thompson, H. B.; Bartell, L. S. Structure, Pseudorotation, and Vibrational Mode Coupling in IF_7: An Electron Diffraction Study. *J. Chem. Phys.* **1970**, *53*, 4040−4046.
(21) Montgomery, C. D. Mechanisms of Pentacoordinate Pseudorotation. A Molecular Modeling Study of PF_5. *J. Chem. Educ.* **2001**, *78*, 844.
(22) Ramirez, F.; Ugi, I. Turnstile Rearrangement and Pseudorotation in the Permutational Isomerization of Pentavalent Phosphorus Compounds. In *Adv. Phys. Org. Chem.*; Gold, V., Ed.; Elsevier, 1971; Vol. 9, pp 25−126.
(23) Casanova, D.; Cirera, J.; Llunell, M.; Alemany, P.; Avnir, D.; Alvarez, S. Minimal Distortion Pathways in Polyhedral Rearrangements. *J. Am. Chem. Soc.* **2004**, *126*, 1755−1763.
(24) Alvarez, S.; Alemany, P.; Casanova, D.; Cirera, J.; Llunell, M.; Avnir, D. Shape Maps and Polyhedral Interconversion Paths in Transition Metal Chemistry. *Coord. Chem. Rev.* **2005**, *249*, 1693−1708.
(25) Rzepa, H. S.; Cass, M. E. A Computational Study of the Nondissociative Mechanisms that Interchange Apical and Equatorial Atoms in Square Pyramidal Molecules. *Inorg. Chem.* **2006**, *45*, 3958−3963.
(26) Csaszar, A. G.; Fabri, C.; Sarka, J. Quasistructural molecules. *Wiley Interdiscip. Rev.: Comput. Mol. Sci.* **2020**, *10*, No. e1432.
(27) Cotton, F. A. Fluxional Organometallic Molecules. *Acc. Chem. Res.* **1968**, *1*, 257−265.
(28) Muetterties, E. L. Stereochemically Nonrigid Structures. *Acc. Chem. Res.* **1970**, *3*, 266−273.
(29) Wentworth, R. Trigonal Prismatic vs. Octahedral Stereochemistry in Complexes Derived from Innocent Ligands. *Coord. Chem. Rev.* **1972**, *9*, 171−187.
(30) der Heyde, T. A. Determination of Reaction Paths for Pentacoordinate Metal Complexes with the Structure Correlation Method. *Angew. Chem., Int. Ed. Engl.* **1994**, *33*, 823−839.
(31) Gielen, M., Willem, R., Wrackmeyer, B., Eds. *Fluxional Organometallic and Coordination Compounds*; Wiley Online Library, 2004.
(32) Westmoreland, T. D. Symmetry Control of Chemical Reactions: Applications to the Berry Pseudorotation of Five-Coordinate Transition Metal Complexes. *Inorg. Chim. Acta* **2008**, *361*, 1187−1191.
(33) Faller, J. W. Stereochemical Nonrigidity of Organometallic Complexes. In *Encyclopedia of Inorganic and Bioinorganic Chemistry*; Scott, R. A., Ed.; Wiley Online Library, 2011; pp 1−34.
(34) Villafañe, F. Dynamic Behavior in Solution of Seven-Coordinated Transition Metal Complexes. *Coord. Chem. Rev.* **2014**, *281*, 86−99.
(35) Sandström, J. *Dynamic NMR Spectroscopy*; Academic Press, 1982.
(36) Ōki, M. *Applications of Dynamic NMR Spectroscopy to Organic Chemistry*; VCH Publishers, 1985.
(37) Perrin, C. L.; Dwyer, T. J. Application of Two-Dimensional NMR to Kinetics of Chemical Exchange. *Chem. Rev.* **1990**, *90*, 935−967.
(38) Bain, A. D. Chemical Exchange in NMR. *Prog. Nucl. Magn. Reson. Spectrosc.* **2003**, *43*, 63−103.
(39) Bryant, R. G. The NMR Time Scale. *J. Chem. Educ.* **1983**, *60*, 933−935.
(40) Eyring, H. The Activated Complex in Chemical Reactions. *J. Chem. Phys.* **1935**, *3*, 107−115.
(41) Houk, K. N.; Liu, F. Holy Grails for Computational Organic Chemistry and Biochemistry. *Acc. Chem. Res.* **2017**, *50*, 539−543.

(42) Harvey, J. N.; Himo, F.; Maseras, F.; Perrin, L. Scope and Challenge of Computational Methods for Studying Mechanism and Reactivity in Homogeneous Catalysis. *ACS Catal.* **2019**, *9*, 6803−6813.
(43) Ashley, D. C.; Jakubikova, E. Ray-Dutt and Bailar Twists in Fe(II)-Tris(2,2′-bipyridine): Spin States, Sterics, and Fe-N Bond Strengths. *Inorg. Chem.* **2018**, *57*, 5585−5596.
(44) Zabrodsky, H.; Peleg, S.; Avnir, D. Continuous Symmetry Measures. *J. Am. Chem. Soc.* **1992**, *114*, 7843−7851.
(45) Alvarez, S. Distortion Pathways of Transition Metal Coordination Polyhedra Induced by Chelating Topology. *Chem. Rev.* **2015**, *115*, 13447−13483.
(46) Alemany, P.; Casanova, D.; Alvarez, S.; Dryzun, C.; Avnir, D. Continuous Symmetry Measures: A New Tool in Quantum Chemistry. In *Reviews in Computational Chemistry*; Parrill, A. L., Lipkowitz, K. B., Eds.; John Wiley & Sons, Inc., 2017; Vol. *30*, Chapter 7, pp 289−352.
(47) Cremer, D.; Pople, J. A. General Definition of Ring Puckering Coordinates. *J. Am. Chem. Soc.* **1975**, *97*, 1354−1358.
(48) Cremer, D. RING - A Coordinate Transformation Program for Evaluating the Degree and Type of Puckering of a Ring Compound. *Quantum Chemical Program Exchange* **1975**, *288*, 1−8.
(49) Cremer, D. On the Correct Usage of the Cremer−Pople Puckering Parameters as Quantitative Descriptors of Ring Shapes - A Reply to Recent Criticism By Petit, Dillen And Geise. *Acta Crystallogr., Sect. B: Struct. Sci.* **1984**, *40*, 498−500.
(50) Cremer, D. Calculation of Puckered Rings with Analytical Gradients. *J. Phys. Chem.* **1990**, *94*, 5502−5509.
(51) Kraka, E.; Cremer, D. Dieter Cremer's Contribution to the Field of Theoretical Chemistry. *Int. J. Quantum Chem.* **2019**, *119*, No. e25849.
(52) Kraka, E. Preface: Dieter Cremer's Scientific Journey. *Mol. Phys.* **2019**, *117*, 1047−1058.
(53) Lyu, S.; Beiranvand, N.; Freindorf, M.; Kraka, E. Interplay of Ring Puckering and Hydrogen Bonding in Deoxyribonucleosides. *J. Phys. Chem. A* **2019**, *123*, 7087−7103.
(54) Zou, W.; Izotov, D.; Cremer, D. New Way of Describing Static and Dynamic Deformations of the Jahn-Teller Type in Ring Molecules. *J. Phys. Chem. A* **2011**, *115*, 8731−8742.
(55) Zou, W.; Filatov, M.; Cremer, D. Bond Pseudorotation, Jahn-Teller, and Pseudo-Jahn-Teller Effects in the Cyclopentadienyl Cation and its Pentahalogeno Derivatives. *Int. J. Quantum Chem.* **2012**, *112*, 3277−3288.
(56) Zou, W.; Cremer, D. Description of Bond Pseudorotation, Bond Pseudolibration, and Ring Pseudoinversion Processes Caused by the Pseudo-Jahn-Teller Effect: Fluoro Derivatives of the Cyclopropane Radical Cation. *Aust. J. Chem.* **2014**, *67*, 435−443.
(57) Cremer, D. Theoretical Determination of Molecular Structure and Conformation. III. The Pseudorotation Surface of 1,2,3-Trioxolane and 1,2,4-Trioxolane. *J. Chem. Phys.* **1979**, *70*, 1898−1910.
(58) Cremer, D.; Szabo, K. J. Ab Initio Studies of Six-Membered Rings: Present Status and Future Developments. In *Conformational Behavior of Six-Membered Rings*; Juaristi, E., Ed.; Wiley-VCH: Weinheim, 1995; pp 59−135.
(59) Biarnés, X.; Ardèvol, A.; Planas, A.; Rovira, C.; Laio, A.; Parrinello, M. The Conformational Free Energy Landscape of β-D-Glucopyranose. Implications for Substrate Preactivation in β-Glucoside Hydrolases. *J. Am. Chem. Soc.* **2007**, *129*, 10686−10693.
(60) Sega, M.; Autieri, E.; Pederiva, F. On the Calculation of Puckering Free Energy Surfaces. *J. Chem. Phys.* **2009**, *130*, 225102.
(61) Autieri, E.; Sega, M.; Pederiva, F.; Guella, G. Puckering Free Energy of Pyranoses: A NMR and Metadynamics-Umbrella Sampling Investigation. *J. Chem. Phys.* **2010**, *133*, 095104.
(62) Sega, M.; Autieri, E.; Pederiva, F. Pickett Angles and Cremer−Pople Coordinates as Collective Variables for the Enhanced Sampling of Six-Membered Ring Conformations. *Mol. Phys.* **2011**, *109*, 141−148.
(63) Huang, M.; Giese, T. J.; Lee, T.-S.; York, D. M. Improvement of DNA and RNA Sugar Pucker Profiles from Semiempirical Quantum Methods. *J. Chem. Theory Comput.* **2014**, *10*, 1538−1545.
(64) Iglesias-Fernández, J.; Raich, L.; Ardèvol, A.; Rovira, C. The Complete Conformational Free Energy Landscape of β-Xylose Reveals a Two-Fold Catalytic Itinerary for β-Xylanases. *Chem. Sci.* **2015**, *6*, 1167−1177.
(65) Lindner, J. O.; Sultangaleeva, K.; Röhr, M. I. S.; Mitrić, R. metaFALCON: A Program Package for Automatic Sampling of Conical Intersection Seams Using Multistate Metadynamics. *J. Chem. Theory Comput.* **2019**, *15*, 3450−3460.
(66) Paoloni, L.; Rampino, S.; Barone, V. Potential-Energy Surfaces for Ring-Puckering Motions of Flexible Cyclic Molecules through Cremer−Pople Coordinates: Computation, Analysis, and Fitting. *J. Chem. Theory Comput.* **2019**, *15*, 4280−4294.
(67) Alibay, I.; Bryce, R. A. Ring Puckering Landscapes of Glycosaminoglycan-Related Monosaccharides from Molecular Dynamics Simulations. *J. Chem. Inf. Model.* **2019**, *59*, 4729−4741.
(68) Cremer, D.; Kraka, E. From Molecular Vibrations to Bonding, Chemical Reactions, and Reaction Mechanism. *Curr. Org. Chem.* **2010**, *14*, 1524−1560.
(69) Kraka, E. Reaction Path Hamiltonian and its Use for Investigating Reaction Mechanism. In *Encyclopedia of Computational Chemistry*; Schleyer, P., Allinger, N., Clark, T., Gasteiger, J., Kollman, P., Schaefer, H., III, Schreiner, P., Eds.; John Wiley & Sons: New York, 1998; pp 2437−2463.
(70) Kraka, E. Reaction Path Hamiltonian and the Unified Reaction Valley Approach. *WIREs: Comput. Mol. Sci.* **2011**, *1*, 531−556.
(71) Cremer, D.; Larsson, J. A.; Kraka, E. New Developments in the Analysis of Vibrational Spectra on the Use of Adiabatic Internal Vibrational Modes. In *Theoretical and Computational Chemistry*; Parkanyi, C., Ed.; Elsevier: Amsterdam, 1998; Vol. *5*, pp 259−327.
(72) Konkoli, Z.; Cremer, D. A New Way of Analyzing Vibrational Spectra. I. Derivation of Adiabatic Internal Modes. *Int. J. Quantum Chem.* **1998**, *67*, 1−9.
(73) Konkoli, Z.; Cremer, D. A New Way of Analyzing Vibrational Spectra. III. Characterization of Normal Vibrational Modes in terms of Internal Vibrational Modes. *Int. J. Quantum Chem.* **1998**, *67*, 29−40.
(74) Levine, R.; Bernstein, R. *Molecular Reaction Dynamics and Chemical Reactivity*; Oxford University Press: New York, 1987.
(75) Brouard, M. *Reaction Dynamics; Oxford Chemistry Primers*; Oxford University Press: New York, 1998.
(76) Crim, F. F. Vibrational State Control of Bimolecular Reactions: Discovering and Directing the Chemistry. *Acc. Chem. Res.* **1999**, *32*, 877−884.
(77) Crim, F. F. Chemical Dynamics of Vibrationally Excited Molecules: Controlling Reactions in Gases and on Surfaces. *Proc. Natl. Acad. Sci. U. S. A.* **2008**, *105*, 12654−12661.
(78) Zare, R. N. Laser Control of Chemical Reactions. *Science* **1998**, *279*, 1875−1879.
(79) Sinha, A.; Hsiao, M. C.; Crim, F. F. Controlling Bimolecular Reactions: Mode and Bond Selected Reaction of Water with Hydrogen Atoms. *J. Chem. Phys.* **1991**, *94*, 4928−4935.
(80) Sinha, A.; Thoemke, J. D.; Crim, F. F. Controlling Bimolecular Reactions: Mode and Bond Selected Reaction of Water with Translationally Excited Chlorine Atoms. *J. Chem. Phys.* **1992**, *96*, 372−376.
(81) Simpson, W. R.; Rakitzis, T. P.; Kandel, S. A.; Orr-Ewing, A. J.; Zare, R. N. Reaction of Cl with Vibrationally Excited CH_4 and CHD_3: State-to-state Differential Cross Sections and Steric Effects for the HCl Product. *J. Chem. Phys.* **1995**, *103*, 7313−7335.
(82) Yoon, S.; Henton, S.; Zivkovic, A. N.; Crim, F. F. The Relative Reactivity of the Stretch-Bend Combination Vibrations of CH_4 in the $Cl(^2P_{3/2})+CH_4$ Reaction. *J. Chem. Phys.* **2002**, *116*, 10744−10752.
(83) Bechtel, H. A.; Camden, J. P.; Brown, D. J. A.; Zare, R. N. Comparing the Dynamical Effects of Symmetric and Antisymmetric Stretch Excitation of Methane in the $Cl+CH_4$ Reaction. *J. Chem. Phys.* **2004**, *120*, 5096−5103.
(84) Camden, J. P.; Bechtel, H. A.; Brown, D. J. A.; Zare, R. N. Effects of C-H Stretch Excitation on the $H+CH_4$ Reaction. *J. Chem. Phys.* **2005**, *123*, 134301.
(85) Crim, F. F. Vibrationally Mediated Photodissociation: Exploring Excited-State Surfaces and Controlling Decomposition Pathways. *Annu. Rev. Phys. Chem.* **1993**, *44*, 397−428.

https://dx.doi.org/10.1021/acs.jctc.9b01274
J. Chem. Theory Comput. 2020, 16, 3162−3193

(86) Reid, S. A.; Reisler, H. Experimental Studies of Resonances in Unimolecular Decomposition. *Annu. Rev. Phys. Chem.* **1996**, *47*, 495−525.
(87) Chen, J.; Zhou, X.; Zhang, Y.; Jiang, B. Vibrational Control of Selective Bond Cleavage in Dissociative Chemisorption of Methanol on Cu(111). *Nat. Commun.* **2018**, *9*, 4039.
(88) Shirhatti, P. R.; Rahinov, I.; Golibrzuch, K.; Werdecker, J.; Geweke, J.; Altschäffel, J.; Kumar, S.; Auerbach, D. J.; Bartels, C.; Wodtke, A. M. Observation of the Adsorption and Desorption of Vibrationally Excited Molecules on a Metal Surface. *Nat. Chem.* **2018**, *10*, 592−598.
(89) Stensitzki, T.; Yang, Y.; Kozich, V.; Ahmed, A. A.; Kössl, F.; Kühn, O.; Heyne, K. Acceleration of a Ground-State Reaction by Selective Femtosecond-Infrared-Laser-Pulse Excitation. *Nat. Chem.* **2018**, *10*, 126−131.
(90) Stei, M.; Carrascosa, E.; Dörfler, A.; Meyer, J.; Olasz, B.; Czakó, G.; Li, A.; Guo, H.; Wester, R. Stretching Vibration is a Spectator in Nucleophilic Substitution. *Sci. Adv.* **2018**, *4*, No. eaas9544.
(91) Heyne, K.; Kühn, O. Infrared Laser Excitation Controlled Reaction Acceleration in the Electronic Ground State. *J. Am. Chem. Soc.* **2019**, *141*, 11730−11738.
(92) Gillespie, R. Fifty Years of the VSEPR Model. *Coord. Chem. Rev.* **2008**, *252*, 1315−1327.
(93) Eckart, C. Some Studies Concerning Rotating Axes and Polyatomic Molecules. *Phys. Rev.* **1935**, *47*, 552−558.
(94) Sayvetz, A. The Kinetic Energy of Polyatomic Molecules. *J. Chem. Phys.* **1939**, *7*, 383−389.
(95) Zou, W.; Kalescky, R.; Kraka, E.; Cremer, D. Relating Normal Vibrational Modes to Local Vibrational Modes with the Help of an Adiabatic Connection Scheme. *J. Chem. Phys.* **2012**, *137*, 084114.
(96) Tao, Y.; Tian, C.; Verma, N.; Zou, W.; Wang, C.; Cremer, D.; Kraka, E. Recovering Intrinsic Fragmental Vibrations Using the Generalized Subsystem Vibrational Analysis. *J. Chem. Theory Comput.* **2018**, *14*, 2558−2569.
(97) Kudin, K. N.; Dymarsky, A. Y. Eckart Axis Conditions and the Minimization of the Root-Mean-Square Deviation: Two Closely Related Problems. *J. Chem. Phys.* **2005**, *122*, 224105.
(98) Kearsley, S. K. On the Orthogonal Transformation Used for Structural Comparisons. *Acta Crystallogr., Sect. A: Found. Crystallogr.* **1989**, *A45*, 208−210.
(99) Peng, C.; Ayala, P. Y.; Schlegel, H. B.; Frisch, M. J. Using Redundant Internal Coordinates to Optimize Equilibrium Geometries and Transition States. *J. Comput. Chem.* **1996**, *17*, 49−56.
(100) Li, X.; Frisch, M. J. Energy-Represented Direct Inversion in the Iterative Subspace within a Hybrid Geometry Optimization Method. *J. Chem. Theory Comput.* **2006**, *2*, 835−839.
(101) Kraka, E.; Zou, W.; Filatov, M.; Tao, Y.; Grafenstein, J.; Izotov, D.; Gauss, J.; He, Y.; Wu, A.; Konkoli, Z.; Polo, V.; Olsson, L.; He, Z.; Cremer, D. *COLOGNE2019*; SMU, 2019; see http://www.smu.edu/catco.
(102) Frisch, M. J.; Trucks, G. W.; Schlegel, H. B.; Scuseria, G. E.; Robb, M. A.; Cheeseman, J. R.; Scalmani, G.; Barone, V.; Petersson, G. A.; Nakatsuji, H.; Li, X.; Caricato, M.; Marenich, A. V.; Bloino, J.; Janesko, B. G.; Gomperts, R.; Mennucci, B.; Hratchian, H. P.; Ortiz, J. V.; Izmaylov, A. F.; Sonnenberg, J. L.; Williams-Young, D.; Ding, F.; Lipparini, F.; Egidi, F.; Goings, J.; Peng, B.; Petrone, A.; Henderson, T.; Ranasinghe, D.; Zakrzewski, V. G.; Gao, J.; Rega, N.; Zheng, G.; Liang, W.; Hada, M.; Ehara, M.; Toyota, K.; Fukuda, R.; Hasegawa, J.; Ishida, M.; Nakajima, T.; Honda, Y.; Kitao, O.; Nakai, H.; Vreven, T.; Throssell, K.; Montgomery, J. A., Jr.; Peralta, J. E.; Ogliaro, F.; Bearpark, M. J.; Heyd, J. J.; Brothers, E. N.; Kudin, K. N.; Staroverov, V. N.; Keith, T. A.; Kobayashi, R.; Normand, J.; Raghavachari, K.; Rendell, A. P.; Burant, J. C.; Iyengar, S. S.; Tomasi, J.; Cossi, M.; Millam, J. M.; Klene, M.; Adamo, C.; Cammi, R.; Ochterski, J. W.; Martin, R. L.; Morokuma, K.; Farkas, O.; Foresman, J. B.; Fox, D. J. *Gaussian 16* Revision B.01; Gaussian Inc.: Wallingford, CT, 2016.
(103) Becke, A. D. Density-Functional Thermochemistry. III. The Role of Exact Exchange. *J. Chem. Phys.* **1993**, *98*, 5648−5652.
(104) Lee, C.; Yang, W.; Parr, R. G. Development of the Colle-Salvetti Correlation-Energy Formula into A Functional of the Electron Density. *Phys. Rev. B: Condens. Matter Mater. Phys.* **1988**, *37*, 785−789.
(105) Vosko, S. H.; Wilk, L.; Nusair, M. Accurate Spin-Dependent Electron Liquid Correlation Energies for Local Spin Density Calculations: A Critical Analysis. *Can. J. Phys.* **1980**, *58*, 1200−1211.
(106) Stephens, P. J.; Devlin, F. J.; Chabalowski, C. F.; Frisch, M. J. Ab Initio Calculation of Vibrational Absorption and Circular Dichroism Spectra Using Density Functional Force Fields. *J. Phys. Chem.* **1994**, *98*, 11623−11627.
(107) Dunning, T. H. Gaussian Basis Sets for Use in Correlated Molecular Calculations. I. The Atoms Boron Through Neon and Hydrogen. *J. Chem. Phys.* **1989**, *90*, 1007−1023.
(108) Zhao, Y.; Truhlar, D. G. A New Local Density Functional for Main-Group Thermochemistry, Transition Metal Bonding, Thermochemical Kinetics, and Noncovalent Interactions. *J. Chem. Phys.* **2006**, *125*, 194101.
(109) Weigend, F.; Ahlrichs, R. Balanced Basis Sets of Split Valence, Triple Zeta Valence and Quadruple Zeta Valence Quality for H to Rn: Design and Assessment of Accuracy. *Phys. Chem. Chem. Phys.* **2005**, *7*, 3297−3305.
(110) Weigend, F. Accurate Coulomb-Fitting Basis Sets for H to Rn. *Phys. Chem. Chem. Phys.* **2006**, *8*, 1057−1065.
(111) Zhao, Y.; Truhlar, D. G. The M06 Suite of Density Functionals for Main Group Thermochemistry, Thermochemical Kinetics, Noncovalent Interactions, Excited States, and Transition Elements: Two New Functionals and Systematic Testing of Four M06-Class Functionals and 12 Other Functionals. *Theor. Chem. Acc.* **2008**, *120*, 215−241.
(112) Hratchian, H. P.; Schlegel, H. B. Accurate Reaction Paths using a Hessian Based Predictor-Corrector Integrator. *J. Chem. Phys.* **2004**, *120*, 9918−9924.
(113) Hratchian, H. P.; Schlegel, H. B. Using Hessian Updating To Increase the Efficiency of a Hessian Based Predictor-Corrector Reaction Path Following Method. *J. Chem. Theory Comput.* **2005**, *1*, 61−69.
(114) Hratchian, H. P.; Kraka, E. Improved Predictor-Corrector Integrators For Evaluating Reaction Path Curvature. *J. Chem. Theory Comput.* **2013**, *9*, 1481−1488.
(115) Gonzalez, C.; Schlegel, H. B. An Improved Algorithm for Reaction Path Following. *J. Chem. Phys.* **1989**, *90*, 2154−2161.
(116) Gonzalez, C.; Schlegel, H. B. Reaction Path Following in Mass-Weighted Internal Coordinates. *J. Phys. Chem.* **1990**, *94*, 5523−5527.
(117) Page, M.; McIver, J. W. On Evaluating the Reaction Path Hamiltonian. *J. Chem. Phys.* **1988**, *88*, 922−935.
(118) Page, M.; Doubleday, C.; McIver, J. W. Following Steepest Descent Reaction Paths. The Use of Higher Energy Derivatives With *ab initio* Electronic Structure Methods. *J. Chem. Phys.* **1990**, *93*, 5634−5642.
(119) Ruff, O.; Heinzelmann, A. Über das Uranhexafluorid. *Z. Anorg. Allg. Chem.* **1911**, *72*, 63−84.
(120) Pople, J.; Schneider, W.; Bernstein, H. J. *High-Resolution Nuclear Magnetic Resonance*; McGraw-Hill, 1959; p 223.
(121) Muetterties, E. L.; Phillips, W. D. Structure of ClF_3 and Exchange Studies on Some Halogen Fluorides by Nuclear Magnetic Resonance. *J. Am. Chem. Soc.* **1957**, *79*, 322−326.
(122) Muetterties, E. L.; Phillips, W. D. Structure and Exchange Processes in Some Inorganic Fluorides by Nuclear Magnetic Resonance. *J. Am. Chem. Soc.* **1959**, *81*, 1084−1088.
(123) Klemperer, W. G.; Krieger, J. K.; McCreary, M. D.; Muetterties, E. L.; Traficante, D. D.; Whitesides, G. M. Dynamic Nuclear Magnetic Resonance Study of Fluorine Exchange in Liquid Sulfur Tetrafluoride. *J. Am. Chem. Soc.* **1975**, *97*, 7023−7030.
(124) Rothman, M. J.; Lohr, L. L. Analysis of an Energy Minimization Method for Locating Transition States on Potential Energy Hypersurfaces. *Chem. Phys. Lett.* **1980**, *70*, 405−409.
(125) Williams, I. H.; Maggiora, G. M. Use and Abuse of the Distinguished-Coordinate Method for Transition-State Structure Searching. *J. Mol. Struct.: THEOCHEM* **1982**, *89*, 365−378.

https://dx.doi.org/10.1021/acs.jctc.9b01274
J. Chem. Theory Comput. 2020, 16, 3162−3193

(126) Fadrná, E.; Koča, J. Single-Coordinate-Driving Method Coupled with Simulated Annealing. An Efficient Tool To Search Conformational Space. *J. Phys. Chem. B* **1997**, *101*, 7863−7868.
(127) Yang, M.; Zou, J.; Wang, G.; Li, S. Automatic Reaction Pathway Search via Combined Molecular Dynamics and Coordinate Driving Method. *J. Phys. Chem. A* **2017**, *121*, 1351−1361.
(128) Yang, M.; Yang, L.; Wang, G.; Zhou, Y.; Xie, D.; Li, S. Combined Molecular Dynamics and Coordinate Driving Method for Automatic Reaction Pathway Search of Reactions in Solution. *J. Chem. Theory Comput.* **2018**, *14*, 5787−5796.
(129) Plessow, P. N. Efficient Transition State Optimization of Periodic Structures through Automated Relaxed Potential Energy Surface Scans. *J. Chem. Theory Comput.* **2018**, *14*, 981−990.
(130) Taha, A. N.; True, N. S.; LeMaster, C. B.; LeMaster, C. L.; Neugebauer-Crawford, S. M. Gas-Phase Nuclear Magnetic Resonance Study of Berry Pseudorotation of SF_4. Comparison of Experimental and Calculated Kinetic Parameters and Falloff Kinetics. *J. Phys. Chem. A* **2000**, *104*, 3341−3348.
(131) Gutowsky, H. S.; McCall, D. W.; Slichter, C. P. Nuclear Magnetic Resonance Multiplets in Liquids. *J. Chem. Phys.* **1953**, *21*, 279−292.
(132) Muetterties, E. L. Topological Representation of Stereoisomerism. II. The Five-Atom Family. *J. Am. Chem. Soc.* **1969**, *91*, 4115−4122.
(133) Ugi, I.; Marquarding, D.; Klusacek, H.; Gillespie, P.; Ramirez, F. Berry Pseudorotation and Turnstile Rotation. *Acc. Chem. Res.* **1971**, *4*, 288−296.
(134) Moberg, C. Stereomutation in Trigonal-Bipyramidal Systems: A Unified Picture. *Angew. Chem., Int. Ed.* **2011**, *50*, 10290−10292.
(135) Braga, D.; Grepioni, F.; Orpen, A. G. Nickel Carbonyl ($Ni(CO)_4$) and Iron Carbonyl ($Fe(CO)_5$): Molecular Structures in the Solid State. *Organometallics* **1993**, *12*, 1481−1483.
(136) Deerenberg, S.; Schakel, M.; de Keijzer, A. H. J. F.; Kranenburg, M.; Lutz, M.; Spek, A. L.; Lammertsma, K. Tetraalkylammonium Pentaorganosilicates: The First Highly Stable Silicates with Five Hydrocarbon Ligands. *Chem. Commun.* **2002**, 348−349.
(137) Campbell, B. S.; De'Ath, N. J.; Denney, D. B.; Denney, D. Z.; Kipnis, I. S.; Min, T. B. Some Caged Polycyclic Phosphoranes. *J. Am. Chem. Soc.* **1976**, *98*, 2924−2927.
(138) Alvarez, S. Distortion Pathways of Transition Metal Coordination Polyhedra Induced by Chelating Topology. *Chem. Rev.* **2015**, *115*, 13447−13483.
(139) Bailar, J. C., Jr Some Problems in the Stereochemistry of Coordination Compounds: Introductory Lecture. *J. Inorg. Nucl. Chem.* **1958**, *8*, 165−175.
(140) Ray, P.; Dutt, N. Kinetics and Mechanism of Racemization of Optically Active Cobaltic Trisbiguanide Complex. *J. Indian Chem. Soc.* **1943**, *20*, 81−92.
(141) Marian, C. M. Spin-Orbit Coupling and Intersystem Crossing in Molecules. *WIREs: Comput. Mol. Sci.* **2012**, *2*, 187−203.
(142) Tao, Y.; Pei, Z.; Bellonzi, N.; Mao, Y.; Zou, Z.; Liang, W.; Yang, Z.; Shao, Y. Constructing Spin-Adiabatic States for the Modeling of Spin-Crossing Reactions. I. A Shared-Orbital Implementation. *Int. J. Quantum Chem.* **2020**, *120*, No. e26123.
(143) Rzepa, H. S.; Cass, M. E. In Search of the Bailar and Rây-Dutt Twist Mechanisms That Racemize Chiral Trischelates: A Computational Study of Sc^{III}, Ti^{IV}, Co^{III}, Zn^{II}, Ga^{III}, and Ge^{IV} Complexes of a Ligand Analogue of Acetylacetonate. *Inorg. Chem.* **2007**, *46*, 8024−8031.
(144) Claassen, H. H.; Gasner, E. L.; Selig, H. Vibrational Spectra of IF_7 and ReF_7. *J. Chem. Phys.* **1968**, *49*, 1803−1807.
(145) Bartell, L. S.; Rothman, M. J.; Gavezzotti, A. Pseudopotential SCF-MO Studies of Hypervalent Compounds. IV. Structure, Vibrational Assignments, and Intramolecular Forces in IF_7. *J. Chem. Phys.* **1982**, *76*, 4136−4143.
(146) Kuczkowski, R.; Lawrence, S. Bartell: Biographical Notes. *J. Mol. Struct.* **1999**, 485−486 xi−xxvii.
(147) Minyaev, R. M.; Wales, D. J. Transition Vector Symmetry and the Internal Pseudo-Rotation and Inversion Paths of CIF_4^+. *J. Chem. Soc., Faraday Trans.* **1994**, *90*, 1831−1837.
(148) Lord, R. C.; Lynch, M. A.; Schumb, W. C.; Slowinski, E. J. The Vibrational Spectra and Structures of Iodine Pentafluoride and Heptafluoride. *J. Am. Chem. Soc.* **1950**, *72*, 522−527.
(149) Musher, J. I.; Cowley, A. H. Intramolecular Ligand Rearrangements in Four- and Five-Coordinate Sulfur Compounds. *Inorg. Chem.* **1975**, *14*, 2302−2304.
(150) Heidrich, D.; Quapp, W. Saddle Points of Index 2 on Potential Energy Surfaces and Their Role in Theoretical Reactivity Investigations. *Theor. Chem. Acc.* **1986**, *70*, 89−98.
(151) Li, Y.; Houk, K. N. The Dimerization of Cyclobutadiene. An ab Initio CASSCF Theoretical Study. *J. Am. Chem. Soc.* **1996**, *118*, 880−885.
(152) Mezey, P. G. *Potential Energy Hypersurfaces*; Elsevier: New York, 1987; p 76.
(153) Sadasivam, D. V. *Theoretical and Experimental Studies of Some Unusual Potential Energy Surfaces and Pseudopericyclic Reactions*. Ph.D. thesis, Texas Tech University, 2006.
(154) Tama, F.; Sanejouand, Y.-H. Conformational Change of Proteins Arising from Normal Mode Calculations. *Protein Eng., Des. Sel.* **2001**, *14*, 1−6.
(155) Ioannidis, E. I.; Gani, T. Z. H.; Kulik, H. J. molSimplify: A Toolkit for Automating Discovery in Inorganic Chemistry. *J. Comput. Chem.* **2016**, *37*, 2106−2117.
(156) Ioannidis, E. I. *Automated Structure Generation for First-Principles Transition-Metal Catalysis*. Ph.D. thesis, Massachusetts Institute of Technology, 2018.
(157) Foscato, M.; Venkatraman, V.; Jensen, V. R. DENOPTIM: Software for Computational de Novo Design of Organic and Inorganic Molecules. *J. Chem. Inf. Model.* **2019**, *59*, 4077−4082.
(158) Kulik, H. J. Making Machine Learning a Useful Tool in the Accelerated Discovery of Transition Metal Complexes. *Wiley Interdiscip. Rev.: Comput. Mol. Sci.* **2020**, *10*, No. e1439.
(159) Fiorin, G.; Klein, M. L.; Hénin, J. Using Collective Variables to Drive Molecular Dynamics Simulations. *Mol. Phys.* **2013**, *111*, 3345−3362.

https://dx.doi.org/10.1021/acs.jctc.9b01274
J. Chem. Theory Comput. 2020, 16, 3162−3193